

DETERMINATION OF HYDROGEN IN LOW
ALLOY STEEL BY MAGNETOACOUSTIC
EMISSION AND BARKHAUSEN NOISE

by

Jonathan A. Poncelow

A thesis submitted to the Faculty and the Board of Trustees of the Colorado School of Mines in partial fulfillment of the requirements for the degree of Doctor of Philosophy (Materials Science).

Golden, Colorado

Date _____

Signed: _____

Jonathan A. Poncelow

Signed: _____

Prof. Stephen L. Liu
Thesis Advisor

Signed: _____

Prof. David L. Olson
Thesis Advisor

Golden, Colorado

Date _____

Signed: _____

Prof. Ryan O'Hayre
Professor and Program Head
Department of Metallurgical and Materials Engineering

ABSTRACT

This work serves to assess the viability of a nondestructive technique for the determination of hydrogen in steel welds using variation in magnetic properties. To that end, the philosophical framework is established through a review of applicable theories and development of new models with regard to hydrogen mobility and ferromagnetism, where possible. Experimental methods and analytical algorithms are developed to determine variation in magnetoacoustic and Barkhausen emission character and changes in magnetization behavior. These techniques are then applied to a select number of low-alloy steel samples varied in microstructure by heat treatment and hydrogen concentration by electrolytic charging. Results of these tests are interpreted in the context of hydrogen trapping in ferrous metals and the impact of the solute on the ferromagnetic properties and magnetization dynamics of steel. Finally, the methods developed are evaluated for their robustness as nondestructive methods for hydrogen characterization in field and/or laboratory environments.

TABLE OF CONTENTS

ABSTRACT	iii
LIST OF FIGURES	vii
LIST OF TABLES	x
LIST OF SYMBOLS	xi
LIST OF ABBREVIATIONS	xv
ACKNOWLEDGMENTS	xvi
DEDICATION	xvii
CHAPTER 1 INTRODUCTION	1
1.1 Effects of Hydrogen on Steel	2
1.1.1 Hydrogen Measurement	3
CHAPTER 2 REVIEW OF RELEVANT THEORY	4
2.1 Hydrogen Transport	4
2.1.1 Hydrogen Trapping	5
2.1.2 Modelling Hydrogen Absorption and Desorption	7
2.2 Hydrogen and Ferromagnetism in Iron	14
2.2.1 Ferromagnetism	16
2.2.2 Magnetic Domains	18
2.2.3 Domain Wall Dynamics: Barkhausen Noise	22
2.2.4 Magnetostriction	26
2.2.5 Magnetoacoustic Emission	28

2.2.6	Magnetic Hysteresis and Nonlinearity	30
2.3	Summary	33
CHAPTER 3 EXPERIMENT		34
3.1	Samples	34
3.1.1	AISI 4340 Steel	35
3.1.2	AISI 4140 Steel	36
3.2	Cathodic Charging	38
3.3	Hydrogen Determination	40
3.4	Testing of Magnetic Properties	42
3.4.1	Apparatus Design	43
3.4.2	Analog Signal Processing	44
3.4.3	Digitization and Storage	48
3.4.4	Digital Filtering	48
3.5	Magnetic Flux Estimation	51
3.6	MAE/MBN Quantification	51
3.6.1	Window Convolution	52
3.6.2	MAE/MBN Cycles	53
3.6.3	Characterization of Experimental Arrangement	55
CHAPTER 4 RESULTS		62
4.1	Cathodic Charging	62
4.2	Eddy Currents: Resistance	63
4.3	Magnetic Flux: Phase	64
4.4	Magnetic Flux: Amplitude	67

4.5	Magnetic Flux: Harmonic Distortion	70
4.6	Barkhausen Noise	71
4.7	Magnetoacoustic Emission	79
CHAPTER 5 DISCUSSION		86
5.1	Discussion	86
5.2	Field Probe Design	87
5.3	Conclusions	90
REFERENCES CITED		93

LIST OF FIGURES

Figure 2.1	Hydrogen concentration profile for various times during charging ($t_{ch} = 120$ min) and discharging as obtained via numerical solution.	9
Figure 2.2	Hydrogen concentration profile for various times during charging ($t_{ch} = 120$ min) and discharging as obtained via numerical solution.	10
Figure 2.3	Predicted hydrogen concentration for $9 \times 9 \times 20$ mm during a charging and discharging cycle for various trapping parameters and charging times for a diffusivity of $D_{eff} = 0.5 \times 10^{-9} \text{ m}^2 \text{ s}^{-1}$	12
Figure 2.4	Predicted hydrogen concentration for during a charging and discharging cycle for various trapping parameters and charging times for a diffusivity of $D_{eff} = 2.0 \times 10^{-9} \text{ m}^2 \text{ s}^{-1}$	13
Figure 2.5	Electronic Density of States for BCC iron (above, with spin state) and a Fe_{32}H supercell (center) from local-spin-density functional theory.	19
Figure 2.6	Illustration of magnetic domain (Bloch) wall.	22
Figure 2.7	Schematic illustration of the various stages of magnetization of a ferromagnetic structure.	23
Figure 2.8	Impact of changes in parameters for the Jiles-Atherton model of ferromagnetic hysteresis.	32
Figure 3.1	Arrangement for cathodic charging of steel samples.	39
Figure 3.2	Apparatus for diffusible hydrogen concentration determination.	41
Figure 3.3	Eudiometer tube calibration curve for evolved hydrogen determination.	42
Figure 3.4	Photograph of magnetic testing fixture with sample.	44
Figure 3.5	Physical arrangement and signal flow during Magnetoacoustic and Barkhausen noise testing (profile).	45
Figure 3.6	Electronic schematic for MAE/MBN transducer front ends.	47
Figure 3.7	Filter response for digital filter used for Barkhausen and magnetoacoustic effect measurements.	49

Figure 3.8	Typical filtered waveforms for a single measurement.	50
Figure 3.9	An example of windowed RMS waveforms.	52
Figure 3.10	Magnetoacoustic and Barkhausen emission waveforms averaged over twenty cycles.	54
Figure 3.11	Typical periodograms for a single measurement, showing the evolution of spectral content of Barkhausen and magnetoacoustic emission over several cycles of magnetization.	55
Figure 3.12	Physical arrangement for characterizing the apparatus.	57
Figure 3.13	Two magnetization cycles demonstrating amplifier output voltage, magnetic flux density, driving coil current, and core flux characteristic behavior.	58
Figure 3.14	Total harmonic distortion and phase of power amplifier output voltage relative to waveform generator output voltage in the absence of a sample (9 mm air gap).	58
Figure 3.15	Total harmonic distortion and phase of magnetic core current relative to waveform output voltage in the absence of a sample.	59
Figure 3.16	Total harmonic distortion and phase relative to waveform generator output for magnetic flux density in the absence of a sample.	60
Figure 3.17	Total harmonic distortion and phase of magnetic flux detected via pickup coil relative to waveform generator output in the absence of a sample.	61
Figure 4.1	Amount of hydrogen cathodically absorbed in samples of AISI 4140 steel for various charging times.	63
Figure 4.2	Changes in resistance of a low-carbon steel wire (0.356 mm dia.) after charging at 10 mA cm^{-2} for one hour.	65
Figure 4.3	Change in core flux phase with time as hydrogen desorbs for AISI 4340 tests.	66
Figure 4.4	Change in core flux phase with hydrogen outgassing for AISI 4140 steel tests.	67
Figure 4.5	Change in core flux amplitude (RMS average) with hydrogen outgassing for AISI 4340 steel tests.	68

Figure 4.6	Change in core flux magnitude (RMS average) with hydrogen outgassing for AISI 4140 steel tests.	69
Figure 4.7	Change in core flux harmonic distortion with hydrogen outgassing for AISI 4340 steel tests.	72
Figure 4.8	Change in core flux harmonic distortion with hydrogen outgassing for AISI 4140 steel tests.	73
Figure 4.9	Decay of MBN energy with time for samples of AISI 4340 steel charged with hydrogen.	75
Figure 4.10	Evolution of MBN counts with time for samples of AISI 4340 steel charged to various levels.	76
Figure 4.11	Decay of MBN energy with time for samples of AISI 4140 steel charged to various levels.	77
Figure 4.12	Variation of MBN energy slope with tempering temperature.	79
Figure 4.13	Change in the number of MBN emission events per waveform with loss of hydrogen in AISI 4140 steel.	80
Figure 4.14	Magnetoacoustic emission energy evolution following hydrogen charging for various currents and times for AISI 4340.	82
Figure 4.15	Evolution of magnetoacoustic emission events ($> 2\hat{\sigma}$) following hydrogen charging for various currents and times for AISI 4340.	83
Figure 4.16	Magnetoacoustic emission “energy” evolution following hydrogen charging for various currents and times.	84
Figure 4.17	Magnetoacoustic emission events ($> 2\hat{\sigma}$) evolution following hydrogen charging for various currents and times.	85
Figure 5.1	Proposed field NDE probe digitization and processing block diagram. . .	88

LIST OF TABLES

Table 3.1	Specified nominal chemical compositions for steel samples used in the MAE/MBN tests.	35
Table 3.2	Sample matrix for AISI 4340 steel. All samples oil quenched from a temperature of 840 °C	36
Table 3.3	Experimental matrix for AISI 4340 steel.	36
Table 3.4	Sample matrix for AISI 4140 steel. All samples oil quenched from a temperature of 840 °C	37
Table 3.5	Experimental matrix for AISI 4140 steel. All samples oil quenched from a temperature of 840 °C	37
Table 3.6	Component values and parameter differences between tests for AISI 4140 and 4340 steels.	46
Table 4.1	Schematic hydrogen desorption trends for magnetoacoustic emission experiments, with Oriani model parameters corresponding to general behavior of Figures 2.1 and 2.2	81

LIST OF SYMBOLS

Indices	$\{i, j\}$
Complex Conjugate	\square^*
Time Derivative	$\dot{\square}$
Convolution	$\square \star \triangle$
Lattice Parameter, Activity	a
Jiles-Atherton Shape Parameters	a, c, k
Magnetic Flux Density	\mathbf{B}
Magnetoelastic Coupling Coefficients	$B_{\{1,2\}}$
Concentration	c
Longitudinal Acoustic Velocity	c_l
Number of Atoms per Volume	C
Elastic Constant	$C_{\{11,12,44\}}$
Capacitance	$C_{\{C,F,T\}}$
Diffusivity	D
Effective Diffusivity	D_{eff}
Strain	e
Energy	E
Anisotropy Energy	E_a
Fermi Energy Level	E_F
Magnetoelastic Energy	E_{mag-el}

Magnetostatic Energy	E_{ms}
Frequency	f
Magnetizing (Driving) Frequency	f_d
Low, High Cutoff Frequency	f_L, f_H
Sampling Frequency	f_{sa}
Fermi-Dirac Distribution	$f(E)$
Density of States	$g(E)$
Applied External Magnetic Field	\mathbf{H}
Coercive Field	H_c
Molecular Exchange Field	H_m
Exchange Integral	J
Trapping Probability	k
Equilibrium Constant	K
Anisotropy Coefficient	$K_{\{1,2,3\}}$
Characteristic Length	l
Magnetization	\mathbf{M}
Anhyseretic Magnetization	M_{an}
Irreversible (Reversible) Magnetization	$M_{irr}, (M_{rev})$
Saturation Magnetization	M_s
Filled Trap Fraction	n
Number per Volume, Nearest Neighbors	N
Demagnetizing Factor	N_d
Release Probability	p

Legendre Coefficient	$P_{\{g,l,q\}}$
Power Spectral Density	$P(\omega)$
Radial Coordinate	r
Rate	\mathcal{R}
Resistance	$R_{\{F,IN\}}$
Spin	\vec{s}
Cross-Sectional Area	S
Charging Time	t_{chg}
Temperature	T
Tempering Temperature	T_{temp}
Volume, Voltage	V
Spin-Pair Potential Function	w
Wiener-Lévy Perturbation	$W(\Phi)$
Trapping Site	X
Mean Field Parameter	α
Direction Cosine	$\alpha_{\{1,2,3\}}, \beta_{\{1,2,3\}}$
Occupancy Fraction, (Phase) Angle	θ
Magnetostriction Coefficient (Average)	$\lambda_{\{100,111\}}, (\bar{\lambda})$
Magnetic Permeability	μ
Permeability of Free Space	μ_0
Bohr Magnetron	μ_B
Correlation Length	ξ
Density	ρ

Electrical Conductivity	σ
Standard Deviation	$\hat{\sigma}$
Time Constant	τ
Angle	ϕ
Magnetic Flux	Φ
Wavefunction	ψ
Angular Frequency	ω

LIST OF ABBREVIATIONS

Arbitrary Waveform Generator	AWG
Body-centered Cubic	BCC
Density of States	DoS
Domain Wall	DW
Electromotive Force	EMF
Low Pass Filter	LPF
Magnetoacoustic Emission	MAE
Magnetic Barkhausen Noise	MBN
Nondestructive Evaluation	NDE
Samples	Sa
Total Harmonic Distortion and Noise	THDN

ACKNOWLEDGMENTS

My deepest gratitude to:

- F., S. & H.S.
- Joe Scott for his gracious financial support and guidance
- My advisors, Profs. David Olson and Stephen Liu, for their valuable input
- My family and (especially) wife, Bethany, whose patience and encouragement have scaled

$$P_{atience} + S_{upport} = \frac{1}{(t_{defense} - t)^2}$$

For Mother Dearest



Elaine Poncelow (1952–2012) and the author *c.* 1988.

CHAPTER 1

INTRODUCTION

Despite being instrumental in the development of some of the greatest advances in physics in the last century, hydrogen—particularly its role in the behavior of metals—remains a beguiling enigma: as one question is tackled, more are raised. Nevertheless, this thesis intends to explore some of the mystery around hydrogen’s impact on steel. Specifically, this work addresses the effects of hydrogen on ferromagnetic behavior of iron via the following questions:

1. How does hydrogen, dissolved in steel, affect the magnetic properties of low alloy steel as determined by magnetic Barkhausen noise (MBN), magnetoacoustic emission (MAE), and through-flux measurements?
2. How and to what extent does tempering obfuscate the role of hydrogen in steel?
3. Are the effects on MBN and MAE quantifiable in such a way as to warrant their use as proxies for the determination of diffusible hydrogen content and susceptibility to embrittlement?
4. What would be the appropriate elements of a nondestructive evaluation (NDE) method for the determination of diffusible hydrogen in steel weldments?

Guided by these questions, this study has focused on observing changes in MBN/MAE behavior as hydrogen is evolved from cathodically-charged steel samples. The work is reported in the following manner:

Hydrogen interactions, as relate to its transport and microscopic effects in steel, are reviewed in the context of prior theory and data in the next section, Chapter 2. Models established in the vast body of existing work are applied to the current system which has

been developed for tests in this study, the details of which are outlined in the chapter on experiments, Chapter 3. Details of algorithms applied to reduce the data (acquired primarily as oscilloscope waveforms) into more meaningful results are given in the remainder of that chapter. The outcomes of these steps and their analyses (informed by prior work on microstructure) are presented in the chapter of results, Chapter 4. Concluding discussion is provided in the final chapter with remarks as to the questions raised and suggestions for continued work in the future.

1.1 Effects of Hydrogen on Steel

Hydrogen, in its ubiquity, inevitably works itself into welds¹ where it becomes a limiting factor in many high-strength applications. Water is considered the primary source of hydrogen through its dissociation during the welding process, and control of moisture content in electrodes, base metal, and atmosphere is an important step in limiting hydrogen intrusion. The exact mechanisms by which hydrogen reduces ductility, toughness, and fatigue life remain enigmatic and debated, but three elements are considered necessary for cracking to occur: hydrogen, stress, and a susceptible microstructure.

Due in large part to an absence of well-established nondestructive methods to assess a material's susceptibility *in situ*, historical mitigation strategies have had to err on the side of caution, increasing costs and delays[1]. It is not the purpose of this work to contribute to the ongoing debate regarding mechanisms of hydrogen embrittlement, as thoroughly reviewed in various articles and books[2, 3] nor to address the extent to which hydrogen impacts a given material or microstructure with any specificity. Rather, the focus of this study is to establish a fundamental link between ferromagnetic properties and hydrogen content in steel and demonstrate the feasibility of a relevant NDE method.

¹Hydrogen ingress can also occur when it is present as part of the environment, e.g. in sour gas service or corrosion.

1.1.1 Hydrogen Measurement

One especially nefarious aspect of hydrogen damage is that—despite every reasonable effort to control hydrogen—it is frequently unknown to what extent the element has ingressed and how it is distributed. There is a significant body of literature devoted to the reliable non-destructive detection of hydrogen in ferrous alloys, and considerable variety in the methods proposed. Low frequency eddy current analysis has demonstrated sensitivity to hydrogen in welds[4, 5]. Measurements of ultrasonic properties have of course been explored extensively as possible NDE methods in steel, and met with varying degrees of success: Rayleigh Wave velocity, attenuation[6, 7].

Localized hydrogen concentrations can be detected nondestructively via flux at solid-air interfaces by gaseous collection and remote analysis by several means[8]. Optical methods including laser-ablation[9] and reflectometry[10] have also been developed which can reliably detect presence or effluence of hydrogen at surfaces. These methods, while reliable and accurate, are restricted to characterization of gaseous hydrogen as it effuses from the material and can require bulky equipment, limiting their utility in field-ready NDE applications.

Magnetoacoustic emission and Barkhausen noise have been studied extensively in their application to nondestructive evaluation of residual stresses, formation of carbides[11], and plastic deformation[12] (among many others) in iron and various steel alloys. Many of these features or properties interact directly with hydrogen by increasing trapping density, altering cohesive forces, or affecting hydrogen mobility[2, 13]. However, only a very limited body of work addressing variation in MBN and/or MAE[14–16] behavior with hydrogen content is currently available in literature. It is therefore prudent to explore in greater detail the theoretical and practical aspects of the determination of magnetic properties for the purposes of hydrogen characterization.

CHAPTER 2

REVIEW OF RELEVANT THEORY

Successful development of a nondestructive technique for diffusible hydrogen determination in steel necessarily relies on sufficient understanding of the underlying phenomena as relate to hydrogen mobility in the medium and effects of its presence on measured material parameters. This chapter addresses the issue of hydrogen transport as a diffusional process delayed by local traps in the framework of McNabb and Foster [17], Oriani [18] and presents predicted behavior of this model. Discussion then turns to effects of hydrogen on the ferromagnetic behavior of iron and low alloy steel at the microscopic level as by perturbation of local atomic moments, followed by a discussion of dynamic effects in the form of domain wall interactions.

2.1 Hydrogen Transport

Work reported in the mid twentieth century by Darken and Smith[19] pertaining to the diffusion of hydrogen in steel demonstrated peculiar and puzzling behavior. Slab-like steel samples, when subject to asymmetric boundary conditions (i.e. zero and non-zero hydrogen concentration on either face) did not exhibit a linear concentration gradient, which would give a mean value of one half in accordance with Fick's laws, but was instead closer to 85%. Further, hydrogen was absorbed *into* a sample faster than it was desorbed—ultimately revealing the inadequacy of any theoretical treatment which uses a constant diffusivity for hydrogen transport in steel. Since the concentration of hydrogen encountered in ferrous materials is extremely low, making interactions between solute atoms an unlikely culprit, it was then proposed that hydrogen diffusion must be impeded by various “traps” in the microstructure: a theory which has since been developed extensively and is widely accepted as congruent with observed behavior.

2.1.1 Hydrogen Trapping

A general treatment of the trapping of hydrogen in metals is attributed to McNabb and Foster[17] which incorporates the foregoing observations into a physical system which is described as follows. Within a material, there exist defects which are capable of locally inhibiting the transport of hydrogen atoms. The degree of trapping classifies these features into shallow (with negligible delay), sinks (the delay is permanent), and active. It is the last of these types that is most relevant to the present discussion, and gives rise to two distinct populations of diffusible hydrogen, coupled by the reaction, $H + X \rightleftharpoons H_X$, where H is a hydrogen atom diffusing according to Fick's laws and X is a trapping site.

Transitions from freely-diffusing (lattice) to trapped populations are described by the rate equation[17],

$$\frac{\partial n}{\partial t} = kc(1 - n) - pn, \quad (2.1)$$

for the fraction n of filled traps and c diffusible atoms of hydrogen per unit volume, and where k and p are the trap and release rate probabilities, respectively. This rate is coupled with Fickian behavior for the diffusing population,

$$\frac{\partial c}{\partial t} + N \frac{\partial n}{\partial t} = \nabla \cdot (D \nabla c), \quad (2.2)$$

with a total trap density of N per unit volume, and ordinary diffusivity D . Consistent with observations that trapping is the rate-limiting step when compared with surface conditions[19], boundary effects are neglected.

In general, Equations (2.1) and (2.2) are without a closed-form solution. Approximations can be applied to facilitate analysis, for example evaluating the behavior of slabs as $t \rightarrow \infty$, which gives meaningful results for comparison with steady-state permeability experiments. Alternatively, the imposition of local equilibrium conditions between hydrogen populations

in Equation (2.1) gives rise to an apparent or *effective* diffusivity, D_{eff} , and this description was determined to be applicable to a variety of existing data sets by Oriani[18]. While the condition of equilibrium would seem to imply static conditions, i.e. $\partial n/\partial t = 0$, this notion is only valid in the neighborhood of a trapping site. Lattice diffusion continues for the untrapped hydrogen population, while local X sites act as sinks.

If this equilibrium constant is given by the ratio of activities for the lattice and trapping sites,

$$K = \frac{k}{p} = \frac{1}{\theta_L} \frac{\theta_X}{1 - \theta_X}, \quad (2.3)$$

where θ_i is the occupancy fraction of site i , i.e. $\theta_X = n$ in equation Equation (2.1) above, the effective diffusion constant then becomes

$$D_{eff} = D \frac{dc_L}{dc_X} = D \left[1 + \frac{N_X N_L K}{(N_L + K c_L)^2} \right]^{-1}, \quad (2.4)$$

for concentrations c and sites per volume N of lattice (L) and trapping (X) sites, taking approximate values,

$$D_{eff} \approx D \frac{c_L}{(c_X - \theta_X c_X)} = D_{abs} \quad (\text{absorption}) \quad (2.5)$$

$$D_{eff} \approx D \frac{c_L}{c_X} = D_{des}, \quad (\text{desorption}) \quad (2.6)$$

from which it is clear that $D_{abs} > D_{des}$.

Following the assumption of Arrhenius behavior for trapping, i.e. that the binding energy E_X for a trap imposes a rate $\mathcal{R} = \nu \exp(E_X/RT)$, where ν is the jump frequency of a hydrogen atom, Oriani gives bounds on the applicability of the assumption of local equilibrium[18],

$$\frac{\delta c_X}{\mathcal{R}N_X\theta_X} \leq \frac{10^{-2}l^{-2}}{D}, \quad (2.7)$$

for an incremental change in concentration δc_X and reference length l (e.g. half-thickness of a plate, radius of cylinder, etc.).

To provide some practical insight into the behavior of hydrogen diffusion in the samples of this study, numerical simulations of the foregoing discussion were performed, subject to the bounds of local equilibrium from the inequality Equation (2.7) for various charging/discharging conditions, the results and discussion of which are presented in Section 2.1.2.

It should be no surprise that the precise nature of hydrogen traps in steel (as with other materials) remains the subject of considerable discussion. Hirth[2], in addition to a thorough review of the various physical effects of hydrogen on steel, discusses and tabulates the various types of hydrogen traps and their respective energies, which can range from about 3–100 kJ mol⁻¹. The following analysis takes on the values of 17, 20, and 23 kJ mol⁻¹ for the computation of K , which correspond roughly to the binding energy for hydrogen and a dislocation. Such a choice of trapping site is somewhat arbitrary, but the discussion is strictly intended to illustrate effects of *changes* in the parameters on the behavior of hydrogen diffusion, which will be relevant later as experimental data is discussed.

2.1.2 Modelling Hydrogen Absorption and Desorption

Solution of Equations (2.1) and (2.2), subject to the constraint of local equilibrium, Equation (2.3) were implemented in Python² for sample cross sections of 9 × 9 mm (assuming infinite length) and various values of K , D_{eff} , and t_{chg} , the electrolytic charging duration. Spatial (a 2D 75 × 75-point grid) and temporal approximations of the derivatives were made by finite difference and fourth order Runge-Kutta methods, respectively[20], with time steps limited by the condition $\delta t = 0.9\delta x^2/(2D_{eff})$. To reflect the conditions encountered in experiments performed, the following boundary conditions were imposed,

²Using the numerical libraries NumPy/SciPy. It would take forever otherwise.

$$c_{t=0} = 0 \tag{2.8}$$

$$c_{x,y=\pm l} = \begin{cases} c_0 & 0 < t \leq t_{chg} \\ 0 & t > t_{chg} \end{cases}, \tag{2.9}$$

for a surface concentration $c_0 = 0.2 \text{ mol m}^{-3}$ during charging[21].

For lower values of the effective diffusivity, $D_{eff} = 0.5 \text{ m}^2 \text{ s}^{-1}$ and equilibrium constant, $K = 1.67 \times 10^{-4}$ (corresponding to a binding energy of 23 kJ mol^{-1}), Figure 2.1 demonstrates the effect of trapping on the hydrogen concentration in cross sections of the rectangular samples. On charging for two hours ($t_{chg} = 7.2 \text{ ks}$, hydrogen is limited to the regions of the sample near the surface (note the times in each image are doubled; the final image describes the state at $t = t_{chg}$). When the boundary concentrations are reset to zero concentration, however, the hydrogen remains stuck, continuing to slowly diffuse into the center of the sample and resulting in very inhomogeneous distribution of hydrogen with high concentrations in the corners where the effect is most intense.

Increasing the diffusivity by a factor of four and reducing the binding energy to $E_X = 17 \text{ kJ mol}^{-1}$ results in more homogeneous behavior, as demonstrated in Figure 2.2. Hydrogen quickly enters the steel as one expects for a higher diffusivity and penetrates throughout by the end of charging, but it remains locked within the sample for longer. Concentration at the center continues to rise as before, such that profiles for $t = 1000 \text{ s}$ and 8000 s become nearly inverses of one another.

To elucidate the apparent differences in behavior between surface and bulk concentrations, Figures 2.3 and 2.4 present the time evolution of concentration of these locations for values of $D_{eff} = 0.5$ and $2.0 \times 10^{-9} \text{ m}^2 \text{ s}^{-1}$, respectively. The surface concentration, c_{surf} is evaluated as a single point at the coordinate ($x = -l, y = 0$), while the middle concentration c_{mid} is the average of the central 16% (i.e. 30×30 -point grid) of the cross section. Vertical lines indicate the charging times of 30, 60, and 120 minutes used in the experiments of this

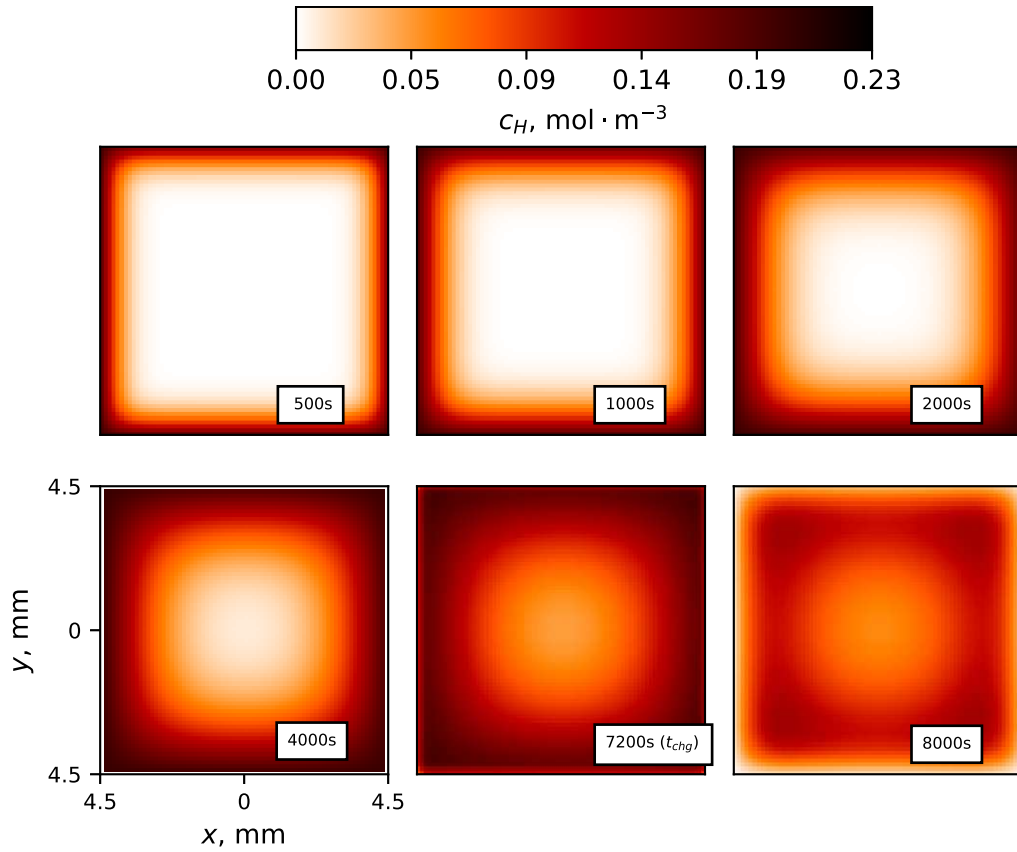


Figure 2.1: Hydrogen concentration profile for various times during charging ($t_{ch} = 120 \text{ min}$) and discharging as obtained via numerical solution. The differential equations of the Oriani model[18] were approximated by fourth order Runge-Kutta method with $K = 1.67 \times 10^{-4}$, $D_{eff} = 0.5 \times 10^{-9} \text{ m}^2 \text{ s}^{-1}$.

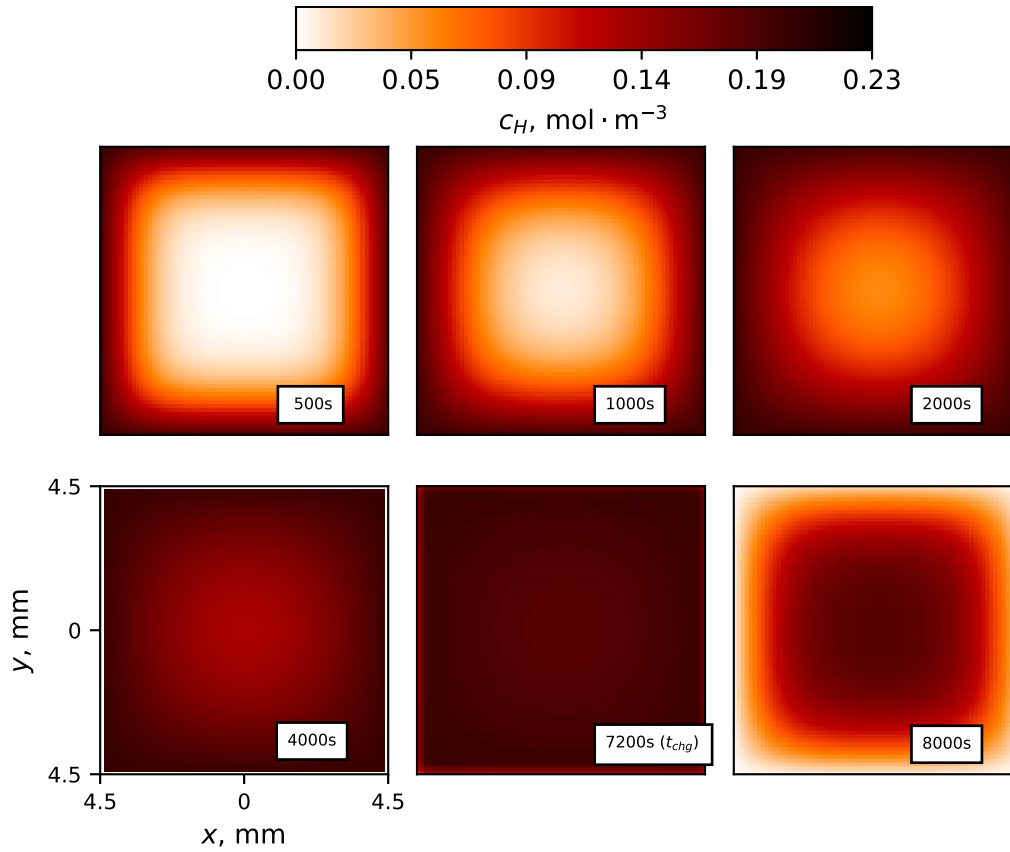


Figure 2.2: Hydrogen concentration profile for various times during charging ($t_{ch} = 120 \text{ min}$) and discharging as obtained via numerical solution. The differential equations of the Oriani model[18] were approximated by fourth order Runge-Kutta method with $K = 1.61 \times 10^{-3}$, $D_{eff} = 2.0 \times 10^{-9} \text{ m}^2 \text{ s}^{-1}$.

study. (For reference, Figure 2.1 corresponds to Figure 2.3, top right; Figure 2.2 is the profile for Figure 2.4, bottom right.)

In terms of microstructure and the applicability of the range of values for the parameters considered, Sakamoto provides some useful data obtained from permeability experiments for carbon steel[22] and high strength Cr–Mo and Ni–Cr–Mo steel of nominal composition identical to those steels used in this study (AISI 4140 and 4340 steel)[23]. Following quenching in oil, higher tempering temperatures increase the effective diffusivity (D_{eff}) while decreasing solubility (c_0). For carbon steel these effects are monotonic, while for alloy steels there is a local minimum (maximum) in D_{eff} (c_0) near $T_{temp} = 250^\circ\text{C}$, a feature which has also been observed for Russian 40KhN alloy of comparable composition to 4130 steel[24]. Numerical values for D_{eff} obtained by Sakamoto ranged from $0.01\text{--}1.0 \times 10^{-9} \text{ m}^2 \text{ s}^{-1}$ —the higher range being reported for $T_{temp} \approx 800^\circ\text{C}$. For the experiments considered here, the behavior of Figure 2.3 is expected for lower tempering temperatures with a lower effective diffusivity and as-quenched samples while Figure 2.4 should be more applicable to higher tempering temperatures. As will be addressed in Chapter 4, however, the influence of additional trapping sites (for example, those generated by carbides on tempering) and the complexities of magnetoacoustic emission obfuscate naive assessment of the data.

The distinction between surface and central concentration profiles is immediately relevant to MAE/MBN behavior as will be discussed in Section 2.2: Barkhausen emissions are sensitive only to surface layers on the order of $100 \mu\text{m}$ or less due to the skin effect, while MAE is a bulk phenomenon. Indeed, much of the behavior observed experimentally in this study are reproduced qualitatively in these numerical simulations, thus for the purposes of discussion it is worth considering the behaviors separately.

At the surface, the abrupt change in boundary conditions at the termination of charging (t_{chg}) is more readily apparent given the relative lack of surrounding material. For the parameters considered, the traps are essentially saturated near the surface, and evolution of hydrogen is more or less as expected. Though not readily visible as presented, an increased

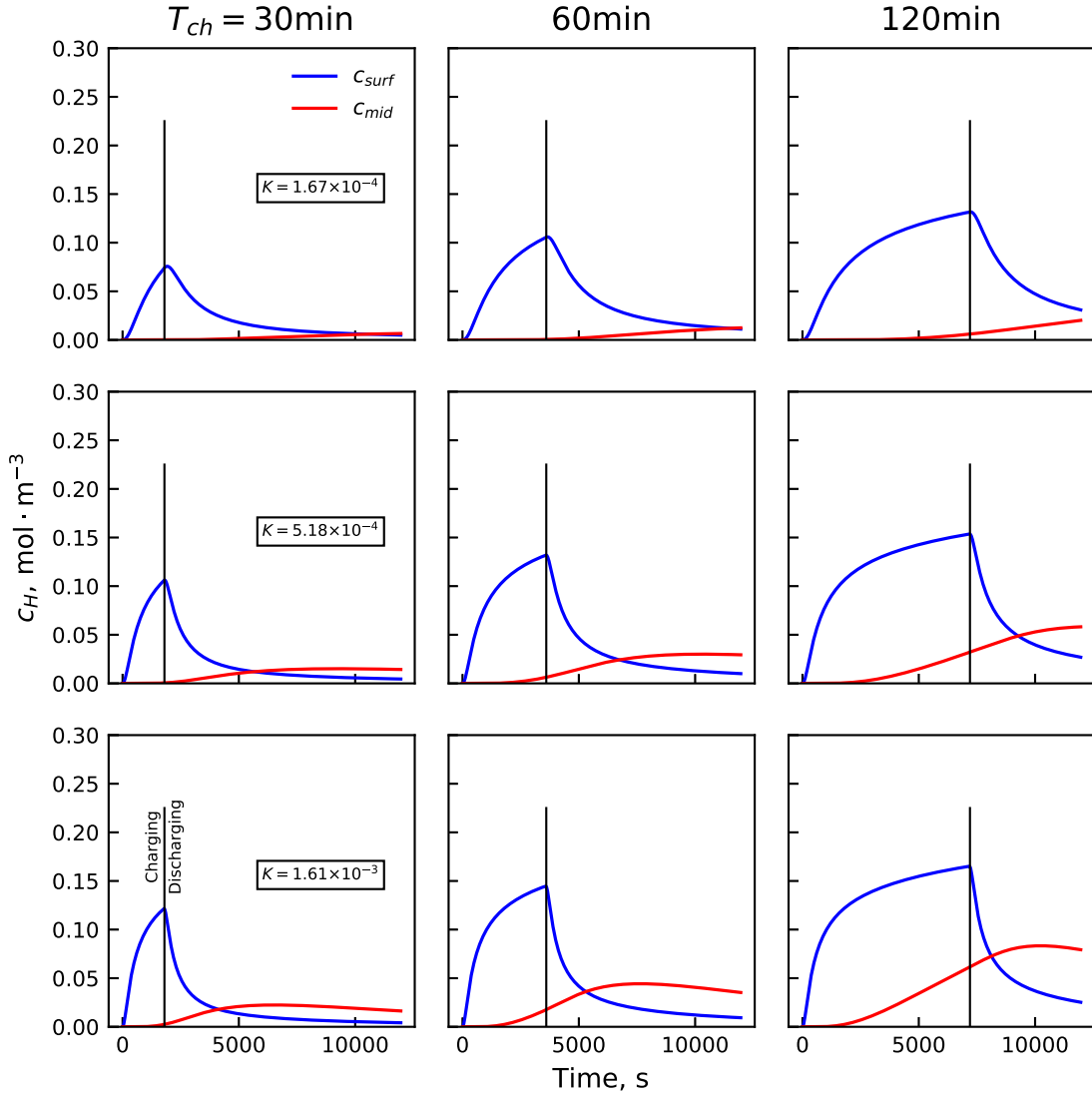


Figure 2.3: Predicted hydrogen concentration for $9 \times 9 \times 20$ mm during a charging and discharging cycle for various trapping parameters and charging times for a diffusivity of $D_{eff} = 0.5 \times 10^{-9} \text{ m}^2 \text{ s}^{-1}$. The results are solutions of the McNabb-Foster relations Equations (2.1) and (2.2), subject to local equilibrium constraints Equation (2.3) developed by Oriani[18].

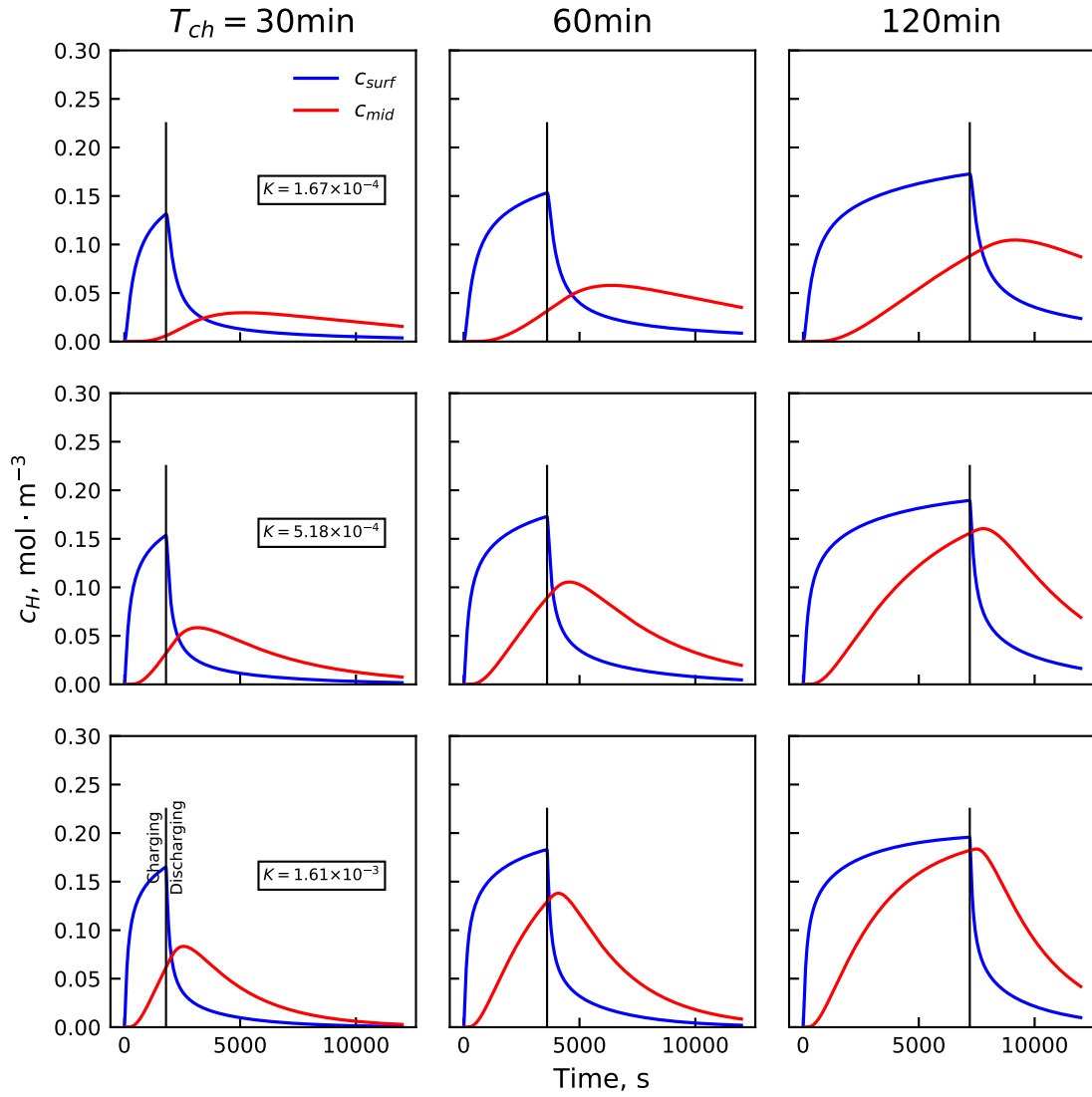


Figure 2.4: Predicted hydrogen concentration for during a charging and discharging cycle for various trapping parameters and charging times for a diffusivity of $D_{eff} = 2.0 \times 10^{-9} \text{ m}^2 \text{ s}^{-1}$. The diffusion simulation is performed by computing the Oriani model[18] subject to the same parameters and constraints as Figure 2.3, apart from a four-fold increase in D_{eff} .

trapping constant K results in greater asymmetry in the charging-discharging profiles, one of the hallmarks of hydrogen diffusion in steel[19]: the time required to charge to, say, 50 % of peak hydrogen is less than the time to evolve the same fraction. An increased diffusivity makes this behavior more apparent as the consequences of trapping are more immediate.

Towards the middle of the sample, however, the effects of trapping and delay give rise to more interesting diffusional behavior. Following charging, the central concentration continues to rise, delayed by up to several hours for low K and low D_{eff} (Figure 2.3). Higher diffusivities sharpen and move this peak closer to t_{chg} , while increasing K causes a broadening of the peak and increase in height relative to c_{surf} . Quite remarkably, the characteristic behaviors and their variations expressed in these models will again be demonstrated by the periodic measurements of magnetic properties over time following charging in Chapter 4.

2.2 Hydrogen and Ferromagnetism in Iron

Equipped with an understanding of the diffusional qualities of hydrogen in steel, attention is now turned to what effects hydrogen itself might have on the magnetic properties of the steel it inhabits. Here a broad overview of the phenomenological processes underlying the Barkhausen effect, magnetoacoustic emission, and magnetic hysteresis are described, beginning with a brief description of ferromagnetism as it occurs in the transition metals. Though not intended to be a rigorous treatment of ferromagnetic behavior (as one might find in treatises on the subject by Chikazumi [25], Cullity [26], Jiles [27], and others), the following discussion provides much-needed background on what mechanisms can be attributed to the features explored by experiment later in this project.

Phenomenologically, ferromagnetic behavior is observed when atomic magnetic moments \vec{m} align themselves spontaneously with the moments of neighboring atoms as a result of the exchange interaction. The extent of this ordering is long-range (i.e. tens to hundreds of atoms in each direction), but in order to minimize the magnetostatic energy which arises from free poles at transitions, does not continue indefinitely. Instead, small regions called magnetic domains emerge in which all magnetic moments of the atoms within collectively

have the same magnetization direction. On a macroscopic scale, the bulk magnetization sums to zero in such a material, but on exposure to a sufficient external magnetic field \mathbf{H} , these domains begin to align themselves in the direction of the applied field and the bulk takes on a finite magnetization \mathbf{M} .

In general, magnetic domains do not necessarily coincide with the grain structure of a crystalline material, except by coincidence of crystallographic orientation with a magnetic “easy axis”. Whether a crystallographic axis is preferred is dependent on the electronic symmetry of the lattice; departures of the magnetic moment from the easy axis will increase the magnetic anisotropy energy. Regions between magnetic domains are termed domain walls and are usually modelled as semi-flexible, elastic membranes pinned by inhomogeneities and defects in the material. Domain wall thickness is dependent on a variety of factors, being a balance of exchange, magnetostatic, magnetic anisotropy, and coupled external (e.g. strain) energies[27].

In consideration of the impacts of hydrogen on the dynamic magnetization behavior of iron and its dilute alloys, the remainder of this chapter will address the following microscopic details of the electronic nature of ferrous materials,

1. Magnetic moments at the atomic level: how might hydrogen alter the magnetic susceptibility?
2. Domain walls: how does hydrogen affect the magnetic anisotropy in iron crystals?
3. Interatomic forces: will hydrogen change the elastic constants or magnetostriction significantly?

Points 1 and 2 will underpin all magnetic behavior considered in this study, as both MBN and MAE share a common origin in iron: domain wall motion. The final point is restricted to MAE, as it is the magnetostriction which causes the acoustic strain; magnetostriction itself being a coupled phenomenon between elasticity and magnetic anisotropy effects.

2.2.1 Ferromagnetism

Spontaneous alignment of magnetic moments between neighboring atoms occurs as a result of the exchange interaction among electrons, a consequence of Pauli exclusion. According to the Heisenberg model of ferromagnetism, two (spatially) overlapping atomic orbitals with wave functions $\psi_a(r_1)$ and $\psi_b(r_2)$, and electron spins \vec{s}_i must be antisymmetric to ensure that the observed wave function $\psi_a^*\psi_b$ remains symmetric on interchange of electrons 1 and 2 while guaranteeing $\psi_a(r_1)\psi_a(r_2) \equiv 0$ (that is, the Pauli exclusion principle). The exchange energy is then $E_{ex} = -2J\vec{s}_1 \cdot \vec{s}_2$, where J is the exchange integral,

$$J = \int \int [\psi_a^*(r_1)\psi_b^*(r_2)] \langle H_{12} \rangle [\psi_b(r_2)\psi_a(r_1)] d\tau_1 d\tau_2, \quad (2.10)$$

with generalized wavefunction coordinate vectors τ_j and the interaction operator is the Bethe Hamiltonian[27],

$$\langle H_{12} \rangle = \left[\frac{1}{r_{ab}} - \frac{1}{r_{a2}} - \frac{1}{r_{b1}} + \frac{1}{r_{21}} \right].$$

for atomic orbitals a, b and electrons 1, 2. In practice, Equation (2.10) is only meaningful with well defined orbitals, and calculations of the J directly are even then of only limited utility in very simple systems. Nevertheless, the Heisenberg model was sufficient to demonstrate the existence of $J > 0$ necessary for ferromagnetism in the ferrous elements, and it remains useful for understanding the origins of the exchange interaction which constitutes a delicate and rather peculiar feature of quantum mechanics[25].

The nature of interatomic bonding has a significant impact on the delicate balance of electrons and therefore magnetic behavior. For strongly overlapping bonds, occurring as hybrids of s-, p-, and d-orbitals, exchange integrals are negative and large owing to Pauli exclusion. For electrons which do not participate, i.e. those which remain unpaired in the 3d-orbitals for ferrous alloys, the exchange energy can be positive[28]. Thus, these two classes

of orbitals—bonding (interatomic) and unpaired (magnetic)—and the associated electronic density of states determine ferromagnetic behavior in a material and its magnetic susceptibility. On partial dissociation of a hydrogen atom into an iron matrix, the electron contributes to the d-band, while the proton enters the lattice as an interstitial, concomitant with strain at the tetragonal sites[13]. Introduction of highly localized charges and stresses from hydrogen atoms has been observed to perturb these qualities commensurate with changes to ferromagnetic quantities in iron.

In the ferrous alloys of iron, cobalt, and nickel, it is the unpaired itinerant 3 d-electrons which participate in ferromagnetism: when the energy required to move electrons from a negative spin band to the positive band at the Fermi energy level E_F is less than the exchange energy gained, spontaneous alignment of atomic magnetic moments occurs, and ferromagnetic behavior becomes the preferred configuration. The increase in magnetization is proportional to the resulting number of unpaired electrons in the d-band[29],

$$M = \mu_B (N_+ - N_-) ,$$

where μ_B is the Bohr magneton and the number of electrons in the band is computed with respect to the density of states (DoS), $g(E)$:

$$N_{\pm} = \int_{-\infty}^{+\infty} g_{\pm}(E) f(E_f \pm \mu_B H_m) dE ,$$

where H_m is the Weiss molecular field and the Fermi-Dirac distribution is

$$f(E) = \left[\exp \left(\frac{E - E_f}{kT} \right) + 1 \right]^{-1} .$$

The DoS has been computed for BCC iron by a number of techniques; Figure 2.5 gives two such calculations for the separate spin bands as prepared by Hathaway et al. [30] and the effect of a hydrogen atom at octahedral (O) and tetrahedral (T) sites using the computed

total DoS of Itsumi and Ellis [31]. For pure nickel the difference in unpaired electrons yields a value is $0.61\mu_B$ and $2.2\mu_B$ for iron (μ_B the Bohr magneton). Addition of a single atom to the 32-atom supercell used in the calculation causes several slight changes the distribution of electron states, shown as the difference between the DoS for pure iron and that for O and T sites in the bottom graph of Figure 2.5. Energies above $(E - E_F) \approx -4$ eV, in the range of 3d-orbitals, witness a shift in energy downwards, suggesting a tendency towards paired spins in these orbitals, and therefore a reduction in spontaneous magnetization. New peaks in the DoS are also observed for tightly bound electrons of the hydrogen 1s- and iron 4s-orbitals around -10 eV, which play an important role in the nature of bonds and embrittlement as discussed by Itsumi and Ellis [31].

In early reports, hydrogen was observed to dramatically increase the permeability, μ , of pure iron when introduced via high pressure gas[32]. However, this particular observation was ultimately attributed to purification of the alloy by hydrogen in later work, and the permeability was found to decrease with hydrogen at higher concentrations[33].

Recent *ab initio* work has suggested that the net effect of hydrogen depends also on the local conditions: the interstitial has a negative or positive impact on μ if it is situated on a tetragonal or octahedral site, respectively, and whether or not vacancies or non-Fe atoms are present[34]. Additional electronic calculations involving hydrogen atoms in or around grain boundaries[35] and vacancies[31] reveal something of the nature of charge transfer and changes to the DoS in iron. Bonds are formed primarily by hybridization of hydrogen 1s and 4s electrons below E_F in iron, thereby weakening the surrounding metallic structure. The extent to which this softening occurs depends again on the surrounding lattice, but in any case results in a decrease in the local magnetic moment.

2.2.2 Magnetic Domains

Despite a stable configuration of mutually-aligned orbitals, ferromagnetic materials do not exhibit macroscopic magnetization without prior application of an externally applied field, \mathbf{H} . The physical origin of this behavior lies in the magnetostatic energy,

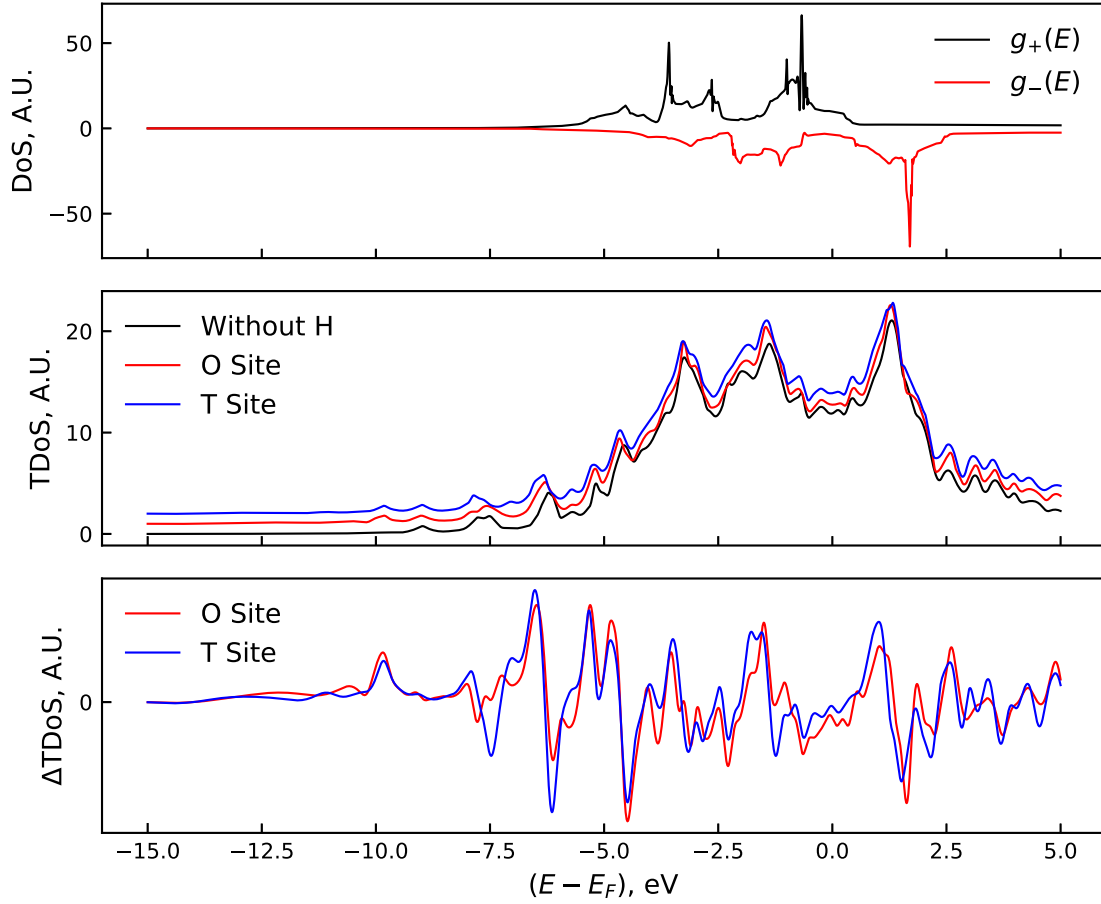


Figure 2.5: Electronic Density of States for BCC iron (above, with spin state)[30] and a Fe_{32}H supercell (center)[31] from local-spin-density functional theory. The change in total density of states due to the introduction of a single hydrogen atom in the supercell at the octahedral (O) and tetrahedral (T) site is shown in the bottom subfigure.

$$E_{ms} = - \int \mu_0 \mathbf{M} \, d\mathbf{H}, \quad (2.11)$$

per unit volume for magnetization \mathbf{M} and field \mathbf{H} . In the absence of an external field, \mathbf{H} is the demagnetizing field $\mathbf{H}_d = -N_d \mathbf{M}$, giving $E_{ms} = \mu_0 N_d \mathbf{M}^2$, where N_d is a geometric demagnetizing factor. As the size of a region of uniform magnetization grows in favor of the exchange energy, so must the magnetostatic energy. To balance these energies, the magnetization will divide into distinct regions known as magnetic domains as shown schematically in Figure 2.7(A).

In the (macroscopically) unmagnetized state, the initial orientations of each domain are random and can vary even within a crystallographic grain. Moment alignment relative to the crystal lattice is determined by the magnetic anisotropy energy, which for a cubic crystal is expressed as a power series in direction cosines,

$$\begin{aligned} E_a = & K_1(\alpha_1^2 \alpha_2^2 + \alpha_2^2 \alpha_3^2 + \alpha_1^2 \alpha_3^2) \\ & + K_2 \alpha_1^2 \alpha_2^2 \alpha_3^2 \\ & + K_3(\alpha_1^2 \alpha_2^2 + \alpha_2^2 \alpha_3^2 + \alpha_1^2 \alpha_2^2)^2 + \dots, \end{aligned} \quad (2.12)$$

where K_1 , K_2 , K_3 are cubic anisotropy constants. The sign of K_1 determines the “easy magnetization axis”. In the case of α -iron, where $K_1 = 4.72 \times 10^4 \text{ J m}^{-3} > 0$, moments align *with* the $\langle 100 \rangle$ crystallographic directions. By contrast, K_1 for nickel is $-5.7 \times 10^3 \text{ J m}^{-3}$, so that the easy axes are the $\langle 111 \rangle$ directions[25].

The physical origins of magnetic anisotropy lie in the directional dependence of the spin-pair potentials w given as a polynomial expansion,

$$w(\cos \varphi, r) = P_g(r) + P_l(r) \left(\cos^2 \varphi - \frac{1}{3} \right) + P_q(r) \left(\cos^4 \varphi - \frac{6}{7} \cos^2 \varphi + \frac{3}{35} \right) + \dots, \quad (2.13)$$

where P_i are Legendre coefficients³ in the expansion about φ : the angle between the spin moment and crystal axis. The first term corresponds to the exchange energy and is therefore independent of direction (i.e. isotropic). The second term behaves analogously with dipole-dipole interactions, and is usually referred to as such. However, because direction cosines of second order vanish over all directions, i.e. $E_a = \sum \alpha_i^2 - \frac{1}{3}$, the dipole-dipole term vanishes for high-symmetry crystals. Thus, in the absence of a strain which would break this symmetry, the magnetic anisotropy energy is due entirely to spin-orbit coupling[36]. Discussion of the strain effects is continued in Section 2.2.4 with regard to magnetostriction. While not necessary for the discussion of magnetic anisotropy, an explicit dependence on the interatomic distance r is made for the expansion coefficients, as this same pair potential is sufficient in elucidating much of the same behavior of magnetostriction in Section 2.2.4.

Zones of transition between domains are termed Bloch or domain walls (DWs), and consist of regions of continuous rotation of the local magnetic moments from one domain to the next, as shown schematically in Figure 2.6 for a 180° DW. The thickness of the transition region is determined by the balance of anisotropy and exchange energies:

$$\delta = \pi \sqrt{\frac{Js^2}{Ka}}, \quad (2.14)$$

for the exchange integral J , spin s ($= 1$ for BCC iron), and lattice constant a . Thus, as the anisotropy energy becomes more dominant, a more gradual transition region (thicker DW) which would otherwise be favored by the exchange term, becomes more energetically costly, and a thinner wall results.

As an abstraction of an underlying physical concept, DWs exhibit some behaviors analogous to dislocations—notably translation, friction, and pinning by defects in the material. Figure 2.7(B-C) provides illustration of these responses to external fields. Those domains

³In the work by Chikazumi [25], P_g and P_l are denoted only by their subscripts. In the case of $P_l = l$, however, the choice is rather unfortunate as l refers to length in the same formulæ; P_i is used here for clarity.

which are favorably aligned to \mathbf{H} will grow at the expense of less favorable domains, but defects and inclusions (or other magnetic constraints) impede DW translation, resulting in bowing out (similar to the response of a dislocation to stress). When a critical field is exceeded, the DW unpins and translates fully until pinned by another defect (Figure 2.7(C)). The discontinuous translation of DWs is one mechanism which gives rise to the Barkhausen effect, and it is the dependence on defects and microstructure which lends MBN utility as a nondestructive technique.

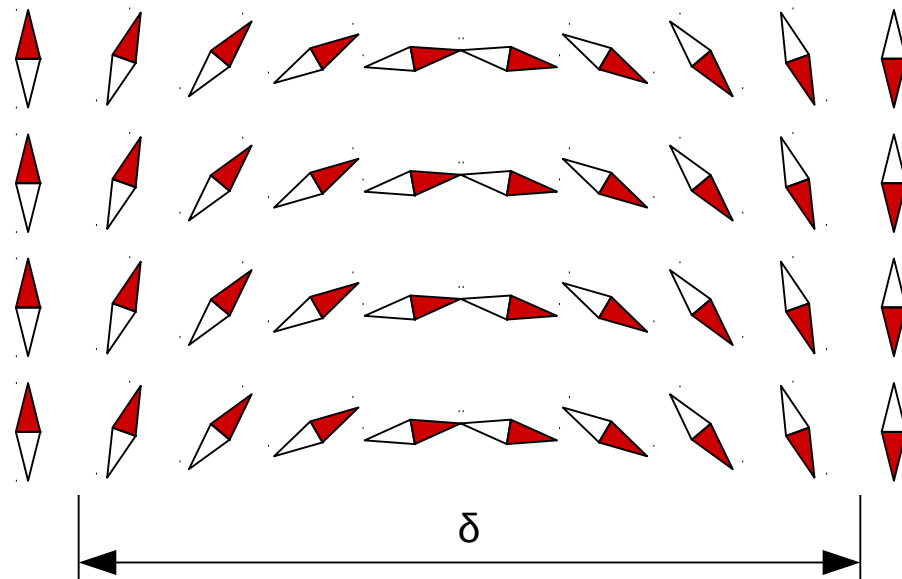


Figure 2.6: Illustration of magnetic domain (Bloch) wall. Arrows indicate the local magnetic moment, corresponding to two domains (i.e. $\uparrow \downarrow$) with a region of continuous variation between. After Chikazumi [25].

2.2.3 Domain Wall Dynamics: Barkhausen Noise

When an external magnetic field is imposed on a material consisting of randomly-aligned magnetic domains, the distribution of their orientation and geometries are affected. At low field strengths domains will rotate slightly toward the direction of the field and walls will bow out from their pinning sites; removal of the external field allows the domains to relax and the

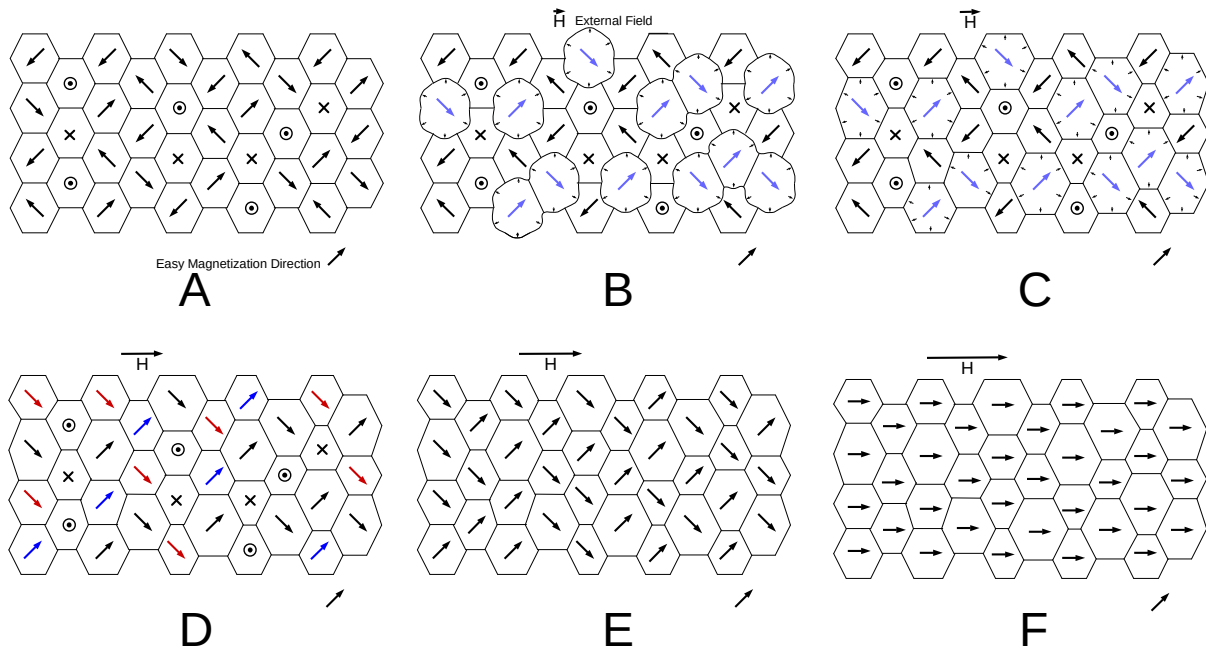


Figure 2.7: Schematic illustration of the various stages of magnetization of a ferromagnetic structure. A crystal with cubic symmetry and easy axis in the relaxed, unmagnetized state (A) is subjected to a small externally applied field, \vec{H} , which causes domain walls to bow out into domains which are not favorably aligned (B). Increasing the field causes domain walls to become unpinned, allowing growth of favorably-aligned domains (C). Further increase in field strength causes rotation of opposing domains to an easy axis in the direction of magnetization (D). Less favorable domains (in and out of paper) are rotated next (E). Finally, all domains are rotated away from the easy axis to align with the external field (F). After Jiles [27].

process is reversible. As the applied field is increased, domains can rotate from their current axis of easy magnetization to one better aligned with the external field (Figure 2.7(D-E)) and domain walls can break free from pinning sites as this process becomes energetically favorable (Figure 2.7(C)). The rapid motion (rotational or translational) perturbs the magnetic field in and around the material, and can be observed as discontinuities in the magnetization curve or as emissions detected by a search coil near the surface.

Motion of domain walls during magnetization is in general a largely stochastic process, making a tractable analysis from first principles difficult. One successful approach, referred to by its author's initials as the ABBM⁴ model, considers the random component as a stationary Wiener-Lévy perturbation $W(\Phi)$ to a linear relaxation relationship[37],

$$\frac{dH_c}{d\Phi} + \frac{H_c - \langle H_c \rangle}{\xi} = \frac{dW}{d\Phi}, \quad (2.15)$$

for applied field $H = H_a + H_m$, and correlation length, ξ . The explicit dependence of the stochastic element on the flux Φ instead of time is the source of intermittent behavior, as the coercive field H_c is dependent on the domain wall position.

While the power law relationships for the distributions of avalanche size s , duration T , and energy E , are predicted[37] and observed[38–40] to scale as

$$P(s) \sim s^{-\tau} g_1(s/s_0) \quad (2.16)$$

$$P(T) \sim T^{-\alpha} g_2(T/T_0) \quad (2.17)$$

$$P(E) \sim E^{-\epsilon} g_3(E/E_0), \quad (2.18)$$

the physical origin of their exponents τ , α , and ϵ and cutoffs s_0 , T_0 , and E_0 is unclear⁵. Evaluation of the magnetostatic, demagnetizing, surface tension, and dipolar interaction energetics by [38] applied to an elastic interface in a disordered medium resulted in a model which

⁴Alessandro, Beatrice, Bertotti, and Montorsi

⁵Here τ is understood to refer to the scaling exponent in the notation of that particular field of study and does not refer to relaxation time.

reproduced much of the same character of the ABBM model, but successfully predicted the exponents as well, namely $\tau = 3/2$ and $\alpha = 2$ for the critical dimension $d = 3$ [38]. These results, along with a linear dependence on \dot{M} , are specific to a particular class of materials which exhibit grain-like structure. For homogeneous, isotropic materials (e.g. amorphous magnetic alloys) the values otherwise take the values $\tau = 5/4$ and $\alpha = 10/7$, independent of driving frequency[39].

For cyclic fields, differentiation of Equation (2.15) with respect to time gives the dynamic equation

$$\frac{d\dot{\Phi}}{dt} + \frac{\dot{\Phi} - S\dot{M}}{\tau} = -\frac{1}{\sigma G} \frac{dH_c}{dt}, \quad (2.19)$$

for magnetization rate \dot{M} and time constant $\tau = \sigma G S \mu$. The conductivity σ , permeability μ , and DW cross-sectional area S constitute the pertinent intrinsic quantities while G is a geometric factor. Solution of Equation (2.19) for Barkhausen jump magnitude as the critical time constant $\tau_c = \xi/S\dot{M}$ becomes large yields power law relationships (widely observed in practical application[38]) with power density[37],

$$P_{\Phi}(\omega) = \frac{4AS\dot{M}}{(\sigma G)^2} \frac{1}{\omega^2 + \tau^{-2}}, \quad (2.20)$$

where A is a parameter that describes short range H_c interactions. Alternatively, in the limit of high DW velocities, the power spectrum becomes

$$P_{\Phi}(\omega) = \frac{4AS\dot{M}}{(\sigma G)^2} \frac{\omega^2}{(\omega^2 + \tau^{-2})(\omega^2 + \tau_c^{-2})}. \quad (2.21)$$

Between Equations (2.20) and (2.21), the latter expression finds more applicability in this study owing to the relatively high magnetizing frequency $f_d = 24$ Hz. The peak in the power spectrum of Equation (2.21) is

$$\max P_{\Phi} = \frac{4ASM}{(\sigma G)^2} \frac{1}{(\tau^{-1} + \tau_c^{-1})^2}$$

with frequency,

$$\omega_{max} = \frac{1}{\sqrt{\tau\tau_c}}; \quad (2.22)$$

Introduction of hydrogen into the matrix will inhibit the direct translation of domain walls by pinning, and favor domain nucleation over growth. In terms of the parameters of Equation (2.22), a reduction in the values of cross sectional area S and correlation length ξ might be expected (in addition to a decrease in permeability μ described previously) resulting in an overall decrease in MBN activity with hydrogen concentration. However at higher frequencies, as noted by [37], the power spectrum is dominated by the coercive field interactions described by the parameter A , and (as will be discussed in Section 2.2.6) this value is likely to be strongly positive-correlated with hydrogen concentration as it relates directly to domain wall mobility. Indeed, available reports[14, 15] and experiments in this study suggest that hydrogen increases Barkhausen response in steel.

2.2.4 Magnetostriction

Mechanical strain and magnetization are coupled through the magnetostrictive effect which has its origins in magnetic anisotropy as described in the spin-pair potential function of Equation (2.13) via an explicit dependence of the Legendre coefficients on the interatomic distance r . Both the exchange term (P_g in the Legendre expansion) and dipole-dipole terms (P_l, P_q, \dots) are assumed to be functions of this distance, but explicit angular dependence is confined only to the latter. Thus, P_g corresponds to a strictly isotropic volume magnetostriction, while the behavior of P_l (ignoring higher order terms) determines the anisotropic magnetoelastic effect. More precisely, for the direction cosines $\alpha_{\{1,2,3\}}$ and $\beta_{\{1,2,3\}}$ for domain

magnetization and interatomic bonds, respectively, a strain e contributes energy[25, 36],

$$E_{mag-el} = B_1 \left[e_{xx} \left(\alpha_1^2 - \frac{1}{3} \right) + e_{yy} \left(\alpha_2^2 - \frac{1}{3} \right) + e_{zz} \left(\alpha_3^2 - \frac{1}{3} \right) \right] + B_2 (e_{xy}\alpha_1\alpha_2 + e_{yz}\alpha_2\alpha_3 + e_{zx}\alpha_3\alpha_1) , \quad (2.23)$$

where the form of the coupling coefficients B_1 and B_2 in general depends on the nature of symmetry in the crystal lattice. For BCC these quantities are related to the nearest neighbors N at the unstrained distance r_0 by[25]

$$B_1 = \frac{1}{2}N \left[6P_l + \left(\frac{\partial P_l}{\partial r} \right) r_0 \right] \quad (2.24)$$

$$B_2 = N \left[2P_l + \left(\frac{\partial P_l}{\partial r} \right) r_0 \right] . \quad (2.25)$$

By minimizing the total energy $E = E_{el} + E_{mag-el}$, where the elastic energy is given by the quadratic dependence on strain,

$$E_{el} = \frac{1}{2}C_{11} (e_{xx}^2 + e_{yy}^2 + e_{zz}^2) + \frac{1}{2}C_{44} (e_{xy}^2 + e_{yz}^2 + e_{zx}^2) + C_{12} (e_{xx}e_{yy} + e_{yy}e_{zz} + e_{zz}e_{xx}) , \quad (2.26)$$

the elongation in the direction $(\beta_1, \beta_2, \beta_3)$ can then be written,

$$\frac{\delta l}{l} = \frac{3}{2}\lambda_{100} \left(\alpha_1^2\beta_1^2 + \alpha_1^2\beta_2^2 + \alpha_1^2\beta_3^2 - \frac{1}{3} \right) + 3\lambda_{111} (\alpha_1\alpha_2\beta_1\beta_2 + \alpha_1\alpha_2\beta_1\beta_3 + \alpha_1\alpha_2\beta_2\beta_3) , \quad (2.27)$$

where C_{ij} are the stiffness moduli (in Voigt notation) and $\lambda_{100}, \lambda_{111}$ are the magnetostriction coefficients whose form again depends on the crystal symmetry:

$$\begin{aligned}\lambda_{100} &= \frac{16}{9} \frac{N}{C_{12} - C_{11}} P_l \\ \lambda_{111} &= -\frac{8}{27} \frac{N}{C_{44}} \left[1 + \left(\frac{\partial P_l}{\partial r} \right) r_0 \right]\end{aligned}\quad \text{(BCC)} \quad (2.28)$$

and

$$\begin{aligned}\lambda_{100} &= \frac{1}{3} \frac{N}{C_{12} - C_{11}} \left[6P_l + \left(\frac{\partial P_l}{\partial r} \right) r_0 \right] \\ \lambda_{111} &= -\frac{1}{3} \frac{N}{C_{44}} \left[2P_l + \left(\frac{\partial P_l}{\partial r} \right) r_0 \right]\end{aligned}\quad \text{(FCC)} \quad (2.30)$$

Thus, the magnetostriction for an individual domain in a crystal with cubic symmetry is scaled by the elastic constants and dependent on the functional form of the dipole-dipole interaction P_l , to first order[25, 27].

Hydrogen (in the concentrations frequently encountered in welds) has been observed to impact the elastic constants only to a limited extent, generally in the form of softening of the order of a few percent[3, 41, 42]. *Ab initio* calculations have indicated that overall effect is the result of a softening strain effect due to hydrogen interstitials and a strengthening electronic component[43]. It is unclear from this information alone whether hydrogen should increase or decrease either or both independent magnetostriction coefficients, as the introduction of both a hydrostatic strain and local disruption to spin-pair potentials by the interstitial will have dramatic effects in both cases. These complicated interactions are likely a strong contributing factor in the difficulty encountered interpreting magnetoacoustic emission data in Section 4.7.

2.2.5 Magnetoacoustic Emission

When the rotation (or nucleation/growth) of a particular domain relative to another is *not* 180°, there is a concomitant mechanical strain if the magnetostriction of the material is

nonzero, that is if there is associated with magnetization a microscopic strain in the lattice, $\frac{dl}{l} = \lambda(\mathbf{H}) \neq 0$. The magnetostriction is frequently strongly dependent on the strength of the magnetic field, and in general, the relationship is not a convenient or simple function[27]. Nevertheless, the exact behavior of the magnetostriction is not critical to the purposes of this study which is firmly set in practical application of the phenomenon. It is sufficient merely that acoustic energy be generated by the magnetization process, as it affords inquiry of the bulk material which would otherwise be limited to the surface by electronic screening of electromagnetic energy.

Macroscopic observation of magnetostriction in polycrystals reduces the magnetostriction coefficients of Equations (2.28) and (2.30) to a single averaged value,

$$\bar{\lambda} = \frac{1}{5} (2\lambda_{100} + 3\lambda_{111}) , \quad (2.31)$$

which produces a volumetric strain at sufficiently large length scales. Such dilatation is the form addressed by Skal's'skyi et al. [44], who applied the theory of Eshelby [45] for elastic inclusions to the phenomenology of MAE. Briefly, the process involves the removal of an ellipsoidal inclusion from the large (isotropic) material, application of a stress-free strain to the inclusion, and computation of the strain field produced by its replacement back into the parent matrix. By consideration of the bulk and surface stresses, the displacement at a distance r in the angular direction θ due to the volumetric change ΔV of the inclusion is

$$\frac{C_{11} \cos^2 \theta}{4\pi \rho c_l^3 r} \epsilon_{zz} \frac{d}{dt} \left[\Delta V \left(t - \frac{r}{c_l} \right) \right] , \quad (2.32)$$

where c_l is the longitudinal velocity of sound in the material, and ϵ_{zz} is related to the degree of magnetization[44],

$$\epsilon_{zz} \sim \bar{\lambda} \frac{M}{M_s} . \quad (2.33)$$

In steel, the number of magnetoacoustic events per magnetizing cycle has been reported in literature to increase with hydrogenation[15], but the limited data available makes stronger correlation difficult. Since magnetoacoustic emission is a coupled phenomenon depending on both magnetic and mechanical properties, any observed effects of hydrogen may be intensified, though perhaps at the cost of more complicated analysis. If the manner of domain motion changes from primarily translation to rotation as can occur under externally-applied elastic strain, for example, departures from linear relations such as those suggested by Equation (2.33) become the norm[46].

2.2.6 Magnetic Hysteresis and Nonlinearity

A principal consequence of the aforementioned phenomena is pronounced nonlinearity in the magnetization behavior of ferromagnetic materials. Over the course of a magnetization cycle, the microscopic processes such as domain rotation, DW motion, and technical saturation all contribute varying amounts to the observed magnetization in a field- and time-dependent way. For a sinusoidal applied field observed on a macroscopic scale, the overall effect is to distort the magnetizing frequency into multiple harmonics, which can then be used as a coarse metric for this nonlinear behavior.

A number of models have been proposed to unify the various phenomena into a single theory of ferromagnetic hysteresis, each with advantages, weaknesses, and applicable classes of problems[47]. One model that is both relevant to the current discussion and captures many of the features observed in experiment was proposed by Jiles and Atherton[48]. This model accounts for both domain wall bowing and displacement (Figure 2.7B–C) via reversible and irreversible magnetization processes M_{rev} and M_{irr} , respectively. Friction encountered in the displacement of the domain walls is addressed by the introduction of pinning sites which are assumed to be homogeneously distributed with density k through an isotropic material. Interdomain interactions are coupled by a mean-field parameter α . Ideal behavior (i.e. anhysteretic) is well-described for iron by the Langevin function,

$$M_{an}(H_{eff}) = M_s \left[\coth \left(\frac{H_{eff}}{a} \right) - \left(\frac{a}{H_{eff}} \right) \right], \quad (2.34)$$

where $H_{eff} = H - \alpha M$ is the effective field incorporating the mean-field parameter and a is a thermal shape parameter with units of magnetic field.

On its own, Equation (2.34) is sufficient to introduce nonlinear behavior into the system such that a sinusoidal applied field \mathbf{H} will give rise to a magnetization with odd harmonic content. Hysteresis further affects the $M - H$ behavior and introduces additional energy loss. Inclusion of hysteretic terms in the form of reversible (bowing) and irreversible (displacement) magnetization processes is accomplished by the solution of two coupled differential equations[47],

$$\begin{aligned} \frac{dM_{irr}}{dH} &= \frac{M_{an}(H) - M_{irr}(H)}{\delta k - \alpha(M_{an}(H) - M_{irr}(H))} \\ \frac{dM_{rev}}{dH} &= c \left(\frac{dM_{an}}{dH} - \frac{dM_{irr}}{dH} \right) \end{aligned} \quad (2.35)$$

which sum to the susceptibility,

$$\frac{dM}{dH} = \frac{dM_{irr}}{dH} + \frac{dM_{rev}}{dH}, \quad (2.36)$$

where c is a free parameter which determines reversible effects and δ is $+1$ or -1 for an increasing or decreasing field, respectively.

Equations (2.34) and (2.35) are solved numerically in Figure 2.8 for nominal free parameter values of $a = 2 \text{ kA m}^{-1}$, $\alpha = 0.5 \times 10^{-3}$, $k = 1 \text{ kA m}^{-1}$, $c = 0.1$, and the saturation magnetization $M_s = 1.7 \text{ MA m}^{-1}$. Variation of these parameters result in the separate magnetization curves on the left and their effects on a sinusoidal applied field are shown at right for the time and frequency domains. The first four odd harmonics above the fundamental frequency ($f_d = 5 \text{ Hz}$) are shown in the bottom right of Figure 2.8, along with a relative

measure of nonlinearity: the ratio of the third harmonic to the fundamental (in the analysis of Chapter 4, the ratio is computed for all non-fundamental harmonic content).

Changes in the parameters a and α affect the harmonic distortion the most for the values selected, though the two are not completely independent in terms of physically measurable quantities, being related to the initial (anhysteretic) susceptibility[49],

$$a = \frac{M_s}{3} \left(\frac{1}{\chi'_{an}} + \alpha \right)$$

The parameter k corresponds to the coercivity, and indeed $k = H_c$ for magnetically soft materials. Doubling of this parameter does not have a notable impact on the harmonic content directly, but the larger area enclosed by the curve between cycles implies a greater loss in energy to hysteresis and a decrease in amplitude overall. Hydrogen has been observed to affect all of these parameters (or, rather, their underlying quantities): notably the coercive force[33, 50] and saturation magnetization[3].

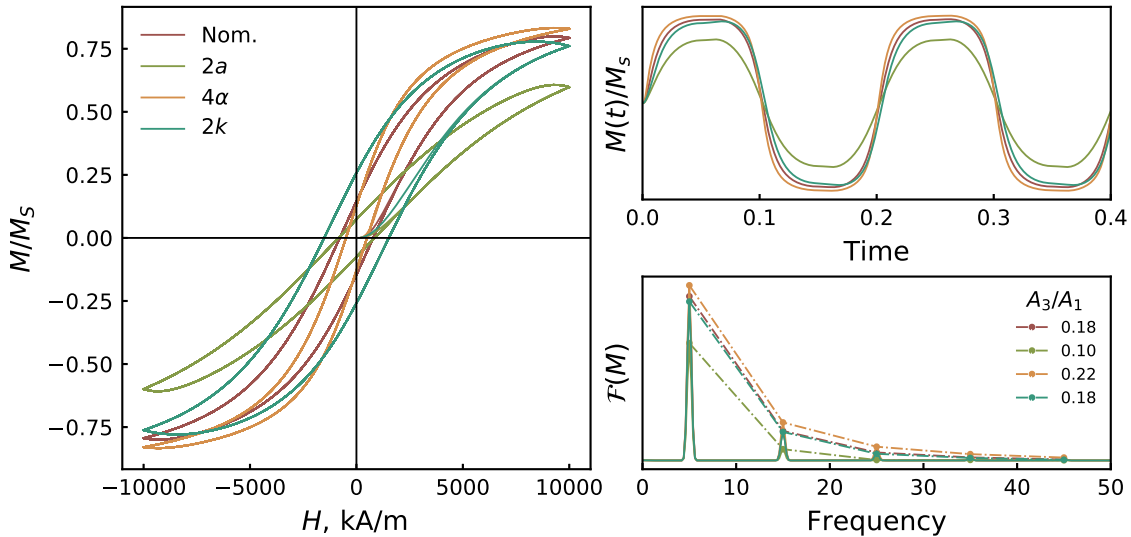


Figure 2.8: Impact of changes in parameters for the Jiles-Atherton model[48] of ferromagnetic hysteresis. Equations (2.34) and (2.35) are solved with nominal values of $a = 2 \text{ kA m}^{-1}$, $\alpha = 0.5 \times 10^{-3}$, $k = 1 \text{ kA m}^{-1}$, $c = 0.1$, and with individual parameter changes as described in the hysteresis curves (left). Sinusoidal magnetization (magnetizing frequency $f_d = 5 \text{ Hz}$) yields the distorted time signal and frequency spectrum (right).

2.3 Summary

A century of research into the manifold effects of hydrogen has accumulated an enormous body of useful albeit occasionally conflicting information regarding the various properties of iron and steel. For the magnetic quantities relevant to this study, hydrogen has been observed to reduce the individual magnetic moment (and therefore the macroscopic spontaneous magnetization), while increasing the coercive field required for domain wall motion. Some hydrogen effects have been noted on the elastic constants and electrical conductivity, which are both properties that affect the practical observation of the magnetoacoustic and Barkhausen effect, but the variation in these quantities is likely minimal for the concentrations considered here. However, the enigmatic nature of hydrogen mobility as it relates to various traps at room temperature presents a perpetually perplexing predicament for reliably characterizing the properties in question due to inhomogeneous distribution of interstitial atoms.

CHAPTER 3

EXPERIMENT

This chapter serves to provide details of the experiments and subsequent data reduction and analysis performed in this study. Presented first are the specific alloys and heat treatments used to vary the microstructure between the steel samples. Discussion of hydrogen introduction by cathodic charging and determination of diffusible hydrogen by a modified glycerine method follows. Finally, the details of magnetic property measurements including Barkhausen noise, magnetoacoustic emission, and several related flux-dependent quantities are provided along with an explanation of the various signal processing methods used. Interspersed in the account are examples and analyses of the assorted features observed during magnetization.

3.1 Samples

Two high strength low alloy AISI steel alloys were selected for testing since their specification is based on composition instead of deliverable properties as would be found in an ASTM- or API-established material. For the experiments performed, AISI 4340 (Cr-Mo-Ni) and 4140 (Cr-Mo) steel were chosen for their hardenability and susceptibility to hydrogen embrittlement; nominal compositions are given in Table 3.1. Variation in microstructure, accomplished by tempering oil-quenched samples at selected temperatures, was explored in consideration of (1) the role carbide precipitation and growth plays in hydrogen trapping and magnetic domain wall pinning, and (2) the effect of changes in crystal structure on hydrogen solubility and/or diffusivity.

In particular, finely dispersed carbides present at lower T_{temp} inhibit magnetic domain wall motion, thereby increasing local coercivity, while simultaneously acting as relatively strong traps for hydrogen (with binding energy some 4–5 times stronger than dislocations, for example[2]). Lath martensite, consisting of high densities of dislocations and defects,

further acts to impede hydrogen diffusion while also affecting the distribution, shape, and mobility of magnetic domains[51]. Furthermore, nickel atoms (present in AISI 4340 steel in amounts between 1.7 and 2%) have fewer unpaired electrons than those of iron, observed as a decrease in the spontaneous magnetic moment from $2.2\mu_B$ to $0.61\mu_B$ (as illustrated in the Slater-Pauling curve[28]). Impact of the presence of nickel (itself being ferromagnetic) in the series of tests for AISI 4340 steel was explored as a possible confounding factor for the magnetization tests, but the relatively low differences in concentration between alloys did not appear to dramatically alter the behaviors observed.

Samples of nominal dimensions $9 \times 9 \times 20$ mm were machined from the center of AISI 4340 steel round stock (25 HRC as received) and AISI 4140 steel bar stock (90 HRB) obtained from a commercial source, then normalized for 1 hour at 871°C . Heat treatments (quenching and tempering) were selected based on the sample geometry and handbook values for tempering temperature and time to provide a range of strengths[52].

Table 3.1: Specified nominal chemical compositions for steel samples used in the MAE/MBN tests.

(In wt. pct.; Iron constitutes remainder.)

AISI	C %	Cr %	Ni %	Mn %	Mo %	P wppm	Si %	S wppm
4140	0.38–0.43	0.80–1.10	–	0.75–1.0	0.15–0.25	≤ 350	0.15–0.30	≤ 400
4340	0.37–0.43	0.70–0.90	1.65–2.00	0.60–0.80	0.20–0.30	≤ 350	0.15–0.30	≤ 400

3.1.1 AISI 4340 Steel

For an initial two-level/two-factor experiment, four samples were austenitized then quenched into room temperature (25°C) oil. The furnace was allowed to cool to the appropriate temperature, and the samples were placed back in to temper for one hour according to the scheme provided in Table 3.2. After tempering, the samples were ground with 320-grit silicon carbide emery paper on plate glass to remove the oxide layer, and re-measured with a micrometer. Electrolytic charging was performed in a 0.5 M sulfuric acid solution with

1 g l⁻¹ thiourea at 60 °C for the current densities and times in Table 3.3.

Table 3.2: Sample matrix for AISI 4340 steel. All samples oil quenched from a temperature of 840 °C

Sample 4340- <i>x</i>	Tempering		
	Time h	Temp. °C	Est. σ_y [53, 54] MPa
1	As Q.		2015
2	1	230	1620
3	1	230	1620
4	1	450	1340
5	1	450	1340

Table 3.3: Experimental matrix for AISI 4340 steel.

Test Nº	Sample 4340- <i>x</i>	Charging	
		Time min	Cur. Dens. mA cm ⁻²
10	5	30	1
11	2	15	1
12	4	15	1
13	3	30	1
14	2	30	10
15	5	30	1
16	1	30	1
17	1	60	10
18	4	60	10
19	2	60	10
20	4	60	10

3.1.2 AISI 4140 Steel

In the second series of tests, after noting considerably higher hydrogen absorption for the latter AISI 4340 steel tests with more aggressive charging conditions, it was decided to restrict the current densities for AISI 4140 steel to 5–10 mA cm⁻². Heat treatment parameters are given for the AISI 4140 steel samples in Table 3.5, and Table 3.4 gives charging conditions for each test.

Table 3.4: Sample matrix for AISI 4140 steel. All samples oil quenched from a temperature of 840 °C

Sample 4140- x	Tempering		
	Time h	Temp. °C	Est. σ_y [55] MPa
2	1	538	1050
3	1	538	1050
4	1	538	1050
5	1	427	1340
6	1	427	1340
7	1	427	1340
8	2	210	1740
9	2	210	1740
10	2	210	1740

Table 3.5: Experimental matrix for AISI 4140 steel. All samples oil quenched from a temperature of 840 °C

Test №	Sample 4140- x	Charging	
		Time min	Cur. Dens. mA cm ⁻²
21	5	60	10
22	6	120	5
23	7	30	10
24	2	60	10
25	3	120	5
26	4	30	10
21	5	60	10
22	6	120	5
23	7	30	10
27	8	60	10
28	9	120	5
29	10	30	10

3.2 Cathodic Charging

Introduction of hydrogen into the samples was accomplished by electrochemical cathodic charging, wherein a constant current source supplied electrons for reduction of aqueous hydrogen in a sulfuric acid solution according to[16]



Absorption of atomic hydrogen into iron competes with the recombination of adsorbed atoms as gaseous hydrogen, which would otherwise bubble off and result in a failure to charge the metallic samples. Therefore when cathodically charging, so-called poisons are frequently introduced to inhibit gaseous evolution of hydrogen, and are commonly composed of arsenic-containing compounds[56]. Given the health and environmental concerns associated with arsenic, and the increased likelihood of mechanical damage during electrolysis, thiourea was selected as a poison. Investigations by Shim and Byrne[57] indicate that even at current densities up to several tens of mA cm^{-2} no cracking is observed when the electrolyte was poisoned with 1 g l^{-1} thiourea and that mechanical properties fully recovered after aging at room temperature following charging, suggesting that the process was substantially reversible.

A stock solution of $0.5 \text{ mol l}^{-1} + 1.0$ or 2.0 g l^{-1} thiourea (ACS) was made gravimetrically using distilled water and stored in a polycarbonate container. For a single charging test (shown in Table 3.1), 300 ml of stock solution was placed in a 1000 ml beaker with a sparging stone approximately 30 mm in diameter. Gaseous nitrogen was then discharged through the stone for no less than 30 minutes prior to electrolytic charging to remove dissolved oxygen which would otherwise be reduced in the charging process (reducing current efficiency). A sample was placed in an aluminium wire basket to which the cathode lead (terminated by an alligator clip) of a 1 m long coaxial (RG-58) cable was attached; a platinized dimensionally-

stable (titanium) counter-electrode was connected to the anode lead. Constant current, provided by a Keithley 225 unit, was applied for the time specified in Tables 3.3 or 3.5.

When charging was completed, the current source was turned off and simultaneously a stopwatch started. The sample was removed and rinsed in distilled water, dried, and placed in the apparatus, described in §3.4. The charging solution was returned to the stock container and the basket, counter-electrode, and sparging stone were rinsed with distilled water. After nine tests⁶, the pH increased from 0.45 to 0.72; for the tests reported here, a new electrolyte was prepared after charging with the solution three times.

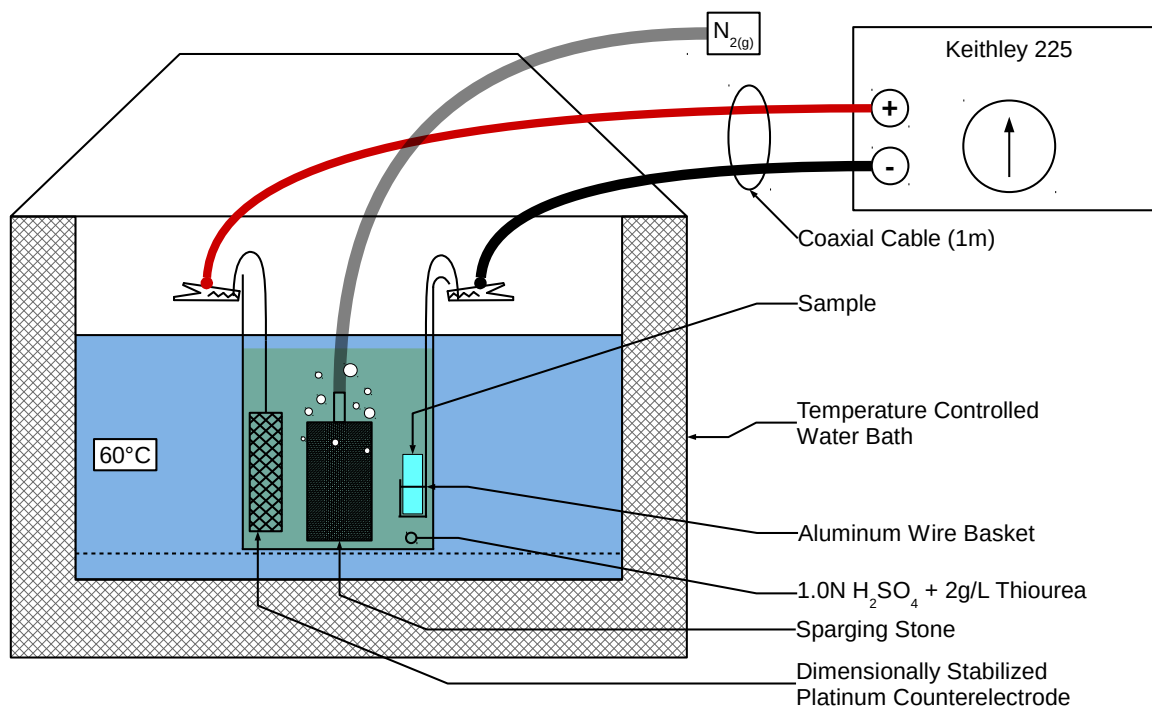


Figure 3.1: Arrangement for cathodic charging of steel samples. Thiourea concentration was 1 g l^{-1} for AISI-4340 steel tests and 2 g l^{-1} for 4140 steel tests.

⁶These initial tests were preliminary in nature and encumbered by sub-optimal experimental methods. They are not reported here.

3.3 Hydrogen Determination

A modified glycerine procedure was used to quantify the diffusible hydrogen content in charged samples. In this test, derived from the Canadian Standards Association W48.7[58], a sample is charged as described in Section 3.2 and quickly rinsed in distilled water and dried. The sample was placed under a 3D-printed funnel (ABS), which was secured in a wire basket as shown in Figure 3.2. The ensemble was lowered into a 1000 ml graduated cylinder filled with a column of glycerine 150mm deep pre-heated to 45 °C. An inverted 10 ml buret (0.05 ml readability) formed a seal with the funnel, and a vacuum draws the glycerine slightly passed the stopcock which was then closed. All of these steps were completed within one minute of the discontinuation of electric current, per the requirement of the standard[58].

The foregoing implements were then placed back in a water bath at 45 °C and the sample was allowed to offgas for 48 hours, after which time the volume of gas was read from the inverted buret and recorded. In literature, diffusible hydrogen content is frequently reported as ml/100g deposited metal. Since no actual metal is deposited in this experiment (as would be with a weld bead), the volume of gas is reported here as the volume of hydrogen evolved over the 48-hour period, divided by the sample weight and extended to the full 100 g (typical sample masses are on the order of 12 g).

Frequently, the meniscus of the hydrogen gas and glycerine was not between graduations on the burette (i.e. the interface was between the stopcock and smallest marked value). To alleviate this issue and to increase the relative precision of the measurement, the volume of gas was measured using a caliper and a reference point on the burette. However, as the inside diameter of the burette is not constant and necks down closer to the stopcock, calibration of the burette volume was required. Thus, a curve was generated by gravimetric determination of water volume as a function of the distance from a selected datum (in this case, the 10 ml-mark of the burette). A fitting spline was computed by least squares to yield a gas volume function as shown in Figure 3.3. Measurements of gas volume were then made using digital calipers and converted using this spline function.

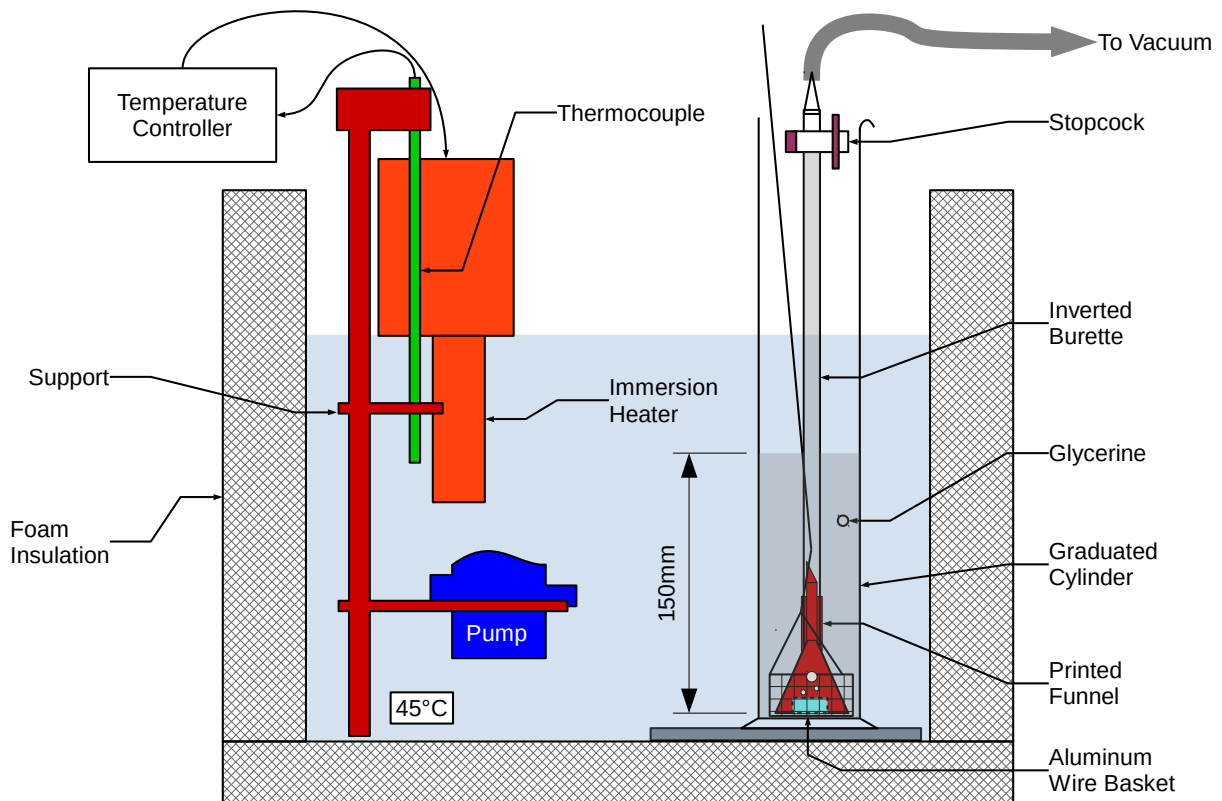


Figure 3.2: Apparatus for diffusible hydrogen concentration determination. Hydrogen-charged samples are placed in a glycerine bath at 45°C for 48 hours and evolved $H_{2(g)}$ collected. The procedure is consistent with the requirements of the Canadian welding standard CSA W48.7 (1977).

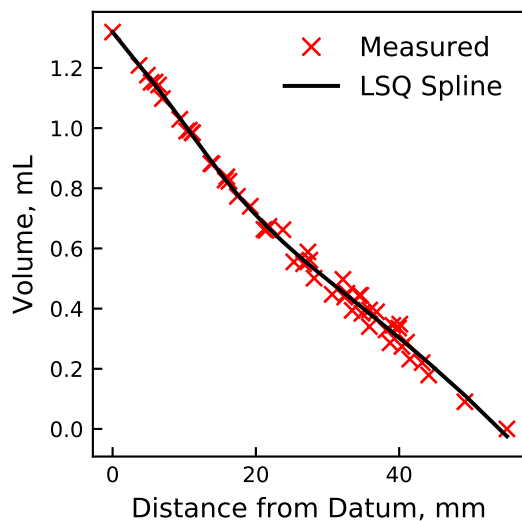


Figure 3.3: Eudiometer tube calibration curve for evolved hydrogen determination. There was generally insufficient hydrogen gas evolved to register within the graduations of the 10 mL burette. As such, a calibration curve with a least-squares spline as a function of distance from the 10 ml mark was used to estimate total hydrogen gas.

3.4 Testing of Magnetic Properties

In the language of these experiments, a sample charged with hydrogen then mounted in the apparatus constitutes a single *test*. At various times, multiple *measurements* (*e.g.* MAE, MBN) are made each consisting of three *replicates* of rapidly-acquired consecutive waveforms over several magnetizing cycles. The last of these are termed “replicates” because they are an indication of the variability of a given parameter made for a single measurement with regard to spurious emissions that may occur during a test, and they form the basis for the error bars (as standard deviations, $\hat{\sigma}$) in the figures below. Replicates do not reflect other sources of error such as transducer mounting variations or temperature fluctuation, so they should not be construed as being representative of the total error in a test as a whole.

3.4.1 Apparatus Design

After charging the sample with hydrogen, it is placed in a channel cut into a laminated iron transformer (Signal Transformer⁷ LP-24-1000) to accommodate the specimen as shown in Figure 3.4 and schematically in Figure 3.5 (side view; a front view is shown in 3.12). At either end is a piezoelectric transducer (PT) with broadband frequency response of 50–2000 kHz (Digital Wave Corp. B1025); above is placed an MBN sensor composed of a 3D printed bobbin wrapped with 2500 turns of 0.086 mm-diameter (#40 AWG) magnet wire. Inside the bobbin of the MBN pickup coil is a $\varnothing 1 \times 10$ mm, ferrite core (material: Fair-Rite 78).

To provide consistent applied force, the two piezoelectric transducers are held in place by four-bar linkages under tension from springs on either side. Dielectric grease is applied as a couplant between the PT and sample. One or two layers of polyimide tape are placed between the sample and core to provide a tight fit and help secure the sample during magnetization. The changing flux in the semi-toroidal magnetic circuit is detected by twenty turns of 0.160 mm magnet wire and recorded. The ensemble is placed in a $150 \times 150 \times 150$ mm Faraday cage which is connected to the USB-oscilloscope (PicoScope 5443B) chassis/ground reference; electrical connections are made through 10 mm grommets in the cage.

A $400 \text{ mV}_{\text{pp}}$, 25 or 24 Hz sine wave is produced by an arbitrary waveform generator onboard the oscilloscope and amplified by one channel (in a bridged load configuration) of a 160 W class D amplifier (based on the ST Micro TDA7498E) with gain of 35.6 dBV. The output from the power amplifier is applied to the secondary coils of the transformer (connected in series), with a ferrite bead to reduce electromagnetic interference. For each measurement, power is applied for a few seconds allowing the oscilloscope to capture three complete waveforms of MAE (channels A, B), MBN (C), and induced $\text{EMF} \propto \dot{\Phi}$ (D) in rapid succession, which are stored as a single file on disk to be analyzed later. When measurements

⁷This description does not reflect the type of transformer used—the name of the manufacturer is Signal Transformer and they make power transformers...

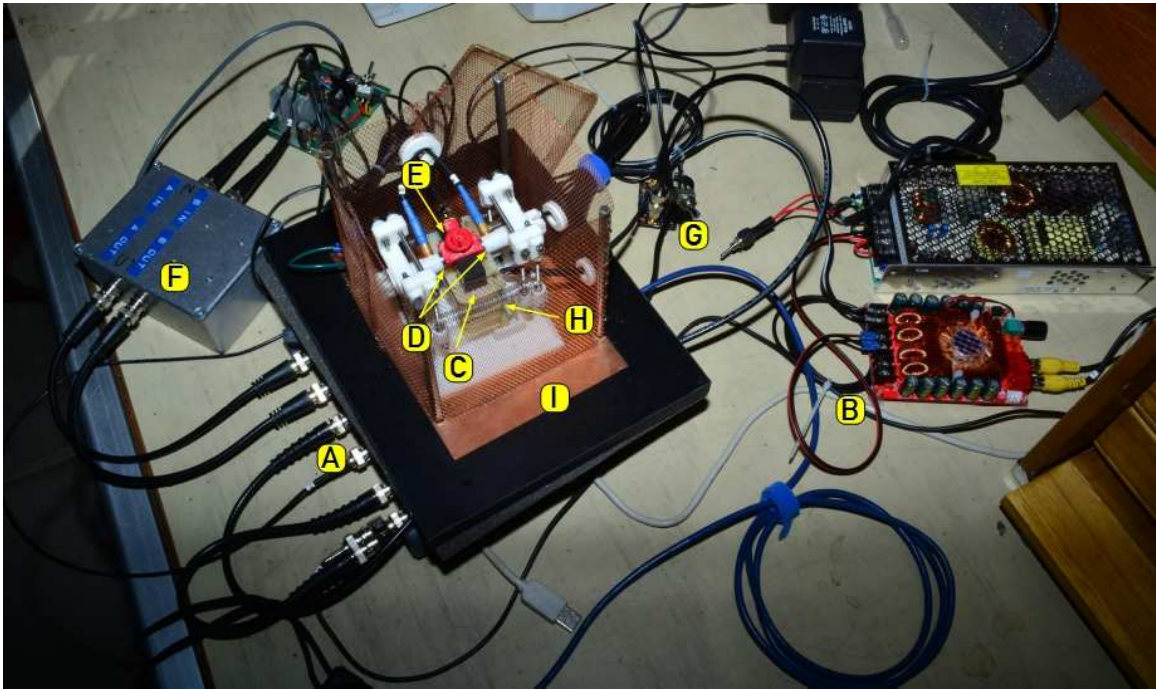


Figure 3.4: Photograph of magnetic testing fixture with sample. A PC-based oscilloscope with integrated waveform generator (A) produces a sinusoidal voltage which is amplified by a class D audio amplifier (B), the output of which drives a cut transformer (C) with a sample placed in the gap. A coil of 20 turns replaces one of the primary coils on the transformer, its voltage proportional to the changing magnetic flux (H). Piezoelectric transducers (D) are held against the ends of a rectangular sample (occluded in this figure) by linkages, and a 1600 turn Barkhausen noise pickup coil is located above (E). Signals from the acoustic transducers and Barkhausen coil are conditioned by a charge amplifier (F) and active filter (G), respectively before being digitized by the oscilloscope (A). A Faraday cage surrounds the magnetizing circuit and transducers (I).

are not being made, power to the apparatus is turned off to prevent heating and premature failure of the coils.

3.4.2 Analog Signal Processing

One technical hurdle associated with implementing piezoelectric transducer elements is the significant parasitic capacitance encountered both in the elements themselves (as they are essentially parallel plates separated by a dielectric) and the cabling which connects them to later stages in the signal processing chain. In this experimental setup, the 9 mm diameter elements constitute about 300 pF, and the 1 m of RG-174 coaxial cable about 100 pF. The

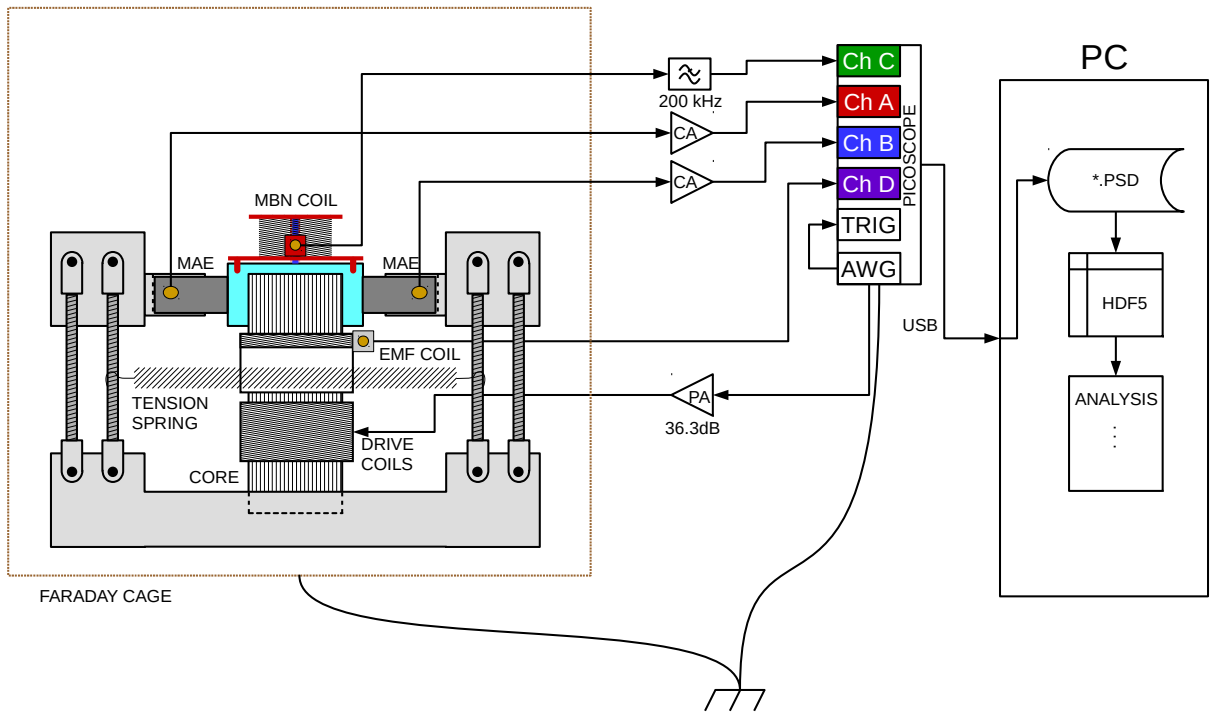


Figure 3.5: Physical arrangement and signal flow during Magnetoacoustic and Barkhausen noise testing (profile). Hydrogen-charged samples are placed in a sinusoidal magnetic field through perpendicular to their long axis (out of paper). Magnetoacoustic emission and Barkhausen noise are sensed in directions perpendicular to the developed field, then conditioned and digitized by a USB oscilloscope. Stored waveform data files consisting of Barkhausen noise, magnetic flux, and 2 channels of magnetoacoustic emission are converted to a hierarchical data format (HDF5) and subsequently analyzed for various features.

miniscule charges produced by the PT from MAE necessitates the usage of a charge-mode amplifier (CA), so one was constructed for this purpose.

Practical design of charge-mode amplifiers is somewhat finicky, as one might expect in analog circuits of this type, so only the salient features will be related here. The circuit, for which a schematic is shown in Figure 3.6, consists of an op-amp in an inverting configuration with a very small value high-Q capacitor, C_F , in the feedback path—essentially a charge integrating circuit. The circuit gain and frequency response are given by[59]

$$G = -\frac{1}{C_F}$$

$$f_L = \frac{1}{2\pi R_F C_F} \qquad f_H = \frac{1}{2\pi R_{IN}(C_T + C_C)},$$

where f_L and f_H are -3 dB cutoff frequencies (Hz), and C_T and C_C are the aforementioned transducer and cable capacitances, respectively. The resistor, R_F , is there to bleed off the feedback capacitor which would otherwise saturate from op-amp bias currents (FET-input op amps are good choices here as these currents are then of the order of a few pA. Values for R_F tend to be quite large, however, so the value for R_{IN} (which would otherwise be present for primarily ESD protection) needs to be higher to reduce the closed-loop gain (in the ordinary sense of an inverting amplifier) to values that do not cause excessive distortion (albeit at the cost of higher thermal noise). The balance in tradeoffs ultimately leads to substantial trial-and-error, but values shown in Figure 3.6 and Table 3.6 give reasonably satisfactory results.

Table 3.6: Component values and parameter differences between tests for AISI 4140 and 4340 steels.

Series	f_d	f_{Sa}	U_1	R_I	C_F	R_F
–	Hz	MSa/s	–	k Ω	pF	M Ω
4340	25	5	OPA656	4.3	0.3	0.47
4140	24	2	LT1880	0	0.3	2

Charge Amplifier (2 Channels)

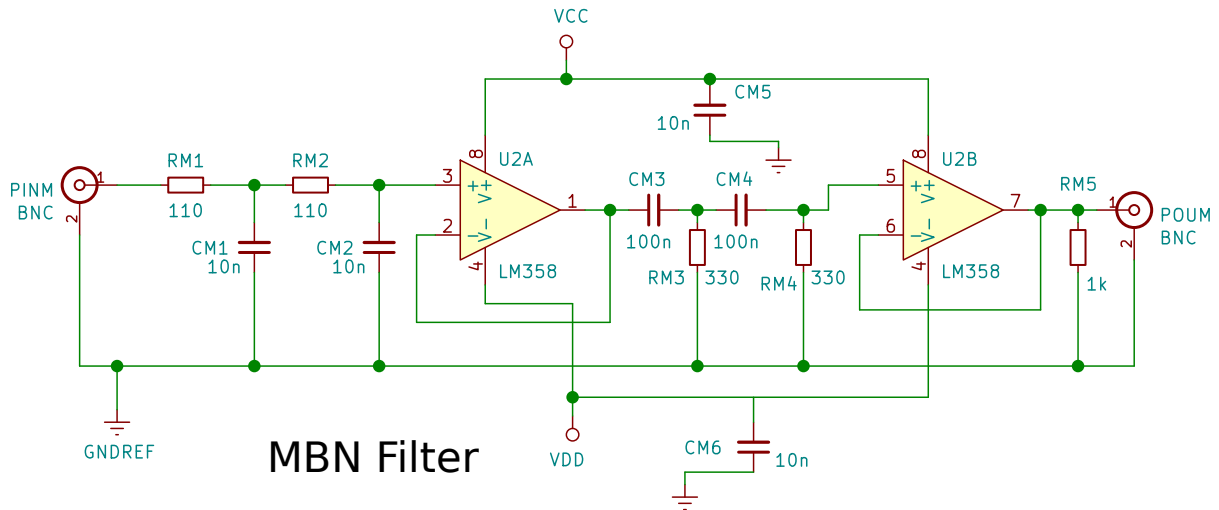
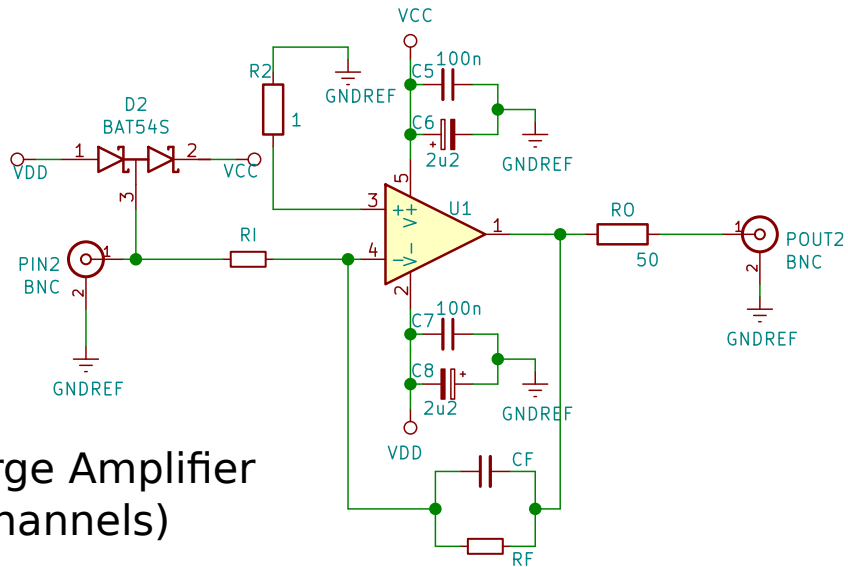


Figure 3.6: Electronic schematic for MAE/MBN transducer front ends. Component values varied between AISI 4340 and 4140 steel tests; they are given in the Table 3.6.

The sensitivity of the MBN sensor coupled with its close proximity to the magnetizing coils and their connections results in significant spurious signal at the oscilloscope. In particular, the switching frequency from the class D amplifier causes (predictable) interference at 310 kHz and its harmonics, and fluorescent lighting, external power supplies, etc. induce noise elsewhere in the spectrum. For the former, a second order low pass filter (LPF) was implemented with a cutoff frequency of $f_c = 200$ kHz. For the latter, the small Faraday cage surrounding the apparatus was sufficient to attenuate much of the interference. Finally, a second order RC filter alleviated much of the low frequency (f_d) interference from flux leakage through the MBN pickup coil. The two RC filter stages and the oscilloscope were isolated by unity-gain buffers.

3.4.3 Digitization and Storage

Signals from the two MAE sensors, the MBN pickup coil, and the core flux coil were, following their respective filters and amplifiers, delivered to the USB-oscilloscope, where they were digitized at 5 or 2 MSa/s with 14 bit resolution. Three consecutive waveforms were recorded for each measurement to act as replicates for that point in time for a given test, and they were stored on disk in a file format proprietary to PicoTech oscilloscopes (*.psdata). At the conclusion of a test, all of the files were exported to a Matlab-compatible (*.mat) format as 32 bit floating point numbers. Since the resolution of the digitizer is less than half that bit depth (14 bit), significant storage space (approximately 2 GB per test) would otherwise be wasted. Thus, the data were converted to a single HDF5 file as 16 bit short integers while preserving the range of the individual waveform (e.g. ± 10 , ± 20 , or ± 500 mV/div) with a double precision scalar.

3.4.4 Digital Filtering

Even with the analog filtering provided by the low pass filter on the MBN channel and the rolloff of the charge amplifier, substantial unwanted signal remains, particularly at low (sub-kHz) frequency. For the MAE sensors, some harmonic distortion still occurs from the

op amp, but interference from the driving coils and mechanical instability in the sample and fixture⁸ contribute the most significantly. In the case of the MBN pickup coil, magnetic flux leakage around the sample and magnetic core induce very large voltages at the driving frequency f_D .

A finite impulse response (FIR) filter thus formed the final stage of the signal processing chain. A 1023-tap bandpass filter with critical frequencies at 20 and 100 is constructed by the window method (Hamming window) using the implementation provided in NumPy/SciPy. The frequency response of the filter is provided in Figure 3.7, and a typical set of filtered waveforms (constituting a single replicate of a single measurement) are reproduced in Figure 3.8.

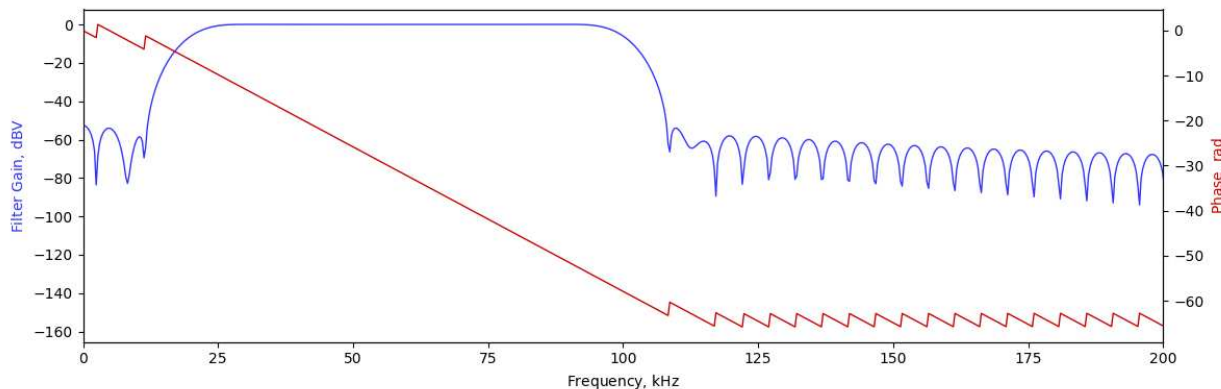


Figure 3.7: Filter response for digital filter used for Barkhausen and magnetoacoustic effect measurements. Critical frequencies for this 1023-tap finite impulse response are at 10 and 100 kHz.

Extraction of relevant information from the stored waveforms is accomplished by quantifying various aspects of the magnetization cycle. In the analysis that follows, several parameters of interest are evaluated for the four sensors (MBN, PT A , PT B, and core flux): (1) Total electrical energy (taken as integrated squared voltage) detected by the sensor MBN or MAE, (2) MAE/MBN event counts (estimated in a quasi-statistical sense), and (3) amplitude, phase, and harmonic distortion of the core flux. For Points (1) and (2), it

⁸Strong, oscillating magnetic forces can cause poorly secured samples to vibrate or strike the core.

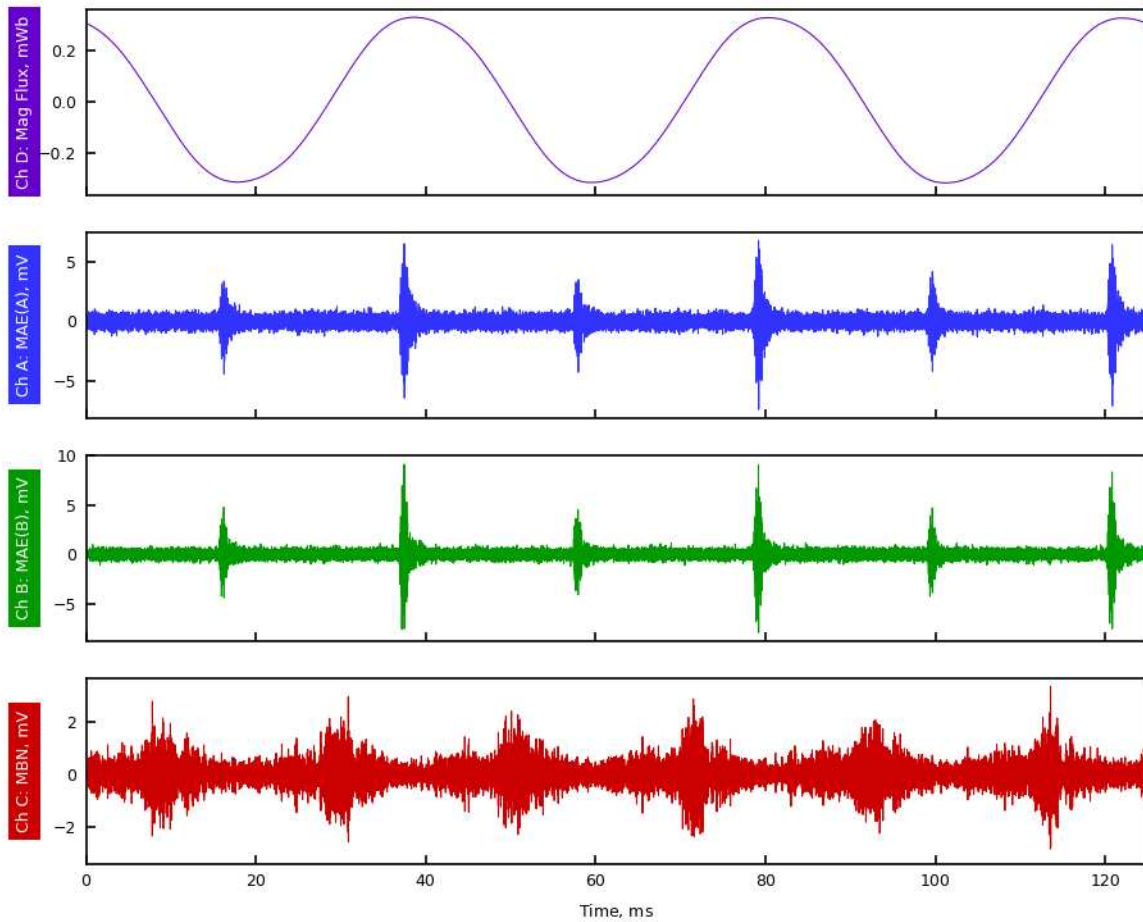


Figure 3.8: Typical filtered waveforms for a single measurement. (Test 21: AISI 4140 steel tempered at 427 °C, 121 s after charging for 60 minutes at 10 mA cm⁻².)

is necessary to compute the magnetic flux from the induced voltage in the pickup coil; the evaluation of this quantity will be considered first.

3.5 Magnetic Flux Estimation

From the EMF generated by a flux-sensing coil around one of the legs of the transformer core, the flux in the magnetic circuit through the core and sample can be estimated by numerically integrating over the waveform,

$$\Phi(t) = - \int_0^t \frac{\mathcal{EMF}(\tau)}{N} d\tau \quad (\text{Wb}), \quad (3.3)$$

where N is the number of turns (20-turns of 0.160 mm/# 34 AWG in this case). Further scaling by dividing by the effective area would give the magnetic flux density, B (T), but the area is difficult to quantify exactly given the discontinuities in geometry and magnetic flux leakage. At the flux sense coil itself, the maximum observed flux of ≈ 0.32 mWb would correspond to ≈ 1.1 T. The top plot of Figure 3.8 shows the raw signal from the flux pickup coil; the driving signal is a 25 Hz sine wave, which is at the lower limit of the capabilities of the class D audio amplifier, so significant harmonic distortion is observed. Figure 3.9 shows the estimated magnetic flux, appearing again sinusoidal since the higher harmonics are suppressed by integration.

3.6 MAE/MBN Quantification

Extraction of useful noise parameters is accomplished by heuristic means, given the stochastic nature of the underlying processes. Specifically, because MAE and MBN emissions consist of a largely random element, data reduction algorithms must exploit some statistical features to a certain extent[27]. In the following discussion, the two parameters referred to in the start of this section (energy and the number of events) are explored as rudimentary indications of the influence of hydrogen on the magnetic properties of steel. Strictly speaking, these parameters are not completely independent, and thus exhibit much of the

same behavior between them. Even so, it is worth considering each as a separate conceptual approach to observing the effects of hydrogen concentration.

3.6.1 Window Convolution

To approximate the root mean squared (RMS) voltage of a digitized signal, it is convenient to convolve the waveform, squared element-wise, with an appropriate window. In the case of a rectangular or boxcar window, this operation amounts to a moving average of the sum of the squares, and its effect is shown in the bottom three plots of Figure 3.9, where the length of the window is 500 Sa ($250 \mu\text{s}$) in duration.

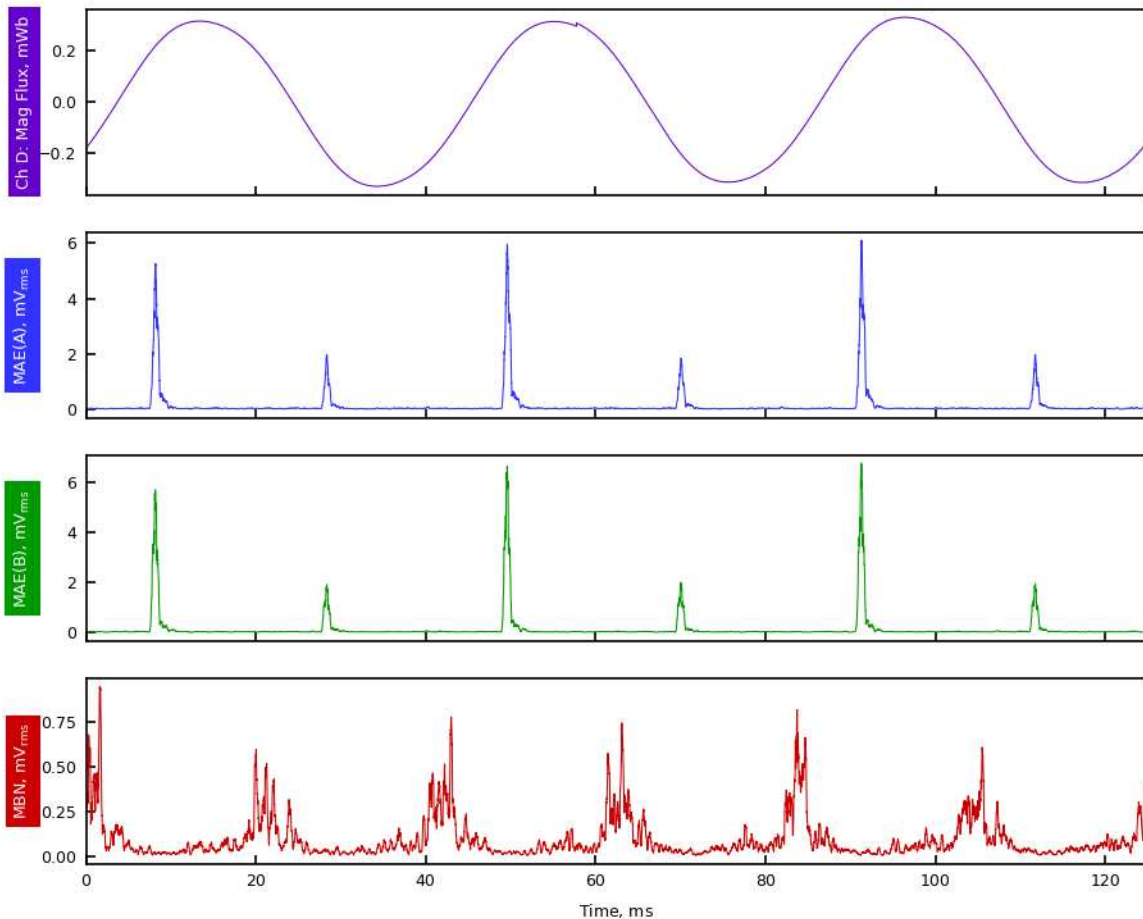


Figure 3.9: An example of windowed RMS waveforms. The data of Figure 3.8 (test 21 at 121 s) are squared and convolved with a rectangular window of 500 pt ($250 \mu\text{s}$) and the square root is taken element-wise.

3.6.2 MAE/MBN Cycles

Since the signal is repetitive with an integral number of cycles per waveform (by design), the moving RMS values over the waveform can be averaged to get a picture of one complete cycle, as in Figure 3.10, where one complete magnetization cycle is separated into four regions by the sign of second (blue-black and red-green being negative and positive, respectively) and first derivatives (black-red: positive/blue-green: negative) of the magnetic flux. Again, a few observations can be noted. (1) Two clearly defined peaks in the MBN signal occur in each half-cycle as the flux changes sign ($|\Phi| < 150 \mu\text{Wb}$) and on return to zero ($150 \mu\text{Wb} < |\Phi| < 225 \mu\text{Wb}$). (2) Two peaks appear in the MAE signal at approximately $\pm 300 \mu\text{Wb}$, very near the maximum in magnetic flux. (3) In general, the MAE behavior between the two *independent* PT are very similar and approximately equal in magnitude. (4) The MAE/MBN data display little variation over the five cycles collapsed here, excepting extrema in magnetic flux.

Point (1) is consistent with MBN behavior in other materials[11], where the initial activity is due primarily to growth of favorably-aligned domains followed by rotation at higher fields[27, 38]. The behavior of point (2) is also expected, although the region over which MAE is observed is rather narrow, being only at the very upper limit of a magnetization cycle.

To give an idea of the spectral content of the Barkhausen and magnetoacoustic emission over time, a typical periodogram over two magnetization cycles is presented in Figure 3.11 for the same waveforms in Figures 3.8–3.10 prior to digital (FIR) filtering. The choice of cutoff frequencies for the FIR filter is made evident as the noise manifests primarily in the 10–100 kHz range for MAE response. (Barkhausen noise at the input of the oscilloscope is necessarily constrained to the frequency range of 5–150 kHz by the analog filter, of course.) While some changes in the frequency response of the measured noise over the course of a test, obtaining consistent, meaningful results was difficult and costly from a computational standpoint; characterization in the frequency domain remains an open but likely fertile

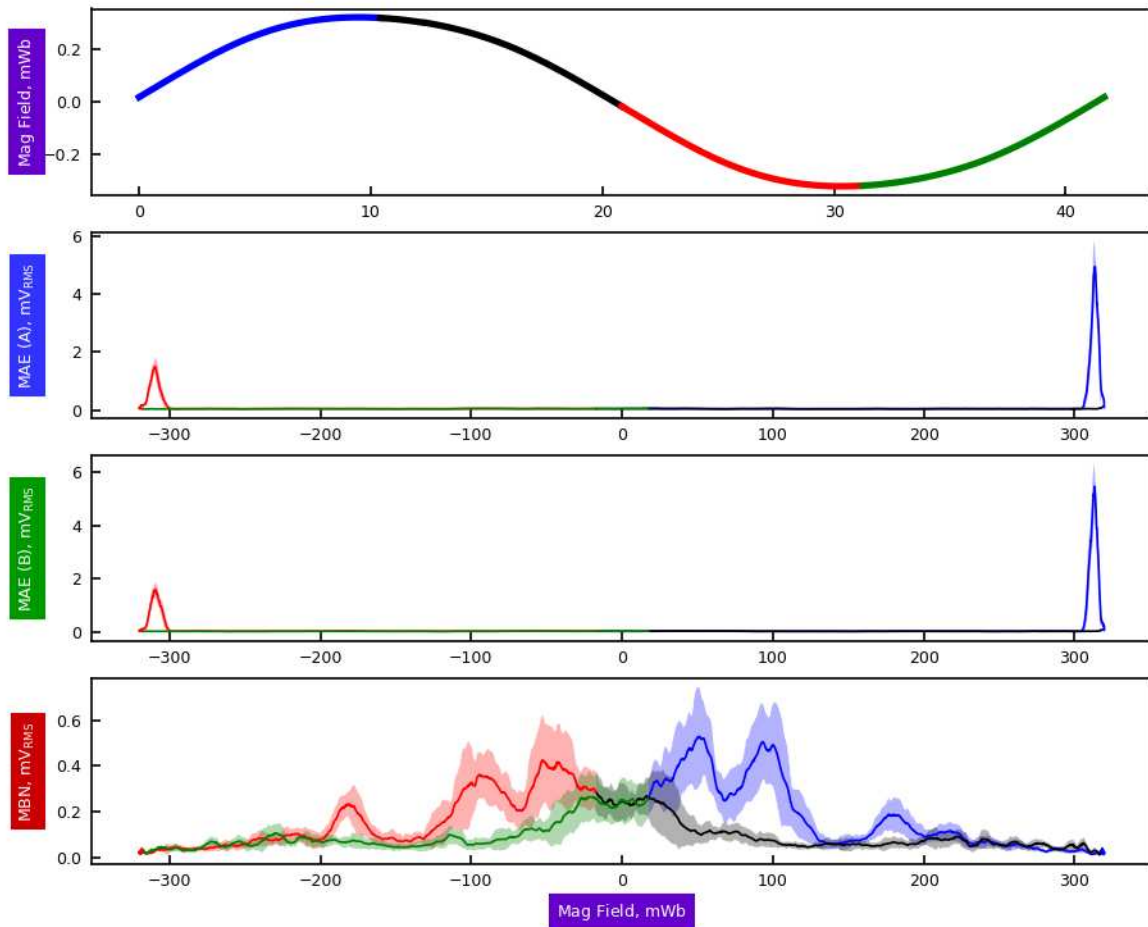


Figure 3.10: Magnetoacoustic and Barkhausen emission waveforms averaged over twenty cycles. The data of Figure 3.9 (test 21 at 121 s) are folded, centered, and averaged to show behavior over one complete cycle. MAE/MBN waveforms (V_{rms}) are plotted to the magnetic flux (Wb) which is shown as a function of time at top.

opportunity for future work.

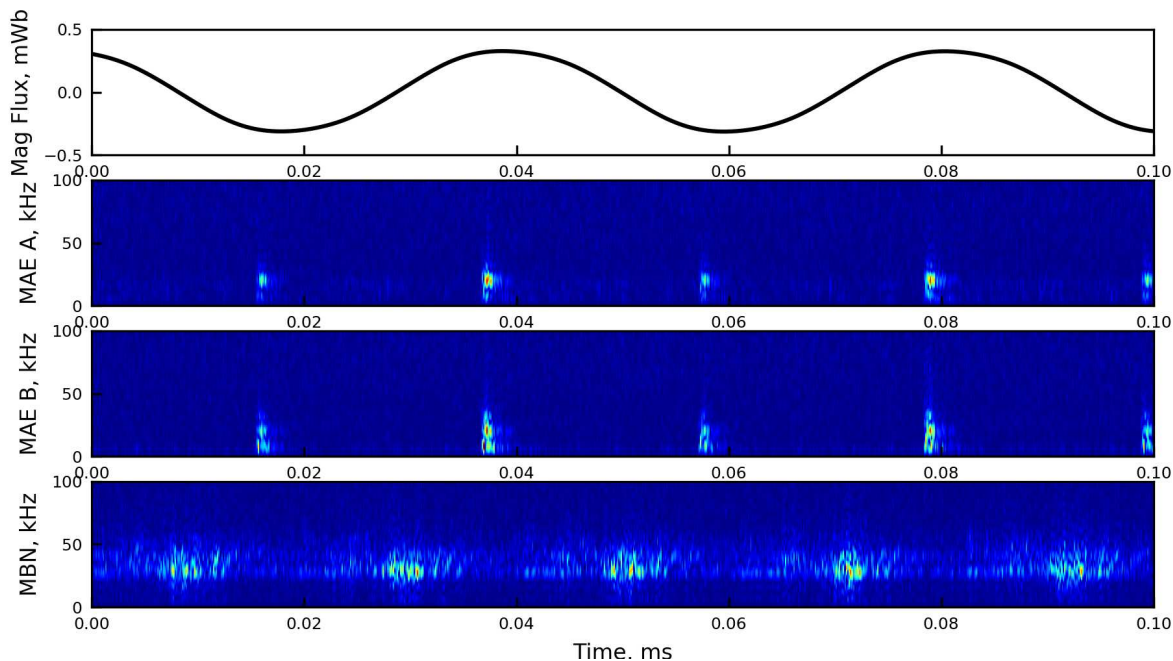


Figure 3.11: Typical periodograms for a single measurement, showing the evolution of spectral content of Barkhausen and magnetoacoustic emission over several cycles of magnetization. Data are from Figure 3.8 prior to digital filtering.

3.6.3 Characterization of Experimental Arrangement

Given the many sources of interference in the measurements described, it is worth considering the extent to which they affect subsequent analyses. In this section, the phase lag $\Delta\theta$ and total harmonic distortion/noise (THD+N) are quantified for the various stages of magnetization for the apparatus in the absence of a steel sample. The measured quantities are shown in Figure 3.12 and consist of the voltage output of the power amplifier, current through the magnetizing coil, magnetic field in the center of the core (through ABS plastic), and magnetic flux through the core as determined by Equation (3.3). Figure 3.13 shows typical waveforms for $f_d = 24$ Hz, normalized to ± 1 V to qualitatively demonstrate noise, distortion, and phase shift relative to the waveform generator output (the reference signal).

Determination of the phase difference is accomplished by cross correlation of the respective (normalized) waveform $V_i[t]$ with a reference signal, $V_{ref} = \sin 2\pi f_d t$. The location of

the peak in this function corresponds to the time shift which yields the maximum

$$\tau = \arg \max \frac{V_{ref} \star V_i}{f_{Sa}}, \quad (3.4)$$

where f_{Sa} is the sampling frequency. The phase shift is then calculated, $\Delta\theta = 2\pi[\tau f_d \bmod 1]$ rad.

Estimation of distortion (THD+N) is also performed on discretized waveforms in Python. After determining the fundamental frequency for a given waveform in the Fourier domain, the local spectrum is subtracted to yield the noise spectrum S_n . The RMS noise signal is then computed in the time domain ($V_{n,rms}$) and divided by the original (total) RMS to give the distortion,

$$\text{THD+N} = 20 \log \frac{V_{n,rms}}{V_{rms}}. \quad (3.5)$$

Class D amplifiers rely on pulse width modulation with high switching frequency⁹ to produce the desired signal response at their output. While much of the resulting noise can be filtered, the amplifier output voltage—on the order of $\pm 25 V_{pp}$ —still contains significant high frequency noise as shown Figure 3.13 (recall that the voltage waveforms are scaled, and that the noise in the figure is roughly 25 times that shown). The noise and distortion at this stage is essentially independent of magnetizing frequency, but decreases at higher driving amplitudes, as shown in Figure 3.14. At the operating point for these tests (24 Hz and 400 mV), the THD+N is about -50 dBc.

In contrast to the output voltage, distortion of the driving coil current, i_D , exhibits a strong dependency on magnetizing frequency—for higher driving amplitudes in particular—as shown in Figure 3.15. While high frequency noise is reduced, being effectively filtered by the inductance of the driving coil itself, harmonic distortion becomes significant at low frequencies due to the effects of magnetic hysteresis in the transformer core. At the magnetizing

⁹Switching frequency, f_{sw} , for the TDA7498E is 310 kHz

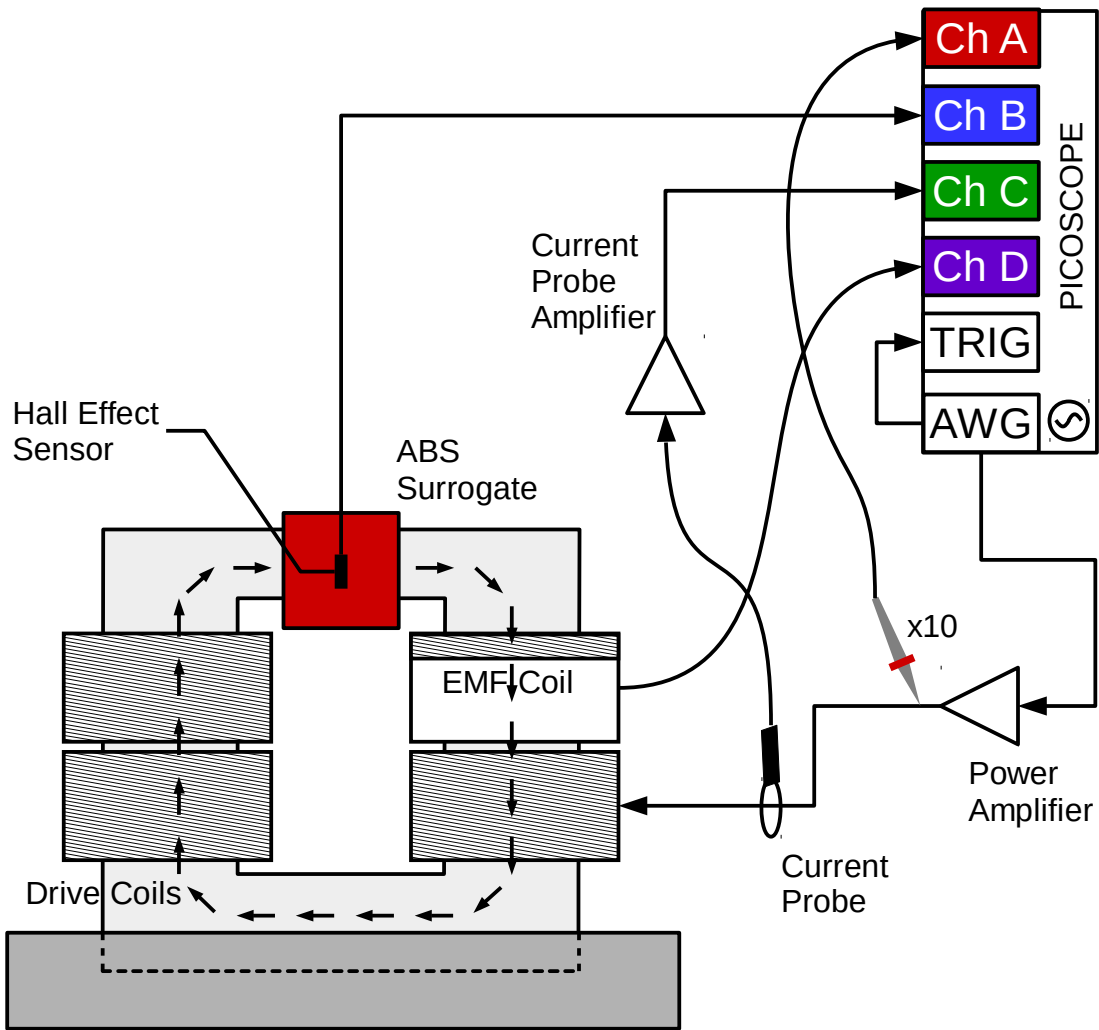


Figure 3.12: Physical arrangement for characterizing the apparatus. A Hall effect magnetic field sensor (Allegro Microsystems A1302) was placed in an ABS plastic RP of sample dimensions and field excitation was varied with waveform generator output voltage and frequency to determine phase difference and THD+N for power amplifier output voltage (Channel A) and current (C), magnetic field density (B), and flux derivative (D).

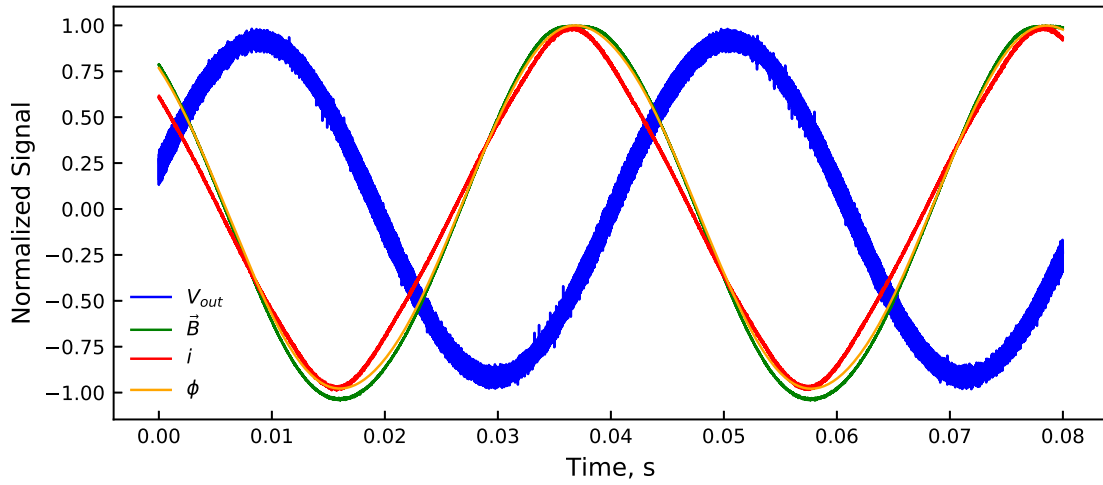


Figure 3.13: Two magnetization cycles demonstrating amplifier output voltage, magnetic flux density, driving coil current, and core flux characteristic behavior. Signals are normalized to their respective maxima to show qualitatively relative phase lag, noise level, and distortion; actual level for, e.g. V_{out} is $\approx 25 V_{pp}$ with superimposed switching noise of $\approx 1.5 V_{pp}$.

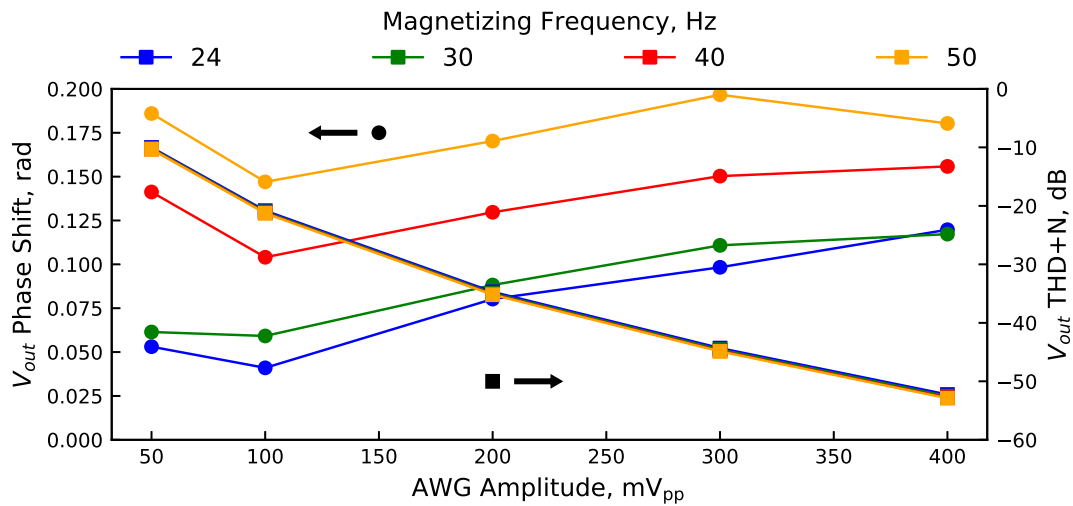


Figure 3.14: Total harmonic distortion and phase of power amplifier output voltage relative to waveform generator output voltage in the absence of a sample (9 mm air gap).

frequency chosen in these tests, THD+N is a bit worse than -60 dBc, but is still considered tolerable. A lower magnetizing frequency, while reducing losses to eddy currents and increasing the effective depth of the MBN sensor, would likely result in too much distortion, however.

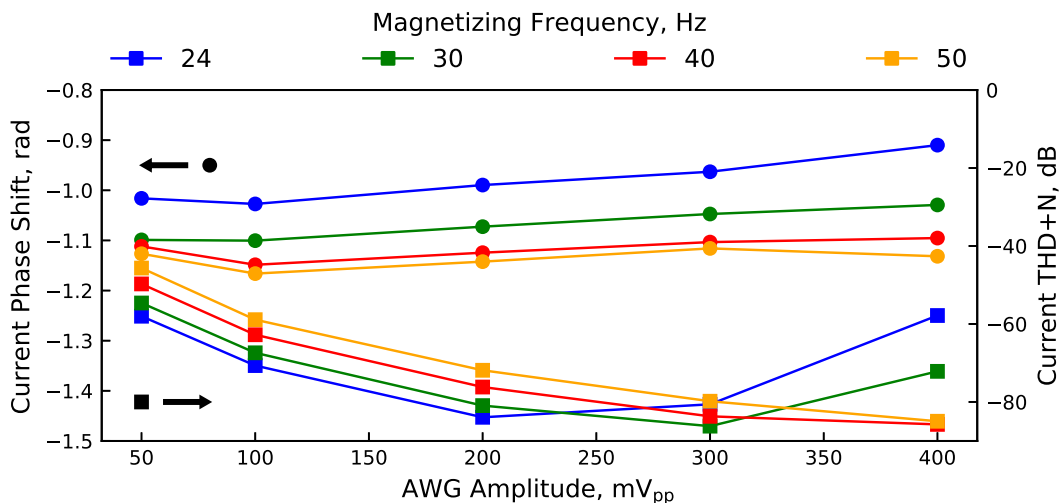


Figure 3.15: Total harmonic distortion and phase of magnetic core current relative to waveform output voltage in the absence of a sample.

Measurement of the magnetic flux density, \mathbf{B} , in the absence of a sample is accomplished by placing a hall effect sensor (Allegro Microsystems A1302) in a plastic parallelepiped sample surrogate ($\mu_R \approx 1$) which is then mounted in the core. The location of the sensor is in the center of the magnetic circuit where the flux density is highest. Figure 3.16 demonstrates the behavior as the driving magnitude and frequency are varied in the region around the operating point, and in general the behavior is very similar to the coil current of Figure 3.15, as expected. (The difference in phase of π rad is due to the bi-directional sensor being placed backwards in the apparatus.) The sensor used has a linear response to magnetic flux in the range of ± 0.2 T, after which it saturates, causing significant distortion. Since the THD+N is less than -80 dBc, it is clear that \mathbf{B} falls within that region (that is, when the magnetic circuit has a 9 mm air gap with permeability a small fraction that of steel). Indeed, using the manufacturer-supplied sensitivity of 13 V T^{-1} gives a maximum flux density of 0.18 T in

this arrangement.

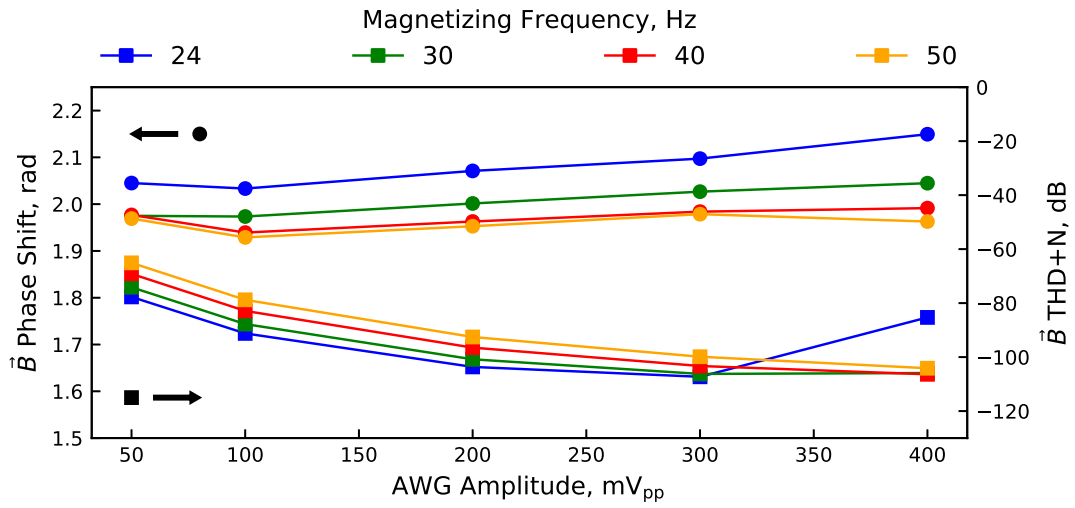


Figure 3.16: Total harmonic distortion and phase relative to waveform generator output for magnetic flux density in the absence of a sample.

Finally, the phase shift and distortion in magnetic flux through the core, as measured by EMF and computed by Equation (3.3) is presented in Figure 3.17. The phase shift of $\Delta\theta_{\Phi} = 2.147\text{rad}$ relative to the AWG output is in good agreement with the directly-measured flux density, $\Delta\theta_B$, suggesting determination of flux in this manner is warranted. THD+N measurements, are several decades lower and noisier due to the suppression of higher frequency content by numerical integration.

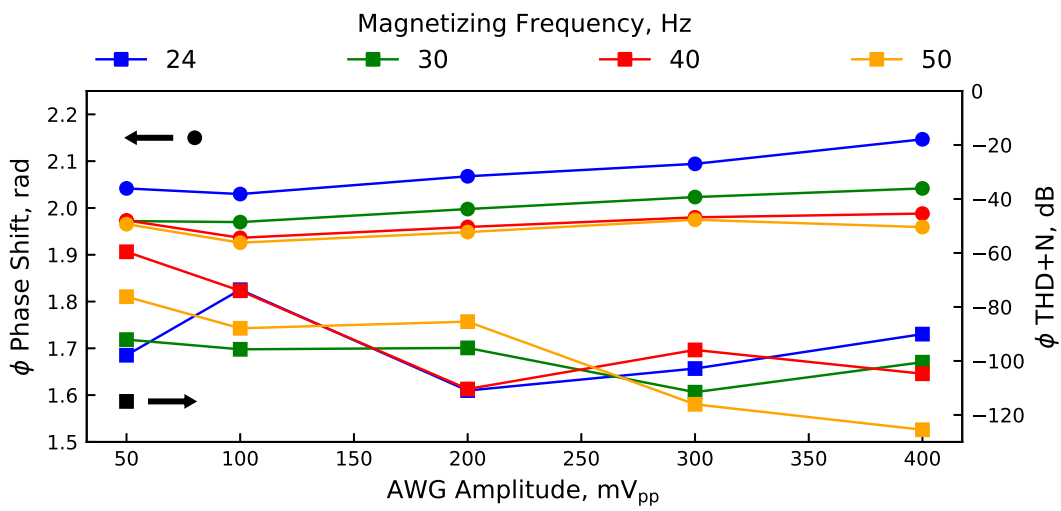


Figure 3.17: Total harmonic distortion and phase of magnetic flux detected via pickup coil relative to waveform generator output in the absence of a sample.

CHAPTER 4

RESULTS

In this chapter experimental data obtained by the methods of the previous section are presented and discussed, beginning with results of the diffusible hydrogen (glycerine) tests. Interpretation of time-dependent data with regard to diffusing hydrogen as it is discharged from samples is given first for the bulk magnetic properties measured via the core flux sensing coil. Attention is then given to Barkhausen noise and magnetoacoustic data obtained in concert with flux.

4.1 Cathodic Charging

Diffusible hydrogen contents for AISI 4140 steel samples were determined by glycerine tests prior to MAE/MBN tests and are presented for the tempering and charging conditions of Tables 3.4 and 3.5 in Figure 4.1. It is apparent that samples of highest hardness (tempered at 210 °C) have the highest hydrogen diffusivity and solubility. Sakamoto et al. [23] attributed the higher solubility for tempering temperatures between 100–300 °C to the precipitation and growth of ϵ -carbides prior to agglomeration at more elevated temperatures: increased surface area provides a larger number of deeper trapping sites for diffusing hydrogen.

Still higher tempering temperatures causes growth and coalescence of these carbides reducing the interfacial area; hydrogen diffusivity increases and solubility is lowered [2, 23]. Being a measure of total diffusible hydrogen made over the course of two days, a glycerine test is not an effective determinant of diffusivity directly. However, by examining the overall trend in Figure 4.1, the amount of time spent charging a sample can be considered to reflect the relative degree of mobility to a certain degree. Thus with its lower overall slope with time, the diffusivity is, in fact, highest for $T_{temp} = 427^\circ\text{C}$ —longer charging times increase the overall dissolved hydrogen less for these samples than others, suggesting trapping effects are less prominent at this temperature.

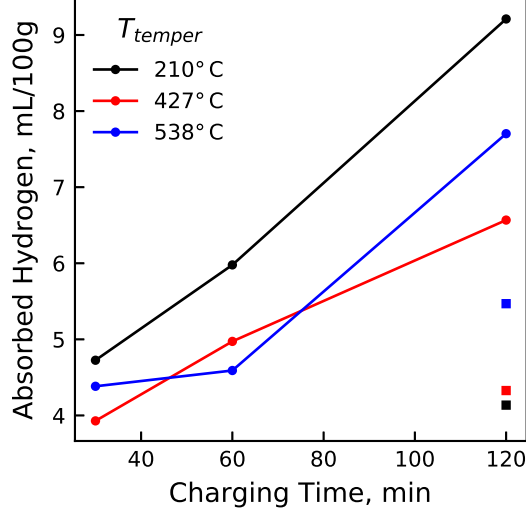


Figure 4.1: Amount of hydrogen cathodically absorbed in samples of AISI 4140 steel for various charging times. The electrolyte was 0.5 M H_2SO_4 with 2 g l^{-1} thiourea; current densities are denoted by circles (10 mA cm^{-2}) and squares (5 mA cm^{-2}).

4.2 Eddy Currents: Resistance

From measurement of the EMF induced by the changing core flux through the magnetic circuit encircled by the twenty-turn coil of Figure 3.5, variation in three bulk quantities can be observed during outgassing of hydrogen in the studies performed. The magnitude of the flux is dependent on the magnetic permeability and other factors, but the measurement is also sensitive to eddy currents which are themselves influenced by the permeability and conductivity of the sample (and core, the properties of which here assumed to be constant). That is, changes in core flux amplitude may be attributable to either μ , σ , or some combination. In the frequencies considered (24 and 25 Hz), eddy current losses could be appreciable; however, available reported effects of hydrogen on conductivity are minimal[32], unless mesoscopic damage (e.g. cracking) is allowed to occur at sufficiently high current densities[60].

To determine the extent to which hydrogen-dependent resistance changes could affect the measurements that follow through eddy current damping, 280 mm long low-carbon steel

wires ($\varnothing 0.356$ and 1.041 mm) were charged in the same manner as Section 3.2, but masked with polyimide tape to a definite region (145 mm) submerged in the electrolyte. After charging, the resistance was measured with a 4-lead Kelvin configuration (Keithley 2000) in a container floating in a 30 °C water bath for 7500 s. Temperature was monitored with a separate probe in the floating container to correct for any thermally-dependent resistance and/or thermoelectric changes which could be erroneously attributed to hydrogen¹⁰. Figure 4.2 presents the raw resistivity/temperature data for one such test and corrections thereto.

After correcting for temperature effects in the resistance measurement, deviation in resistance with hydrogen content is found to be minimal, if at all, and does not vary in any predictable or meaningful way. Others have observed such an effect which appeared to establish a direct correlation[4, 5] between electrical impedance and hydrogen in steel; however their method involved the deliberate use of eddy currents which depend not only on impedance but also on electrical permeability. Variation in other magnetic properties (addressed in subsequent sections) combined with the apparent lack of a clear relationship for DC resistance suggests that previous work directed at a nondestructive hydrogen detection method by eddy current may have misattributed the effect to the latter, and that a reframing of that data in the context of macroscopic *magnetic* properties over *electronic* may prove fruitful.

4.3 Magnetic Flux: Phase

Discussion of magnetic properties begins with examination of the change in amplitude and phase lag for the magnetic circuit consisting of the laminated iron magnetizing core and the sample itself (through the minor dimension, 9 mm) for the initial tests of AISI 4340 steel. The phase lag is taken as the change in overall phase (as determined by autocorrelation) relative to the initial value ($\theta_0 = 2.147$ rad for the core without a sample as per Section 3.6.3), and is reported in Figure 4.3. Errors (shown in every third bar in Figure 4.3 for clarity) are

¹⁰Even in a 4-lead resistance measurement, the error in a DC measurement is significant. Noise and temperature drift in the leads, junctions, and even the instrument itself are nontrivial.

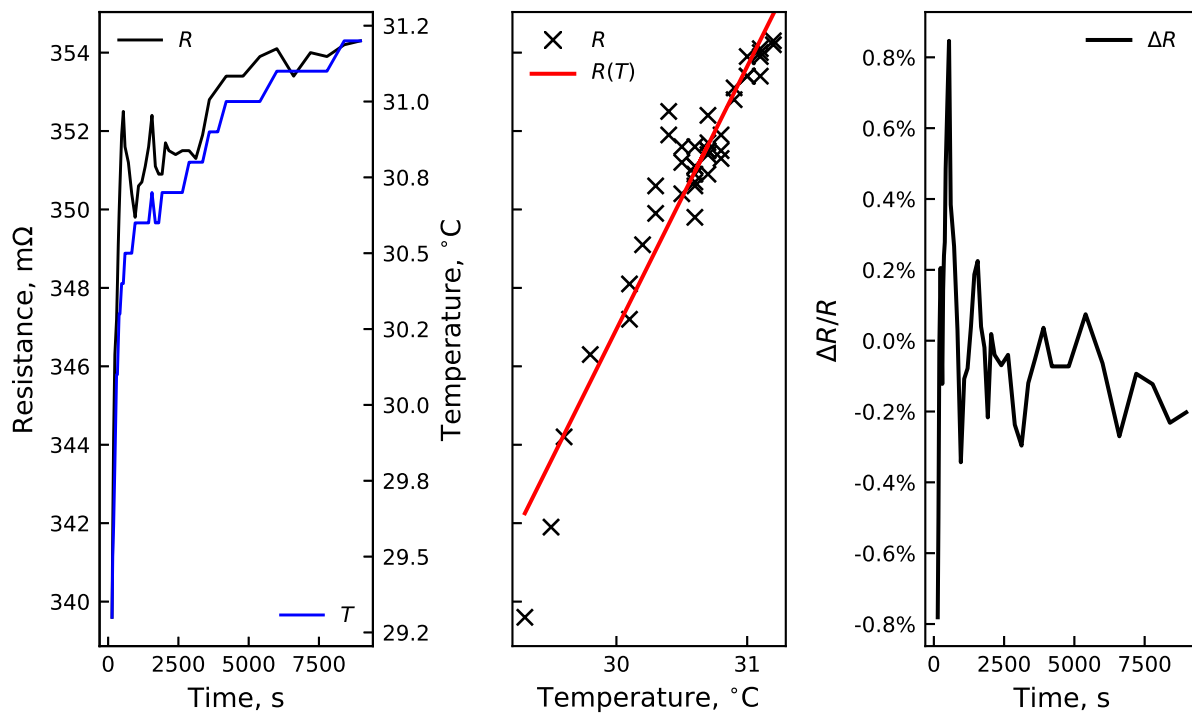


Figure 4.2: Changes in resistance of a low-carbon steel wire (0.356 mm dia.) after charging at 10 mA cm^{-2} for one hour. Minute changes in temperature of a few degrees appear to correlate with the resistance (left), which include Seebeck-type junctions or simply the temperature coefficient of the wire and leads. The linear fit between temperature and measured resistance (center) is subtracted to obtain the relative change due to other factors (right).

of the order of ± 0.1 rad.

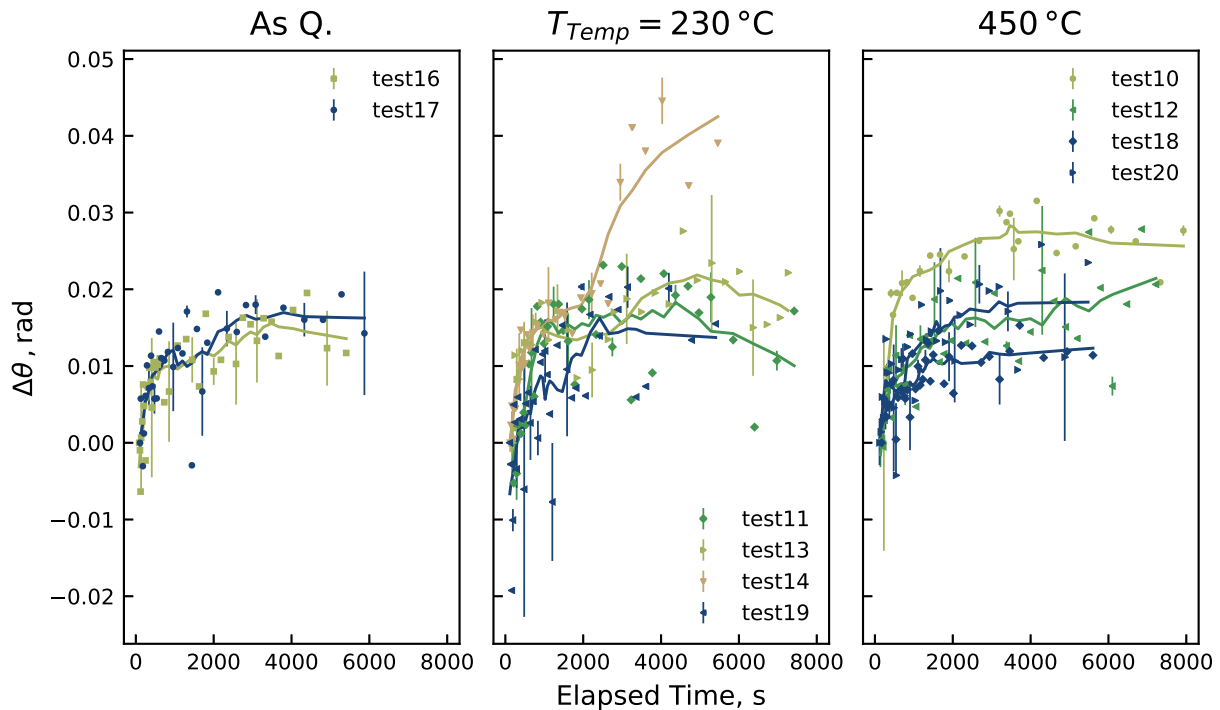


Figure 4.3: Change in core flux phase with time as hydrogen desorbs for AISI 4340 tests. Data points are the phase shift relative to the initial value at $t = 0$ (for the core without a sample, $\theta = 2.147$ rad). Lines are the results of a Savitzky-Golay filter performed on the points of order 1 and window length 7 added to aid the eye. Plot colors indicate charging current density (mA cm^{-2})/time (minutes): 1/30 (—), 1/15 (—), 10/30 (—), and 10/60 (—).

Figure 4.4 shows the phase lag for AISI 4140 steel samples, and the results are similar to those of AISI 4340 steel (Figure 4.3), with the same general behavior observed: as hydrogen is desorbed from the material, the phase lag increases asymptotically to roughly 0.02 rad relative to the initial value¹¹. Unfortunately, the high degree of variability in the measurement makes meaningful comparison between tests or heat treatments difficult: an alternative phase determination method, such as with a lock-in amplifier would provide vast improvement in this regard.

¹¹The sample in test 31 was not fully seated in the core, so the magnetic field did not penetrate into the entire sample; similar anomalies are shown in much of the remaining graphs with this test, but the data is included for posterity.

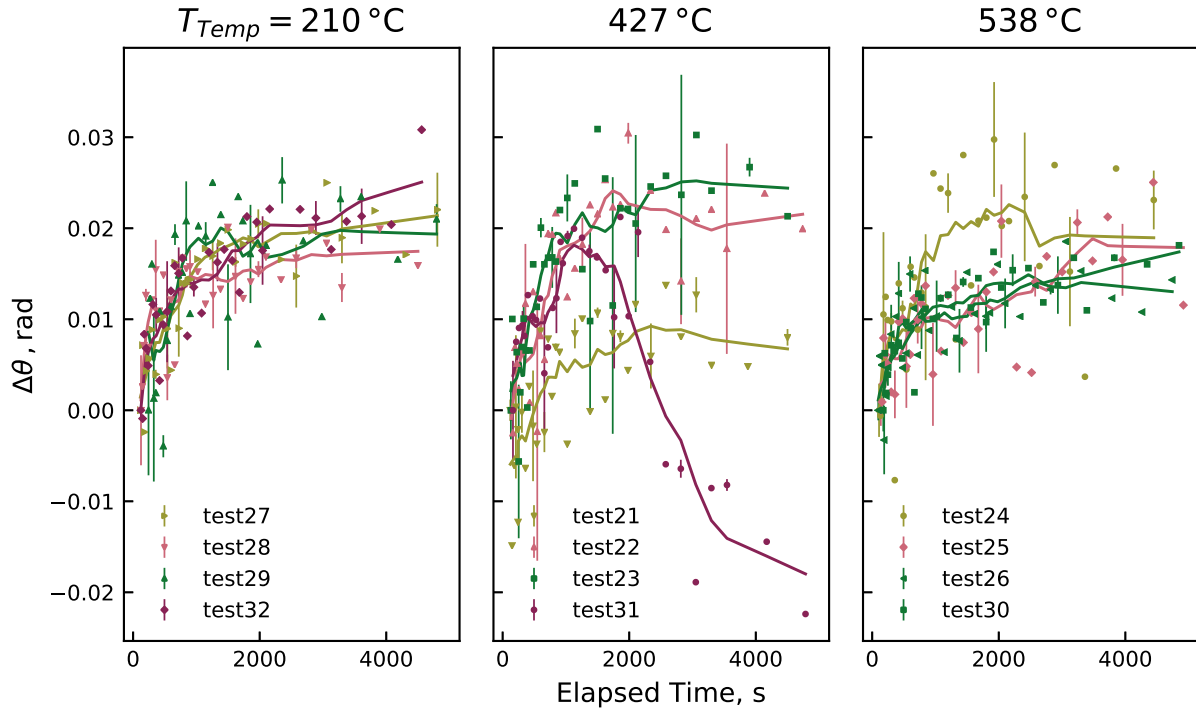


Figure 4.4: Change in core flux phase with hydrogen outgassing for AISI 4140 steel tests. Data points are the phase shift relative to the initial value. Lines are the results of a Savitzky-Golay filter performed on the points of order 1 and window length 7 added to aid the eye. The phase lag may be related to magnetic hysteresis, after effect or (given the relatively high frequency of magnetization) eddy current losses which are dependent on hydrogen concentration. Plot colors indicate charging current density (mA cm^{-2})/time (minutes): 5/120 (—), 10/30 (—), 10/60 (—), and 10/120 (—).

4.4 Magnetic Flux: Amplitude

Variations in the amplitude show a greater degree of robustness, however, as demonstrated in Figures 4.5 and 4.6 for samples of 4340 and 4140 steel, respectively. The effect of hydrogen outgassing on the magnetic flux through the entire circuit changes with RMS value determined by Equation (3.3) over time. Changes in flux can be related to variation in the permeability of an element i of the circuit by the reluctance $\mathcal{R}_i = l_i/\mu_i A_i$, as

$$\Phi = \frac{\text{mmf}}{\sum_i \mathcal{R}_i}, \quad (4.1)$$

where the magnetomotive force is $\text{mmf} = NI = \oint H \, dl$ if the applied field H is assumed to be relatively constant. Total change in flux over the course of a test was small—only on the order of 0.1%—but considering the relative length of the circuit through the sample (9 mm) to the overall core (250 mm), the differences in permeability could be significant.

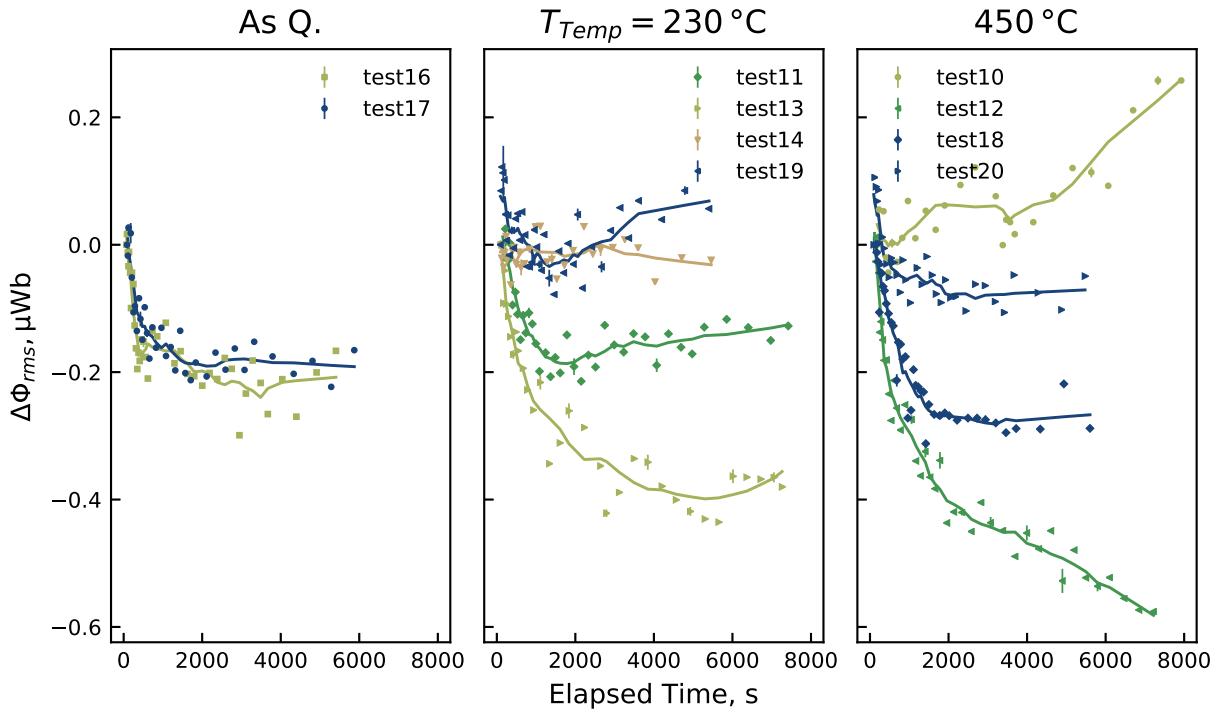


Figure 4.5: Change in core flux amplitude (RMS average) with hydrogen outgassing for AISI 4340 steel tests. Data points are the change in magnetic flux relative to the initial value. Lines are the results of a Savitzky-Golay filter performed on the points of order 1 and window length 7 added to aid the eye. Plot colors indicate charging current density (mA cm^{-2})/time (minutes): 1/30 (—), 1/15 (—), 10/30 (—), and 10/60 (—).

Hydrogen has the effect of increasing the apparent permeability, observed as a negative slope during initial outgassing. A positive effect on permeability is contrary to expected behavior if hydrogen is present only at tetragonal interstitial sites, but would be consistent with occupation of octahedral sites, especially around vacancies[34, 61]. Following the initial decrease in total flux, there appears a stable region for apparent permeability and even some recovery, as in the case of 4340 steel tempered at 230 °C. For higher strength samples

($T_{temp} = 210\text{ }^{\circ}\text{C}$ in Figure 4.6), the period of recovery appears to follow a secondary loss in permeability at about 2 ks which may reflect a transition from one hydrogen trapping site to another.

Even though the changes in MBN amplitude are shown to be less than about $0.5\text{ }\mu\text{Wb}$ while the absolute value is roughly three orders of magnitude higher, the effects of hydrogen desorption are still apparent. High strength samples of 4140 steel ($T_{temp} = 210\text{ }^{\circ}\text{C}$) demonstrate the least overall change, being less than $0.2\text{ }\mu\text{Wb}$, but also appear to exhibit the most consistent behavior: an initial decrease in flux followed by a period of about 1 ks of stagnation, and an eventual recovery of total flux.

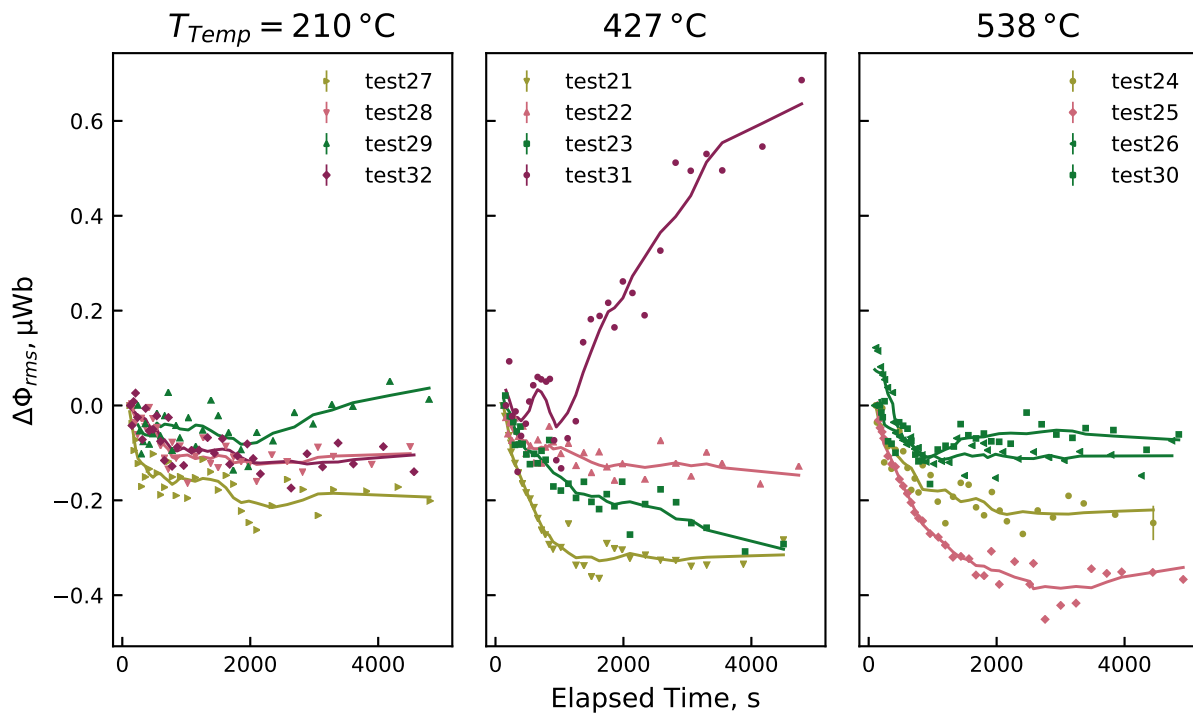


Figure 4.6: Change in core flux magnitude (RMS average) with hydrogen outgassing for AISI 4140 steel tests. Data points are the change in magnetic flux relative to the initial value. Lines are the results of a Savitzky-Golay filter performed on the points of order 1 and window length 7 added to aid the eye. Plot colors indicate charging current density (mA cm^{-2})/time (minutes): 5/120 (—), 10/30 (—), 10/60 (—), and 10/120 (—).

4.5 Magnetic Flux: Harmonic Distortion

Eddy currents cause a phase lag and reduce the amplitude of the magnetic flux in conducting materials via an effective imaginary term in permeability, making this loss frequency dependent. This phenomenon is linear in nature, however, so eddy currents do not contribute to any nonlinear behavior in the magnetization—observed, for example, as harmonic generation for sinusoidal signals. On the other hand, magnetization is in general a highly nonlinear process and its various features manifest as decreases in amplitude or phase shifts at the fundamental frequency and generation of odd harmonics. Supposing, then, that hysteresis is the source of observed changes in phase shift and amplitude, variation in the nonlinearity of the signal measured magnetic flux sensor around the core should correlate in a manner similar to these quantities.

One straightforward and useful measure of nonlinearity (and therefore a crude measure of hysteresis) is total harmonic distortion and noise (THDN), which is a ratio consisting of all frequency content that is not considered part of the fundamental (that is, driving frequency f_d) divided by the total spectral content. Total harmonic distortion is computed for each data point and presented in Figures 4.7 and 4.8 for charged samples of AISI 4340 and 4140 steel, respectively. Due to minute differences in mounting conditions, the change in distortion, ΔTHDN is given relative to the initial value for that test. Differences as high as 0.4 dBc are observed while initial values are on the order of -48 dBc. It should also be noted that the harmonic distortion is computed for the EMF in the coil, *not* the integrated flux as in Figure 3.17, and is thus several orders of magnitude higher (about 30 dBc).

Hydrogen has the immediate appearance of reducing the harmonic distortion computed as THDN. This decrease in hysteretic nonlinearity with hydrogen has been noted by Ramesh et al. [50] as a reduction in the coercivity in iron which was cathodically charged in sulfuric acid/thiourea. Coercivity is a measure of domain wall pinning energy and site density, is directly related to the parameter k in the Jiles-Atherton model ($H_c = k$ for magnetically soft materials)[49]. By doubling of the value of k in Equation (2.35) as shown in Figure 2.8, the

nonlinearity is, in fact, decreased as indicated by the lower value of the third harmonic ratio, A_3/A_1 of that figure. Dissolved hydrogen is, of course, expected to increase the number of pinning sites, so a concomitant increase in k is sensible.

However, an increase in coercivity expands the hysteresis curve, reducing the overall observed flux amplitude. Such an effect is not observed in the data of Figures 4.5 and 4.6, which show an *increase* in amplitude at higher hydrogen concentrations (lower times). These two opposing trends may be one cause of the tendency for the harmonic distortion data to depart from a simple exponential or quadratic decay-type function and exhibit multiple peaks over time. Alternatively, the behaviors observed in both flux amplitude and harmonic distortion can be reconciled by a relative increase in the Jiles-Atherton model parameter a in Equations (2.34) and (2.35) and outlined in Figure 2.8, although the semi-empirical nature of the model does not necessarily elucidate any direct physical phenomena at the microscopic level.

Also of note in Figure 4.7 is an apparent change in behavior from the steep increase in harmonic distortion followed by a near steady-state condition as hydrogen is lost for as quenched samples (tests 16 and 17) to more gradual behavior in tempered samples (e.g. tests 10, 11, and 14). More severe charging conditions (higher current density or time) seem to cause a return to the stepped behavior for tempered samples, with those at 10 mA cm^{-2} and 60 s exhibiting a transitional region between 1–2 ks (tests.17–20).

By contrast, smoother variation in harmonic distortion over time is more represented in higher strength samples of AISI 4140 steel ($T_{temp} = 210^\circ\text{C}$, with sharp discontinuities following rapid increases in distortion observed for higher tempering temperatures. It is also worth noting that repeated charging of samples (as was done in tests 30–32) resulted in a tendency towards a smooth discharge profile and a larger change in THDN overall.

4.6 Barkhausen Noise

Changes in Barkhausen emission with hydrogen outgassing in AISI 4340 and 4140 steel samples appear to coincide with the desorption profile behavior predicted by the Oriani

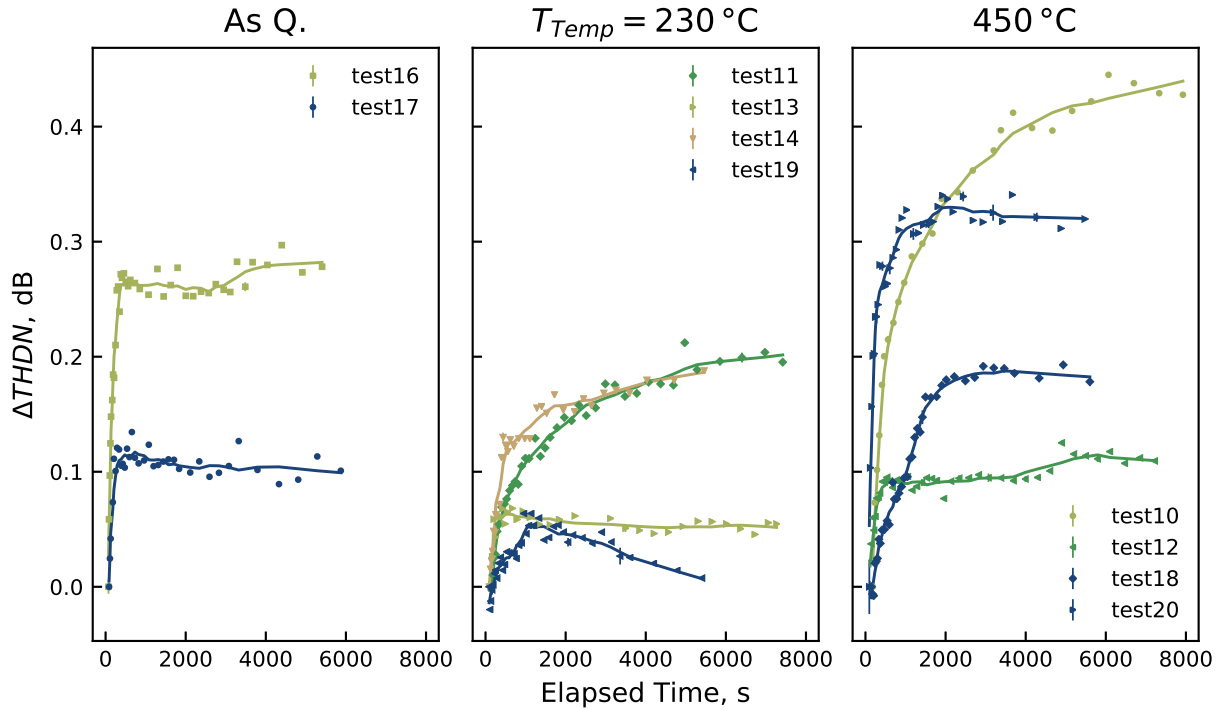


Figure 4.7: Change in core flux harmonic distortion with hydrogen outgassing for AISI 4340 steel tests. Data points are the change in harmonic distortion relative to the initial value (generally on the order of -48 dB). Lines are the results of a Savitzky-Golay filter performed on the points of order 1 and window length 7 added to aid the eye. Plot colors indicate charging current density (mA cm^{-2})/time (minutes): $1/30$ (—), $1/15$ (—), $10/30$ (—), and $10/60$ (—).

models of Section 2.1.2, suggesting a direct proportionality between MBN and hydrogen content. This section will introduce two methods for characterizing Barkhausen behavior in a given waveform: its so-called “energy” and the number of “events” which occur over its duration. Comparison will be made of overall trends for these two metrics between the two alloy systems and the various conditions. In general, the AISI 4340 steel tests are not well-defined by a simple function, but tests for AISI 4140 steel appear to follow a \sqrt{t} trend; a least squares fit is provided and discussed for these tests.

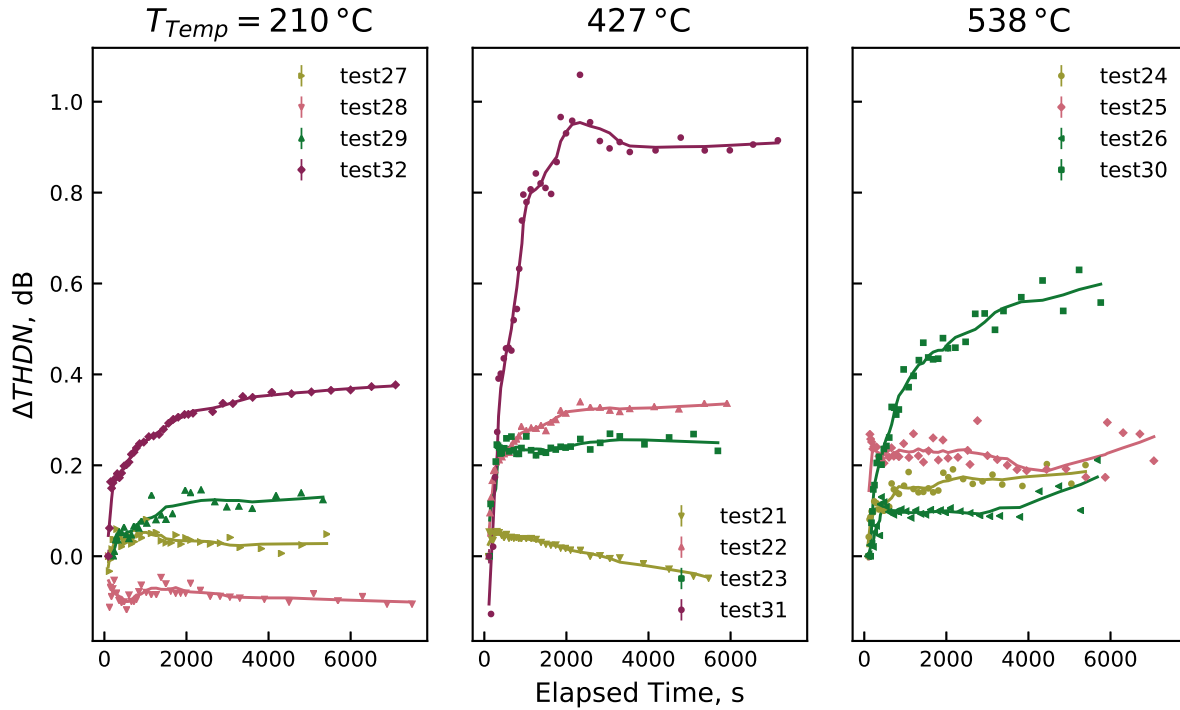


Figure 4.8: Change in core flux harmonic distortion with hydrogen outgassing for AISI 4140 steel tests. Data points are the change in harmonic distortion relative to the initial value. Lines are the results of a Savitzky-Golay filter performed on the points of order 1 and window length 7 added to aid the eye. Plot colors indicate charging current density (mA cm^{-2})/time (minutes): 5/120 (—), 10/30 (—), 10/60 (—), and 10/120 (—).

Considering now the effects of hydrogen on MBN in the 4340 alloy, the total MBN energy¹² in the filtered waveform

$$E = \int_0^{t_f} [V(t)]^2 dt, \quad (4.2)$$

for each measurement after charging is presented in Figure 4.9, where a Savitsky-Golay filter has been added to smooth the data. Owing to variation in coupling between search coil and the sample, the data points are presented as relative changes for each series (test), $S_i(t)$ such that

¹²Given the poorly-defined impedances and coupling coefficients in this setup, the “energy” here must be of completely arbitrary units.

$$S_i^n(t) = s_i [S_i(t) - S_i(0)] ,$$

where

$$s_i = \frac{1}{S_0} \times 100 \% \quad (4.3)$$

is a scaling factor which is also applied to estimates of the deviations $\hat{\sigma}_{ij}$. (Standard deviations as they relate to replicates are shown by error bars in these graphs for every third data point j to maintain visual clarity.) Normalizing in this way allows the data to be compared with the same ordinate, and is used as necessary in the graphs which follow.

It is clear from Figure 4.9 that the Barkhausen effect is enhanced upon charging with hydrogen, consistent with the rather limited body of prior work[15]. As hydrogen evolves from the surface, the MBN energy emitted is reduced to a minimum value some 10–25 % lower than the initial value in most cases, with the magnitude of the relative change corresponding to charging conditions (i.e. more variation is observed for higher current densities and/or charging times).

In some tests, such as those for a current density of 1 mA s^{-1} (tests 10, 13, and 16, a secondary behavior is observed after about one hour (4 ks) where the signal reaches a plateau and/or begins to increase. It is unclear whether this behavior can be attributed to a distinct phenomenon or if it is merely an artifact of the apparatus. It is conceivable, for example, that different types of traps releasing hydrogen at various rates would contribute to the surface desorption behavior observed here and as has been reported for e.g. low carbon[62] and Russian 4340-equivalent steel[24].

In Figure 4.10, a more pragmatic approach to MBN characterization is adopted. Here the number of Barkhausen counts, $\sum C_{mbn}$ in a given waveform is computed by first estimating the standard deviation ($\hat{\sigma}$) of the background noise for a region of the magnetization cycle

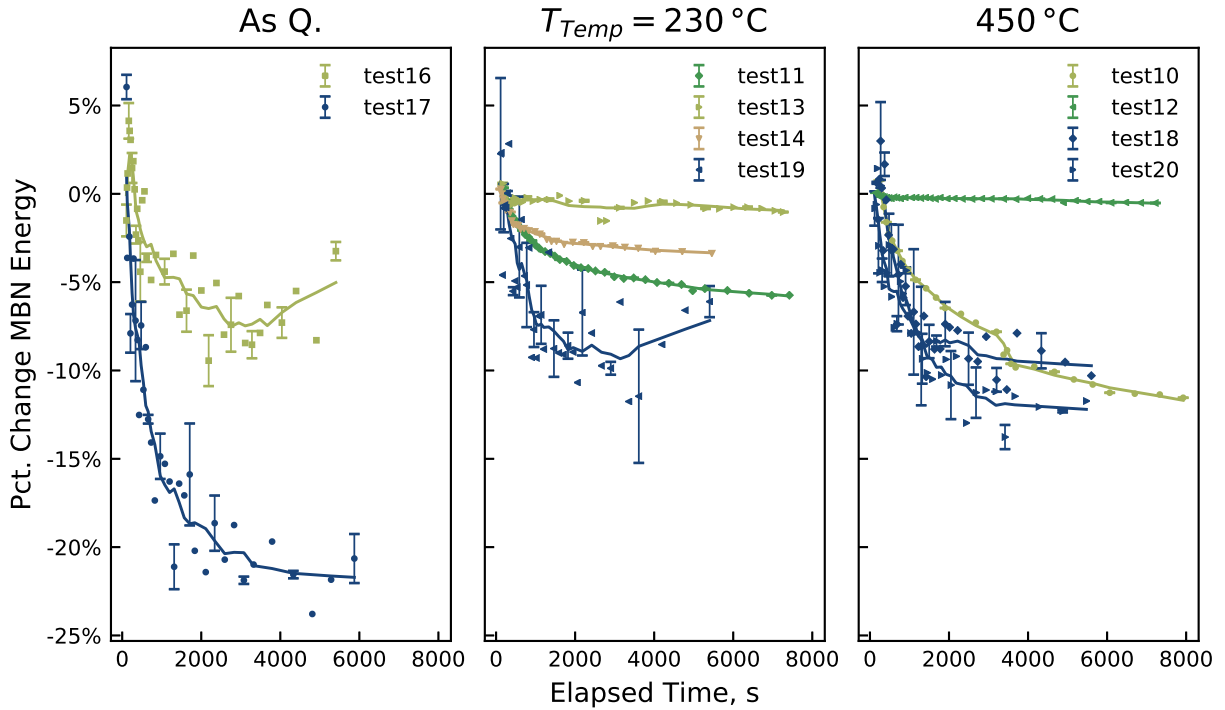


Figure 4.9: Decay of MBN energy with time for samples of AISI 4340 steel charged with hydrogen. A Savitsky-Golay filter of order 1 and length 3 is provided to aid the eye. Plot colors indicate charging current density (mA cm^{-2})/time (minutes): 1/30 (—), 1/15 (—), 10/30 (—), and 10/60 (—).

where Barkhausen emission does not occur¹³, then counting all of the points in the entire waveform where the voltage exceeds $\hat{\sigma}$ by some factor m :

$$\sum C_{mbn} = \sum^N i, \quad i = \begin{cases} 1 & V[i] \geq m\hat{\sigma} \\ 0 & V[i] < m\hat{\sigma} \end{cases},$$

where the value for m is taken to be 2, in the case of Figure 4.10. The number of Barkhausen events so determined reflects the same trends as those of the total energy, as in Figure 4.9, with a monotonic decrease falling exponentially with time as hydrogen diffuses out of the sample. Total changes over a given series vary between about 20–70 thousand events (out of

¹³Using Figure 3.10 as an example, bounds on the magnetic flux for the background region would be $|\Phi| > 200 \text{ mWb}$ for MBN and $|\Phi| < 250 \text{ mWb}$ for MAE. The flux “mask” is then applied to the respective waveform and $\hat{\sigma}$ is calculated.

1 MSA possible in a single waveform), and appear to stabilize the exponential behavior after 30 minutes (2 ks) of outgassing. Comparison of Barkhausen data here and for the 4140 steel data which bear remarkable resemblance to solutions of the Oriani model in Section 2.1.2, in particular those of lower equilibrium constant (e.g. $K = 1.67 \times 10^{-4}$), suggesting a direct correspondence between Barkhausen noise and hydrogen content.

Comparing results between sample groups for a single charging condition (e.g. 10 mA cm^{-2} and 60 minutes: tests 17–20) indicates that there is more significant change in MBN activity for harder samples, being most pronounced in the as quenched condition and demonstrating minimal variation at $T_{temp} = 450 \text{ }^\circ\text{C}$.

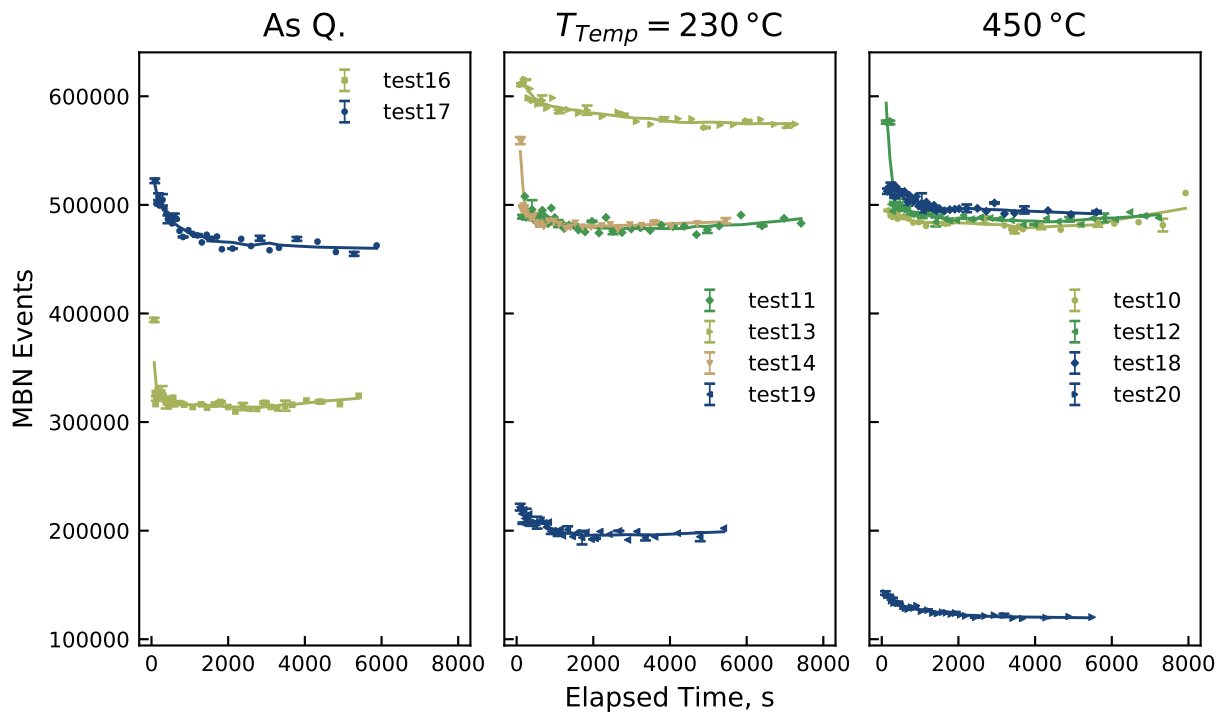


Figure 4.10: Evolution of MBN counts with time for samples of AISI 4340 steel charged to various levels. A Savitsky-Golay filter of order 1 and length 3 is provided to aid the eye. Plot colors indicate charging current density (mA cm^{-2})/time (minutes): 1/30 (—), 1/15 (—), 10/30 (—), and 10/60 (—).

Examination of the data for 4140 steel and supposing a linear relationship between Barkhausen noise and hydrogen content, and recalling the results of the simulation in Fig-

ures 2.3 and 2.4, in that the hydrogen concentration very near the surface decayed approximately as \sqrt{t} , the MBN series are plotted against the square root of time starting from the end of the charging stage. A decay of MBN energy is observed over time for each sample and for all charging conditions. As hydrogen concentration is presumably the single variable condition for the duration of the test, it can be concluded that diffusible hydrogen increases MBN in steel samples, perhaps by increasing domain wall pinning energy such that domain growth steps are larger, or by fundamentally altering the ferromagnetic behavior *viz.* permeability, susceptibility, conductivity, etc.

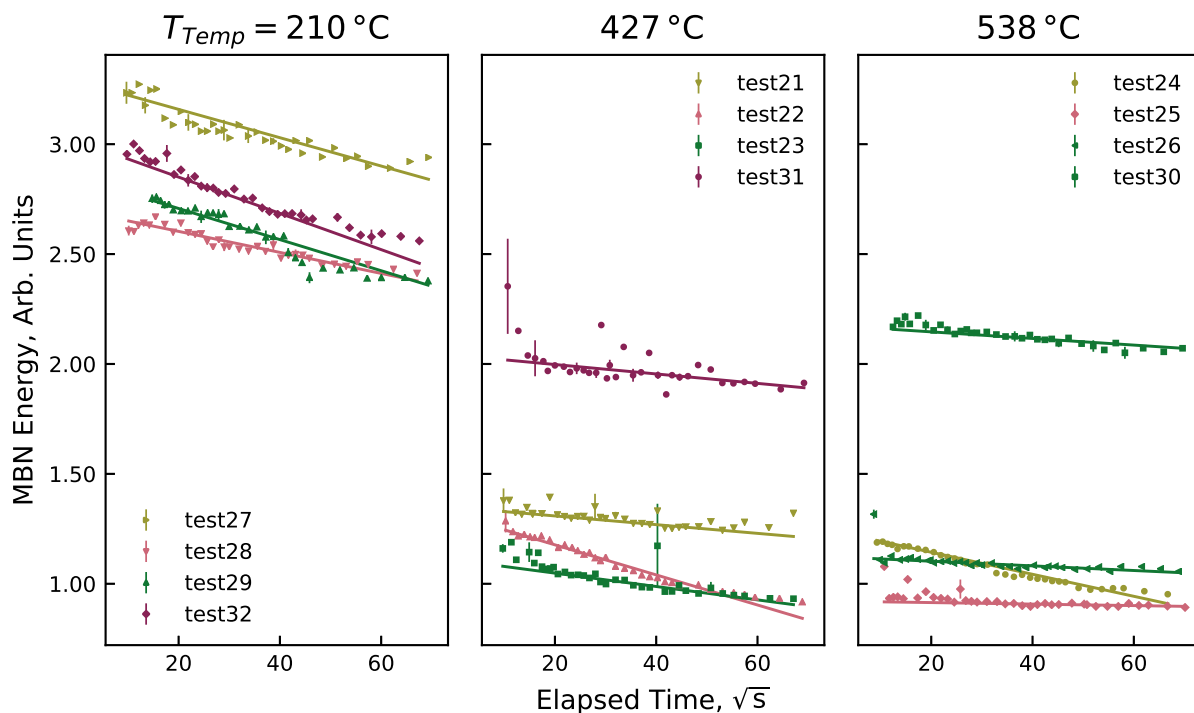


Figure 4.11: Decay of MBN energy with time for samples of AISI 4140 steel charged to various levels. Lines are least squares fits to the (normalized) data for each measurement obtained by integrating the squared waveform over time. Plot colors indicate charging current density (mA cm^{-2})/time (minutes): 5/120 (—), 10/30 (—), 10/60 (—), and 10/120 (—).

Indeed, the data in Figure 4.11 fall—within experimental error—upon a straight line, as indicated by fits of linear weighted least-squares for each series, suggesting agreement with MBN energy decay $\propto \sqrt{t}$. Departures from linearity are frequently the result of spurious

emissions (power supplies being the most likely culprit) for single points, while multipoint excursions may indicate distinct physical phenomena, such as increased trapping activity. Deviations of the latter type are mostly observed early in each series, which is consistent with the observed behavior in the Oriani models of Section 2.1.2.

Perhaps most notable in the data of Figure 4.11 is the consistency of the high-strength samples ($T_{temp} = 210^\circ\text{C}$ between charging conditions, which have very similar slopes and very little departure from linearity. By contrast, the evolution of MBN in softer samples demonstrates very different behavior depending on charging time and current density. From these observations alone it might be inferred that microstructure becomes more sensitive to the interplay between effective diffusivity and trapping as the tempering temperature increases. It is conceivable that precipitation of iron carbides, for which the trap binding energy $H_b \gtrsim 84 \text{ kJ mol}^{-1}$ [2], contributes to this sensitivity for the tempered martensite structures of tests 2–7 ($T_{temp} = 427$ and 538°C).

The relative simplicity of the apparent functional form of the Barkhausen energy, described by a steady decrease proportional to \sqrt{t} , affords the opportunity for direct comparison between tests via the results of the linear fit, as shown in Figure 4.12. A larger slope as shown for $T_{temp} = 210^\circ\text{C}$ ostensibly corresponds to a higher effective diffusivity, allowing faster reduction in hydrogen concentration at the surface. As the steel is tempered, the precipitation of carbides inhibits the diffusion of hydrogen, slowing the return to nominal magnetic characteristics.

Consistency in Barkhausen behavior is demonstrated in Figure 4.13, which shows the number of MBN events over time for each measurement as estimated from the number of points in each waveform exceeding a $2\hat{\sigma}$ voltage threshold. The data again fall to a \sqrt{t} decrease in activity with hydrogen outgassing, in much the same manner as the energy but with the same slope between nearly all tests.

A decrease in the *number* of events concomitant with a decrease in overall energy hints at a tendency for domain walls to be less inhibited in their motion through the sample, as

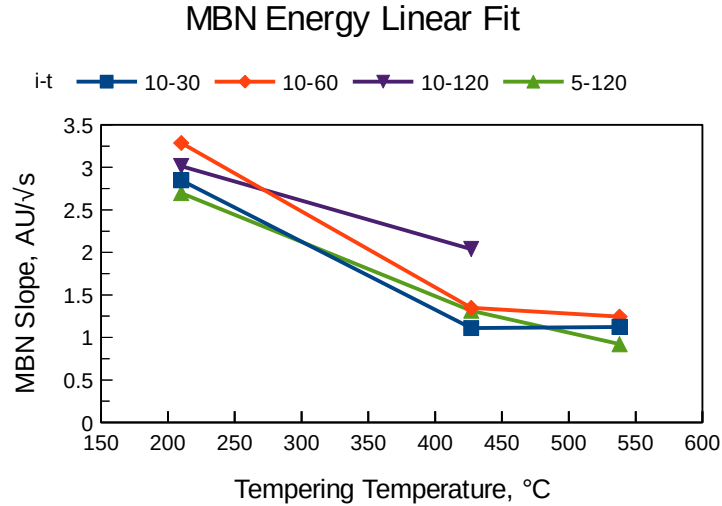


Figure 4.12: Variation of MBN energy slope with tempering temperature. Slope (in arbitrary energy units per \sqrt{s}) is determined from an ordinary least squares linear fit to the data in Figure 4.11 for 4140 steel samples.

the intensity of the emissions scales linearly with pinning strength (A in the power spectrum relation of Equation (2.22)). If, on the other hand, the energy of the waveform decreases while the number of events *increases* (or stays constant as it does in tests 21 and 31 for the more intense charging conditions of samples of $T_{temp} = 427^\circ\text{C}$), then the size of individual Barkhausen jumps (the magnitude of each event) must necessarily *decrease* to maintain the observed trend in energy.

4.7 Magnetoacoustic Emission

Magnetoacoustic behavior is inherently complicated by interactions between magnetostrictive/elastic effects and magnetic domain dynamics both of which are themselves sensitive to gradients in the bulk material, making precise characterization difficult. Additional experimental factors such as changes in transducer coupling, near field effects, and/or systematic interference tend to further obfuscate the nature of any single physical phenomenon on MAE trends. Nevertheless, the data presented in the following section indicate some promising relationships between hydrogen and magnetoacoustic emission, even if the precise

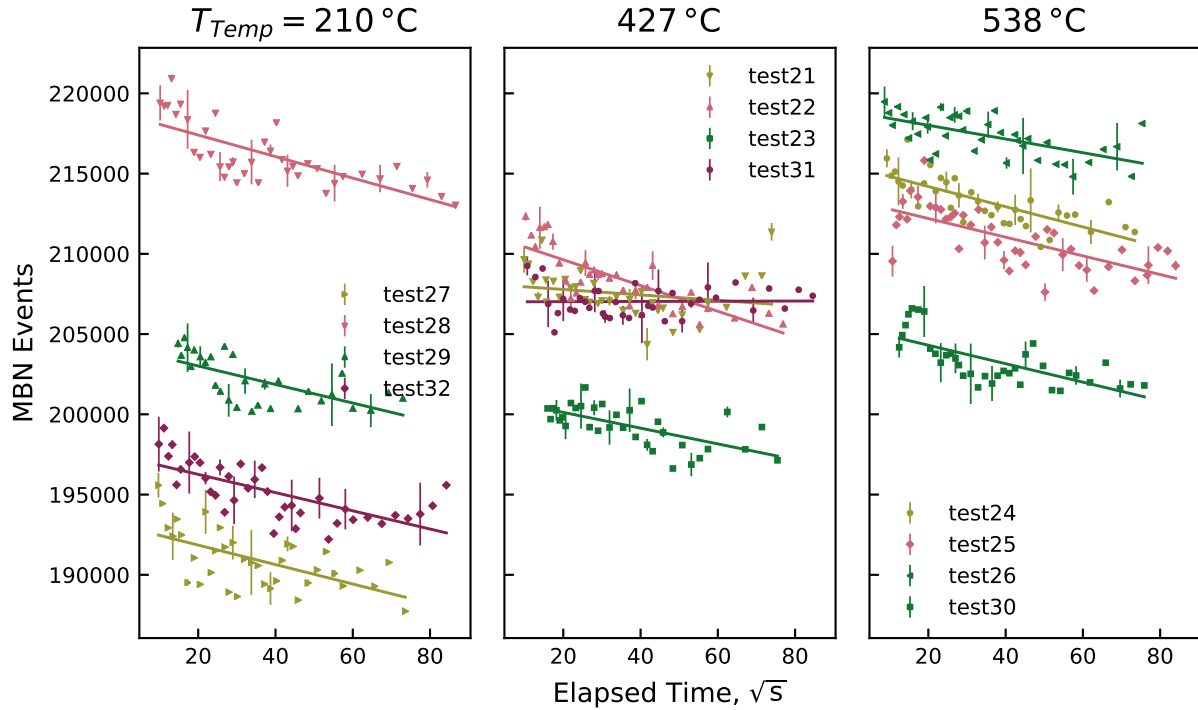
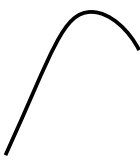
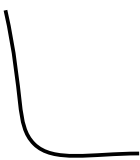
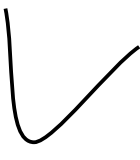
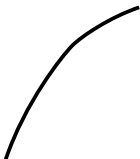


Figure 4.13: Change in the number of MBN emission events per waveform with loss of hydrogen in AISI 4140 steel. Lines are least squares fits to the total number of events, considered to be voltage levels greater than two standard deviations of the voltage estimated over the waveform. Plot colors indicate charging current density (mA cm^{-2})/time (minutes): 5/120 (—), 10/30 (—), 10/60 (—), and 10/120 (—).

nature of these relationships remains unclear.

Magnetoacoustic emission, as with Barkhausen noise, has been shown to increase in activity with hydrogen in the limited literature available on the subject[16]. Further, as MAE is sensitive to the bulk material, the trends shown in the figures that follow are perhaps not unexpected in consideration of the earlier discussion of hydrogen trapping and its role in the changes of hydrogen concentration towards the center, such as that shown in Figures 2.1 and 2.2. Schematics of these trends and the corresponding differences in model parameters are summarized in Table 4.1, and references to these characteristic behaviors are made in the following discussion.

Table 4.1: Schematic hydrogen desorption trends for magnetoacoustic emission experiments, with Oriani model parameters corresponding to general behavior of Figures 2.1 and 2.2

Trend	Shape	D_{eff}	K	Tests
A		High	Low	13, 16, 17, 19, and 20
B		High	High	10, 14, 21, and 26
C		High*	Low*	22–25, 27–29, 31 and 32
D		Low	Low	11, 12, 18, and 30

*Reflects the overall trend, but does not explain the initial rapid decrease

Beginning with 4340 samples, the energy (computed as before in Section 4.6) is presented in Figures 4.14 and 4.15 for the energy and number of events in each 4340 steel waveform. The data are again normalized to indicate relative change in each series to account for some of the effects of coupling differences, which are a more significant source of error for the piezoelectric trasnducers than they are for the Barkhausen pickup coil. Again, for clarity, only every third error bar is included and a Savitsky-Golay filter has been applied to the series to show general behavior.

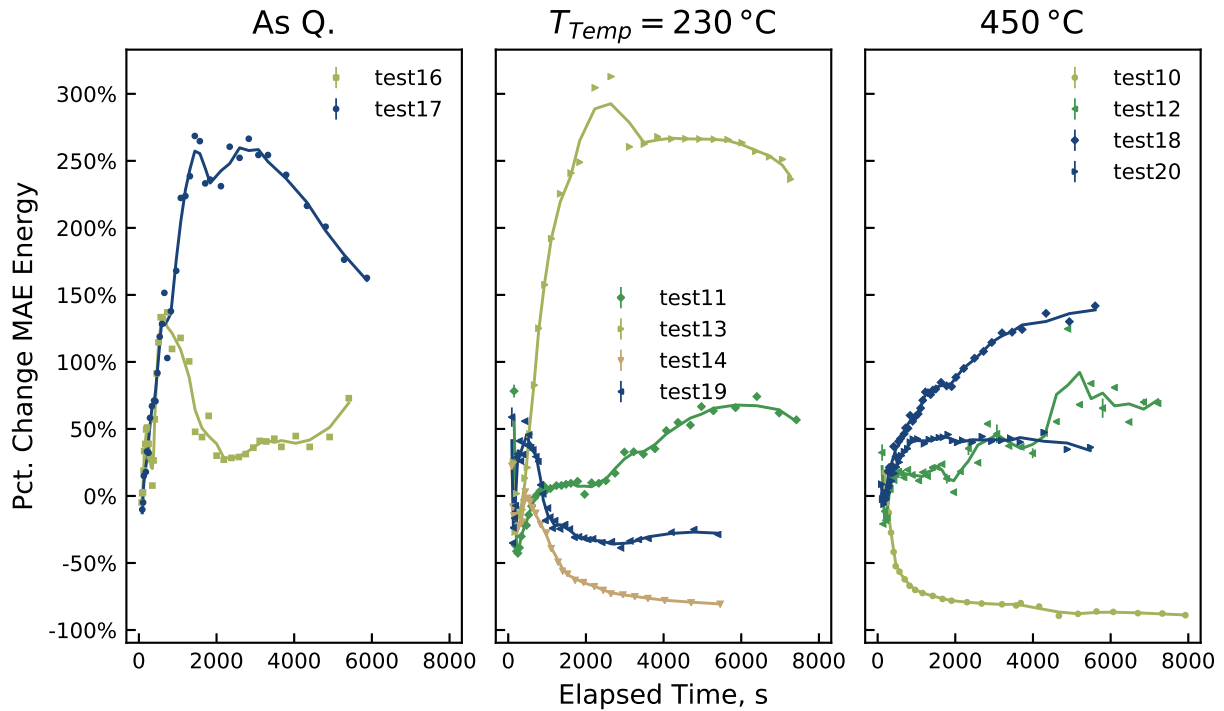


Figure 4.14: Magnetoacoustic emission energy evolution following hydrogen charging for various currents and times for AISI 4340. Plot colors indicate charging current density (mA cm^{-2})/time (minutes): 1/30 (—), 1/15 (—), 10/30 (—), and 10/60 (—).

Two distinct trends are observed in Figures 4.14 and 4.15: the magnetoacoustic energy either falls off with time in a near-logarithmic fashion as for tests 10 and 14 (Type “B”), or the energy increases to some maximum as high as a three-fold increase for some time and falls off again (Type “A”). Both behaviors are suggested in the hydrogen diffusion model of

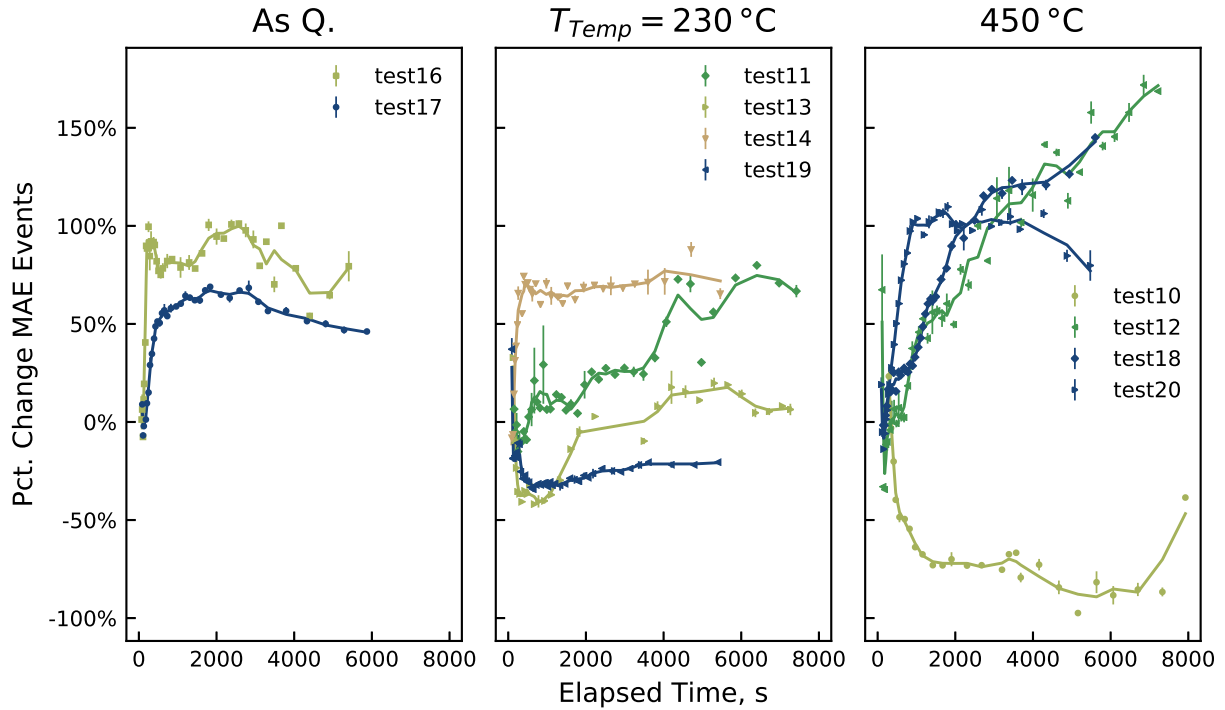


Figure 4.15: Evolution of magnetoacoustic emission events ($> 2\hat{\sigma}$) following hydrogen charging for various currents and times for AISI 4340. Plot colors indicate charging current density (mA cm^{-2})/time (minutes): 1/30 (—), 1/15 (—), 10/30 (—), and 10/60 (—).

Section 2.1.2 for the center of the samples. A logarithmic decay of hydrogen concentration in the center corresponds to high D_{eff} and K (Figure 2.4 bottom row). For those which exhibit the latter behavior, the location at which the maximum occurs is primarily dependent on the equilibrium constant in the Oriani model, where a later time suggests a lower K , suggesting a reduction in trapping activity. (Recall that the equilibrium constant is defined as the ratio of activities of trapping sites to lattice sites: $K = a_X/a_L$.) Those tests demonstrating Type “D” behavior may actually reflect an extended type “A” trend, where the eventual reduction in MAE activity has been cut off by the end of the test.

Relative variation in high strength 4140 steel samples over time is less than those of higher tempering temperatures, as shown in Figure 4.16, being of the order of 25% or less over the course of the test. Trends in energy profiles for 4140 steel exhibit Type B or C behavior,

but also exhibit peaks at around 15 minutes (1–2 ks). These peaks are also observed in the discharge profile for the number of events per waveform in Figure 4.17, which essentially mirrors the behavior of the energy.

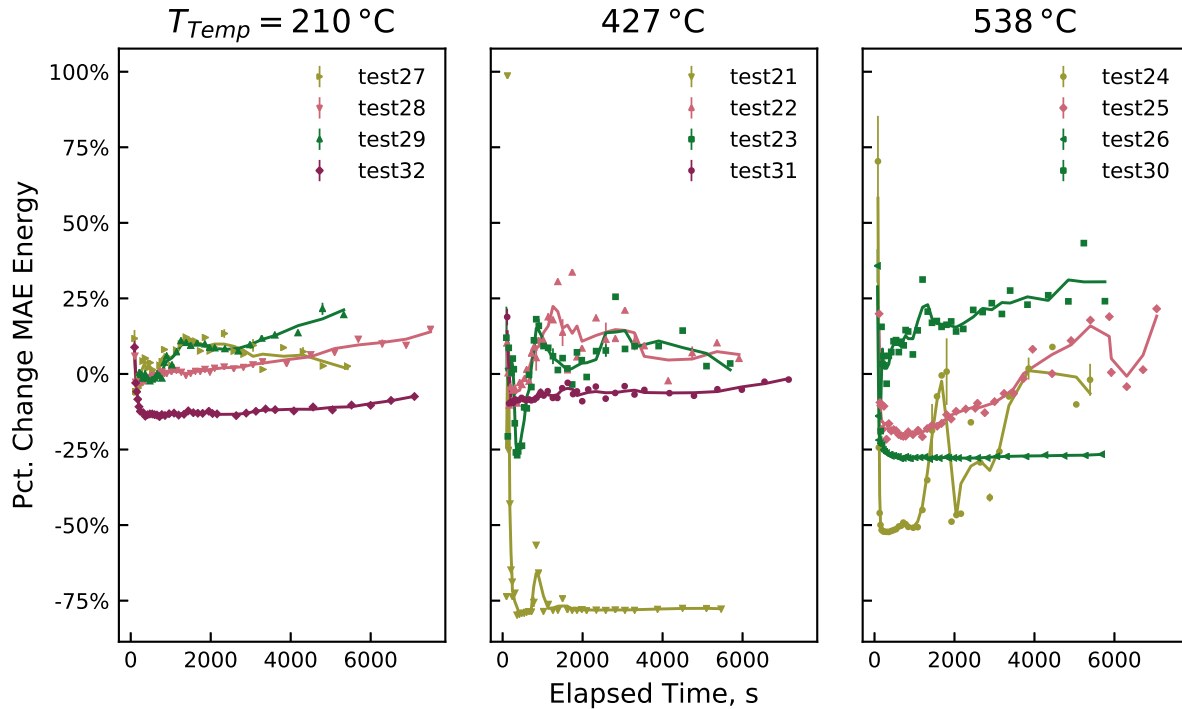


Figure 4.16: Magnetoacoustic emission “energy” evolution following hydrogen charging for various currents and times. Plot colors indicate charging current density (mA cm^{-2})/time (minutes): 5/120 (—), 10/30 (—), 10/60 (—), and 10/120 (—).

While the data obtained clearly demonstrate significant correlation between hydrogen concentration and magnetoacoustic emission activity, the variety of practical difficulties in developing consistent experimental conditions overwhelm a rigorous assessment of the functional relationship. In particular, the occurrence of an initial drop in activity followed by a steady increase (Type C) for 4140 steel remains unexplained.

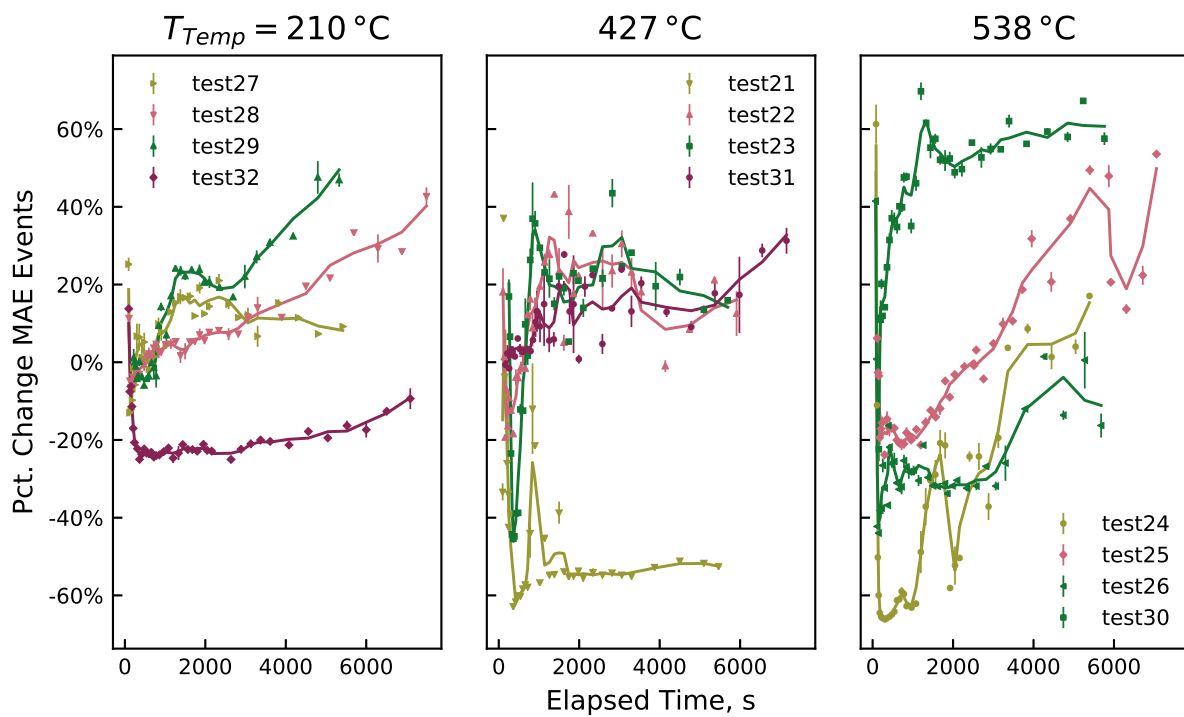


Figure 4.17: Magnetoacoustic emission events ($> 2\hat{\sigma}$) evolution following hydrogen charging for various currents and times. Plot colors indicate charging current density (mA cm^{-2})/time (minutes): 5/120 (—), 10/30 (—), 10/60 (—), and 10/120 (—).

CHAPTER 5

DISCUSSION

This Chapter discusses in general the results obtained in the context of hydrogen embrittlement and proposes a field-deployable probe ensemble consisting of the necessary features for analyzing hydrogen interactions as they relate to MAE/MBN emissions.

5.1 Discussion

Through observation of various changes in magnetic flux, Barkhausen noise, and magnetoacoustic emission during magnetization following electrolytic charging of low alloy steel, experimental evidence obtained in this investigation has demonstrated significant correlation between diffusible hydrogen and these magnetic properties. Specifically, the presence of hydrogen has been shown to enhance Barkhausen emission, and hydrogen diffusion is shown to agree semi-quantitatively with prevailing trapping theory in iron for material at or near the surface, as demonstrated in Section 4.6. For AISI 4140 steel, trapping effects were sufficiently weak such that a simple Fickian diffusional fit were obtained and comparison of fit parameters could be made, as shown in Figure 4.12. Such analysis could not be performed for 4340 steel, which appeared to demonstrate more complex behavior for the charging conditions used.

Measurement of magnetic quantities through the bulk of the samples also demonstrated sensitivity to hydrogen concentration, discussed in Section Sections 4.4 and 4.5. In particular, the apparent flux amplitude was increased in the presence of hydrogen concomitant with a decreased phase lag customary for linear loss processes. An increased permeability could explain this behavior, but hydrogen is generally thought to decrease this quantity. Further, hydrogen is observed to decrease apparent harmonic distortion for the conditions explored, which cannot be explained by any linear loss process such as eddy current generation or changes in (complex) permeability. Rather, it is supposed that the observed changes in flux,

as measured with a search coil in the core are due to variation in the hysteretic properties of steel with hydrogen, notably the coercivity, remanence, and magnetic moment.

The complex, coupled nature of magnetoacoustic emission makes definitive analysis of the data obtained difficult. In general, the observed trends in Section 4.7 suggest that MAE activity is decreased at higher concentrations, but inhomogeneous hydrogen distribution combined with transducer near-field and coupling effects were a source of considerable interference. Qualitatively, however, many of the observed trends agree with the trapping models discussed, where hydrogen continues to diffuse into the sample well after charging has ceased. The appearance of peaks in MAE activity may also be indicative of physical changes in the material, such as transitions of preferred interstitial sites or trapping locations, the physical nature of which remain only conjecture with the data available.

Differences in microstructure introduced by tempering are observed in the overall behavior of various trends in Barkhausen noise and through-core magnetic flux. In the case of MBN energy, the relatively simple form of the trend allowed for least squares fitting, and the effect of tempering can be seen to decrease the effective diffusivity near the surface. Changes in magnetic flux magnitude and harmonic distortion with hydrogen were in general greater for higher T_{temp} than for as quenched or high strength tempers, which may reflect greater variation in distribution, strength, or diversity in trapping locations such as precipitated carbides. Since it is the high strength steel microstructure which is most susceptible to hydrogen embrittlement and therefore most likely to be encountered in the application of this NDE technique, any variability due exclusively to microstructural changes is expected to be secondary.

5.2 Field Probe Design

Careful consideration of the signal conditioning and processing elements constitutes a significant portion of the overall design of any nondestructive evaluation technique. The groundwork for such a system is laid out here, informed by the experimental results and characterized behavior of the work in this study. While a field-deployable probe is the ulti-

mate goal, the methods explored here would find appreciable utility in a laboratory setting, being adapted, for example, as a characterization tool in hydrogen permeation studies.

Figure 5.1 presents a block diagram for the generation of an oscillating magnetic field and the data acquisition system for detecting MAE and MBN features in plates across a weld. Design of a data acquisition system consisting of the block elements in blue (and suggested components) could be implemented for a PC-based system using the PCIe bus or as a peripheral device using the USB interface. The bandwidth of the PCIe bus would be of significant advantage if the decision was made to fully utilize the CPU/GPU and extended computing libraries available for signal processing (e.g. OpenCL/CUDA). The following explains the key features of the PC-based approach.

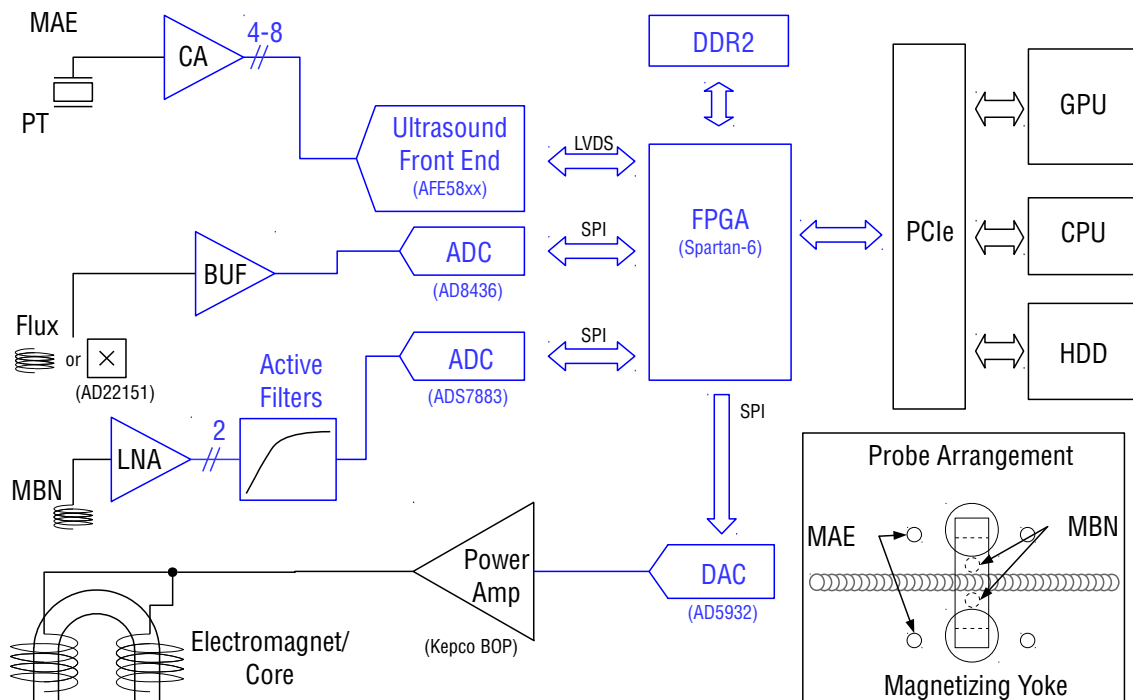


Figure 5.1: Proposed field NDE probe digitization and processing block diagram. Pertinent features of the internal circuit are shown in blue, with current component series/values in brackets. The choice of FPGA is for a PCIe-based configuration; an alternative could be a Zynq-7000 system-on-chip design for a USB interface, but would be without ready access to the CPU/GPU for digital signal processing (e.g. FFT, etc.).

- For MAE measurements, an analog front end (AFE) such as that currently available from Texas Instruments (AFE5800-series) includes the appropriate digital filters, low noise and variable gain amplifiers (LNAs, VGAs), and multiple high resolution ADCs of sufficient sample rate suitable for multiple ultrasonic sensors. Four or more PTs could potentially allow for some degree of localization for magnetoacoustic emissions. These particular AFEs are marketed for amplified medical ultrasound sensors; inclusion of a charge amplifier in the signal processing chain is likely needed.
- Core flux in the magnetic yoke can be determined by secondary coil, as has been done in this work, and/or by direct measurement of the magnetic field by a Hall Effect sensor. The low frequency of magnetization makes the choice of ADC in this application one of cost effectiveness if the flux is to be digitized directly; alternatively the RMS value of the flux can be estimated by a direct RMS converter (as shown), though any sense of the change in phase would be lost in this case.
- Multiple MBN search coils can be implemented to reduce the effects of flux leakage from the magnetic circuit by either subtracting the filtered signal digitally (as shown) or by antiparallel orientation of the coils to cancel the common mode low-frequency flux.
- Inducing the magnetic flux through the core would best be accomplished with a dedicated bipolar power supply such those available from Kepco. These linear supplies would not suffer the same issues encountered with the audio amplifier used in this study, i.e. low frequency cutoff and high frequency switching noise. BOP-series amplifiers are available which can source and sink several amperes. Again, the low f_d of these tests would allow for any of a large number of DACs to be used, but a generating IC capable of various waveforms up to 25 MHz is included here.
- Finally, a field-programmable gate array (FPGA) ties together the digital signals in the board and allows rapid storage of waveforms in memory before passing them on for sub-

sequent analysis. Depending on the size of the waveforms and the number of available gates on the FPGA, some significant digital signal processing can be accomplished here as well. For relatively unsophisticated signal processing schemes, a combined ARM-based system-on-chip (SoC) and FPGA device such as the Zynq-7000-series from Xilinx would be an excellent alternative.

5.3 Conclusions

With the results of experiments and the lessons learned in hand, discussion now concludes with an assessment of the guiding questions outlined in the beginning of this investigation and summarizes the pertinent findings with suggestions for further work—this study is, after all, on the subject of hydrogen.

1. Hydrogen enhances the Barkhausen effect, and appears to demonstrate a direct, perhaps linear relationship with hydrogen concentration. Magnetoacoustic emission, though complicated by various experimental factors, exhibits qualitatively similar effects.
2. Low alloy steel samples tempered at higher temperatures demonstrated greater variability in general behavior in all magnetic properties explored in this study. Higher strength (lower T_{temp}) resulted in more consistent behavior overall.
3. The algorithms and analytical techniques developed in this study were sufficient to glean semi-quantitative hydrogen diffusion information from Barkhausen noise experiments. Magnetoacoustic emission presents additional experimental and theoretical challenges for practical implementation of such techniques, but additional study may very well prove fruitful.
4. A field-portable or laboratory instrument would require some substantial investment in electronic hardware and analytical software design, but many of the necessary features have been evaluated in this study.

Overall, the magnetic properties of steel appear to demonstrate strong correlation with hydrogen concentration. Barkhausen noise, being detectable only near the surface due to electromagnetic attenuation in conductive samples, gives expected results for diffusing hydrogen at the interface. The limited penetration depth makes analysis of Barkhausen noise especially well-suited to thin materials or performing hydrogen permeation studies (i.e. detection at a hydrogen free surface).

Magnetoacoustic emission is sensitive to bulk elastic and magnetic/electronic properties, but the wide variety of possible interactions and changes in coupling makes analysis of particular features difficult in the absence of extensive (and specific) characterization and controlled environment. The complicated trends observed in MAE with time may be due to microscopic changes in the material such as localized redistribution of hydrogen atoms or stresses induced by electrolytic charging (e.g. from formation of microcracks or inclusions). On the other hand, minor differences in transducer coupling or ultrasonic wave propagation characteristics can have profound effects for sample geometries used in this study. One effective (but costly) alternative to piezoelectric transducers might be laser Doppler vibrometry, which allows for detection of acoustic vibrations from a (physically decoupled) distance. In any of the aforementioned cases, however, more experiments on well-defined samples would surely clarify some of the behaviors observed.

Finally, the amplitude and harmonic distortion of the EMF generated by changing magnetic flux in the circuit is presumably caused by nonlinear magnetization dynamics and appears to strongly correlate with hydrogen content in the sample. There are two major advantages to characterizing the magnetic flux in this or similar ways. Correcting differences in coupling for a toroidal magnetic circuit is relatively simple compared to Barkhausen noise or magnetoacoustic emission, as any gaps result in a linear decrease in magnitude. Depending on the geometry, however, the measurement remains largely sensitive to bulk properties as the flux permeates throughout a magnetic material via the path of least reluctance.

As is the case with all nondestructive evaluation schemes, measurement of more than one physical property by different techniques gives significantly better insight into the state of the material in question. Further, for each method utilized, variation in experimental parameters can increase sensitivity to particular effects, and isolate changes due to certain physical features. It is clear, therefore, that any system designed for the determination or characterization of hydrogen in steel by magnetic properties should make use of all techniques available and be extended to include analysis of the response to changes in magnetizing frequency, magnitude, and wave shape.

REFERENCES CITED

- [1] Louis Raymond, editor. *Hydrogen Embrittlement: Prevention and Control*, number STP962, 1988. ASTM International.
- [2] John P. Hirth. Effects of hydrogen on the properties of iron and steel. *Metall. Trans. A*, 11A:861–890, June 1980.
- [3] Michael Smialowski. *Hydrogen in steel*. Pergamon Press, Warszawa, 1962.
- [4] A.N. Lasseigne, K. Koenig, D.L. Olson, J.E. Jackson, B. Mishra, and J.D. McColskey. Real-time low frequency impedance measurements for determination of hydrogen content in pipeline steel. In *Review of Progress in Quantitative Nondestructive Evaluation 28*, volume 1096, pages 1283–1290. AIP, 2009.
- [5] K. Koenig, A.N. Lasseigne, J.E. Jackson, D.L. Olson, and B. Mishra. A fundamental analysis of low frequency impedance phenomenon: Application to hydrogen content assessment of coated linepipe steel weldments. In *Review of Progress in Quantitative Nondestructive Evaluation 30*, volume 1335, pages 1163–1167. AIP, 2011.
- [6] Kh.G. Schmitt-Thomas and A. Bauberger. Nondestructive detection of hydrogen in steel by vibration damping. *NDT Int.*, 21(5):327–332, 1988.
- [7] P. Senior and J. Szilard. Ultrasonic detection of hydrogen in pipeline steel. *Ultrasonics*, pages 42–44, 1984.
- [8] F.W.H Dean and D.J. Fray. Ultrasensitive technique for detection of hydrogen emanating from steel and other solid surfaces. *Mater. Sci. Tech. Ser.*, 16:41–46, 2000.
- [9] R.D. Smith II, D.K. Benson, I. Maroef, D.L. Olson, and T.R. Wildeman. The determination of hydrogen distribution in high-strength steel weldments part 1: Laser ablation methods. *Weld. J.*, 80(5):115–121–s, 2001.
- [10] R.D. Smith II, G.P. Landis, I. Maroef, D.L. Olson, and T.R. Wildeman. The determination of hydrogen distribution in high-strength steel weldments part 2: opto-electronic diffusible hydrogen sensor. *Weld. J.*, 80(5):122–125–s, 2001.
- [11] D.J. Buttle, G.A.D. Briggs, J.P. Jakubovics, E.A. Little, and C.B. Scruby. Magnetoacoustic and Barkhausen emission in ferromagnetic materials. *Phil. Trans. R. Soc. Lond. A*, 320:363–378, 1986.

- [12] D.J. Buttle, C.B. Scruby, J.P. Jakubovics, and G.A.D Briggs. Magneto-acoustic and barkhausen emission: their dependence on dislocations in iron. *Phil. Mag. A*, 55(6): 717–734, 1987.
- [13] Werner Pepperhoff and Mehmet Acet. *Constitution and Magnetism of Iron and its Alloys*. Springer, Berlin, 2001.
- [14] S.V. Grishakov, Yu.I. Archakov, V.P. Terent'ev, A.I. Kovalev, and O.B. Ershova. Barkhausen effect as a means of evaluating the hydrogen corrosion of steels. *Strength Mater.*, 21(4):535–540, 1989.
- [15] Z.T. Nazarchuk, V.R. Skal's'kyi, B.P. Klym, V.D Rudavs'kyi, P.P. Velykyi, and Ya. D. Tolopko. Influence of hydrogen on the changes in the power of Barkhausen jumps in ferromagnets. *Mat. Sci.*, 45(5):663–669, 2009.
- [16] Yevhen Pochapsky, Zinoviy Nazarchuk, Valentin Skalsky, and Sviatoslav Hirnyj. Application of magnetoacoustic emission for detection of hydrogen electrolytically absorbed by steel. In *19th European Conference on Fracture: Fracture Mechanics for Durability, Reliability and Safety*, 2012.
- [17] A. McNabb and P.K. Foster. A new analysis of the diffusion of hydrogen in iron and ferritic steels. *T. Metall. Soc. AIME*, 227:618–627, 1963.
- [18] R.A. Oriani. The diffusion and trapping of hydrogen in steel. *Acta Metall.*, 18:147–157, 1970.
- [19] Lawrence S Darken and Rodney P Smith. Behavior of hydrogen in steel during and after immersion in acid. *Corrosion*, 5(1):1–16, 1949.
- [20] Ward Cheney and David Kincaid. *Numerical Mathematics and Computing*. Thomson Brooks/Cole, Belmont, CA, 6th edition, 2008.
- [21] J. Svoboda and F.D. Fischer. Modelling for hydrogen diffusion in metals with traps revisited. *Acta Mater.*, 60:1211–1220, 2012.
- [22] Yoshiichi Sakamoto and Tadashi Mantani. Effect of quenching and tempering on diffusion of hydrogen in carbon steel. *Trans. JIM*, 17:743–748, 1976.
- [23] Yoshiichi Sakamoto, Keizo Takao, and Shuzo Tokumitsu. Effect of quenching and tempering on diffusion of hydrogen in high-strength alloy steels. *Trans. JIM*, 18:603–609, 1977.
- [24] A.A. Astaf'ev. Diffusion and evolution of hydrogen from steel. *Met Sci Heat Treat*, 33(2):93–96, 1991.

- [25] Sōshin Chikazumi. International series of monographs on physics. In Chad D Graham, editor, *Physics of Ferromagnetism*, volume 94. Oxford University Press, 2nd edition, 1997.
- [26] B.D. Cullity. *Introduction to Magnetic Materials*. Addison-Wesley, Reading, Mass., 1972.
- [27] David Jiles. *Introduction to Magnetism and Magnetic Materials*. CRC Press, Boca Raton, FL, 3rd edition, 2016.
- [28] Linus Pauling. The nature of the interatomic forces in metals. *Phys. Rev.*, 54:899–904, 1938.
- [29] J.C. Slater. The ferromagnetism of nickel. *Phys. Rev.*, 49:537–545, 1936.
- [30] K.B. Hathaway, H.J.F. Jansen, and A.J. Freeman. Total-energy local-spin-density approach to structural and electronic properties of ferromagnetic iron. *Phys. Rev. B*, 31(12):7603–7611, 1985.
- [31] Yoshio Itsumi and D.E. Ellis. Electronic bonding characteristics of hydrogen in bcc iron: Part i. interstitials. *J. Mater. Res.*, 11(9):2206–2213, 1996.
- [32] P.P. Cioffi. Hydrogenized iron. *Phys. Rev.*, 39:363–367, Jan 1932.
- [33] R.K. Reber. The effect of nascent hydrogen on the magnetic properties of iron. *Phys.*, 5:297–301, 1934.
- [34] M.E. Elzain and A.A. Yousif. Local magnetic moment and hyperfine field in hydrogenated iron and iron-vanadium alloy. *Hyperfine Interac.*, 94:1879–1884, 1994.
- [35] Genrich L. Krasko and G.B. Olson. Effect of hydrogen on the electronic structure of a grain boundary in iron. *Solid State Commun.*, 79(2):113–117, 1991.
- [36] Rainer H'olzle, editor. *Physical origins and theoretical models of magnetic anisotropy*, number 24 in Magnetismus von Festkörpern und grenzflächen, 3 1993. IFF-Ferienkurs, Forschungszentrum, Jülich.
- [37] Bruno Alessandro, Cincia Beatrice, Giorgio Betottie, and Arianna Montorsi. Domain-wall dynamics and Barkhausen effect in metallic ferromagnetic materials. I. Theory. *J. Appl. Phys.*, 1990.
- [38] Stefano Zapperi, Pierre Cizeau, Gianfranco Durin, and Eugene H. Stanley. Dynamics of a ferromagnetic domain wall: Avalanches, depinning transition, and the Barkhausen effect. *Phys. Rev. B*, 58(10):6353–6366, 1998.

- [39] Gianfranco Durin and Stefano Zapperi. Scaling exponents for Barkhausen avalanches in polycrystals and amorphous ferromagnets. *Phys. Rev. Lett.*, 84:4705–4708, 2000.
- [40] Djordje Spasojević, Srdjan Bukvić, Sava Milošević, and H. Eugene Stanley. Barkhausen noise: Elementary signals, power laws, and scaling relations. *Phys. Rev. E*, 54(3):2531–2546, 1996.
- [41] M. Ortiz and J. Ovejero-Garcia. Effect of hydrogen on Young’s modulus of AISI 1005 and 1070 steels. *J. Mater. Sci.*, 27:6777–6781, 1992.
- [42] E. Lunarska, A. Zielinski, and M. Smialowski. Effect of hydrogen on shear modulus of polycrystalline α -iron. *Acta Mater.*, 25:305–308, 1977.
- [43] D. Psiachos, T. Hammerschmidt, and R. Dratz. Ab initio study of the modification of elastic properties of α -iron by hydrostatic strain and by hydrogen interstitials. *Act. Mater.*, 59:4255–4263, 2011.
- [44] V.R. Skal’s’skyi, O.M. Serhienko, V.B. Mykhal’chuk, and R.I. Semeheniiv’s’kyi. Quantitative evaluation of Barkhausen jumps according to the signals of magnetoacoustic emission. *Mat. Sci.*, 45:399–408, 2009.
- [45] J.D. Eshelby. The determination of the elastic field of an ellipsoidal inclusion, and related problems. *Proc. R. Soc. London, A*, 241(1226):376–396, 1957.
- [46] E.S. Gorkunov, Yu N. Dragoshanskii, and V.A. Khamitov. Magnetoelastic acoustic emission in ferromagnetic materials. ii. effect of elastic and plastic strains on parameters of magnetoelastic acoustic emission. *Russian journal of nondestructive testing*, 37(12): 835–858, 2001.
- [47] F. Liorzou, B. Phelps, and D.L. Atherton. Macroscopic models of magnetization. *IEEE T. Magn.*, 36(2):418–428, 2000.
- [48] D.C. Jiles and D.L. Atherton. Theory of ferromagnetic hysteresis. *J. Magn. Magn. Mater.*, 61:48–60, 1986.
- [49] David C. Jiles, J.B. Thielke, and M.K. Devine. Numerical determination of hysteresis parameters for the modeling of magnetic properties using the theory of ferromagnetic hysteresis. *IEEE T. Magn.*, 28(1):27–35, 1992.
- [50] A. Ramesh, M.R. Govindaraju, D.C. Jiles, S.B. Biner, and J.M. Roderick. Hydrogen charging in nickel and iron and its effect on their magnetic properties. *J. Appl. Phys.*, 79:5453–5455, 1996.

- [51] V. Moorthy, S. Vaidyanathan, T. Jayakumar, and Baldev Raj. On the influence of tempered microstructures on magnetic Barkhausen emission in ferritic steels. *Philos. Mag. A*, 77(6):1499–1514, 1998.
- [52] American Society of Mechanical Engineers, O.J. Horger, S.L. Hoyt, J.W. Huckert, and R.W. Bolz. *ASME Handbook: Metals properties; edited by Samuel L. Hoyt*. ASME Handbook. McGraw-Hill, 1954.
- [53] W.W. Gerberich, T. Livne, X.-F. Chen, and M. Kaczorowski. Crack growth from internal hydrogen—temperature and microstructural effects in 4340 steel. *Metall. Trans. A*, 19A:1319–1334, 1988.
- [54] Woei-Shyan Lee and Tzay-Tian Su. Mechanical properties and microstructural features of AISI 4340 high-strength alloy steel under quenched and tempered conditions. *J. Mater. Process. Tech.*, 87:198–206, 1999.
- [55] Thony V. Philip and Thomas J. McCaffrey. Ultrahigh-strength steels. In *Properties and Selection: Irons, Steels, and High-Performance Alloys*, volume 01 of *ASM Handbook*. ASM International, 1990.
- [56] R.D. McCright and R.W. Staehle. Effect of arsenic upon the entry of hydrogen into mild steel as determined at constant electrochemical potential. *J. Electrochem. Soc.*, 121(5):609–618, 1974.
- [57] O. Shim and J.G. Byrne. A study of hydrogen embrittlement in 4340 steel i: Mechanical aspects. *Mat. Sci. and Eng.*, A123:169–180, 1990.
- [58] W48 Committe. Diffusible hydrogen in mild steel and low-alloy steel weld metals: Test method. Standard CSA W48.7-M1977, Canadian Standards Association, 1977.
- [59] James Karki. Signal conditioning piezoelectric sensors. Application Note SLOA033A, Texas Instruments, September 2000.
- [60] D.J. van Ooijen and J.D. Fast. Electrical resistance of hydrogen-charged iron wires. *Acta. Metall.*, 11:211–216, 1963.
- [61] B. Lindgren and D.E. Ellis. Hyperfine fields and electronic structure of hydrogen impurities in transition metals. *Phys. Rev. B*, 26(2):636–647, 1982.
- [62] Geert Mertens, Lode Duprez, Bruno C De Cooman, and Marc Verhaege. Hydrogen absorption and desorption in steel by electrolytic charging. In *Advanced Materials Research*, volume 15, pages 816–821. Trans. Tech. Publ., 2007.